Astronomy Letters, Vol. 31, No. 2, 2005, pp. 103–108. Translated from Pis'ma v Astronomicheskiĭ Zhurnal, Vol. 31, No. 2, 2005, pp. 116–121.

Further Photometric Observations of the X-ray Binary A0535+26/V725 Tau: A New Activity Cycle

G. V. Zaitseva*

Sternberg Astronomical Institute, Universitetskiĭ pr. 13, Moscow, 119992 Russia

Received August 2, 2004

Abstract—We performed new photoelectric UBV observations of the X-ray binary A0535+26 at the Crimean Station of the Sternberg Astronomical Institute in 1998–2003. After the brightness stabilized at a minimum of about 500 days in duration, a new brightness rise steeper than that observed previously began: the brightness increased over two seasons of observations by a total amplitude of $0^m.5$. The physical parameters (T_e, n_e) of the additional emission that caused this brightening match, within the error limits, were obtained from the averaged over 15 years, data, that include both the ascending and descending branches of the light curve. We found a delay of the variations in the Hα line relative to the continuum, which is no more than one year. © *2005 Pleiades Publishing, Inc.*

Key words: *stars—X-ray binaries, photometry, variability, A0535+26.*

INTRODUCTION

The transient X-ray source A0535+26 attracted the attention of researchers after its first intense X-ray outburst in April 1975 (Rosenberg *et al.* 1975). This is a binary with a neutron star, a pulsar with a period of 103 s and an orbital period of 111^d (see the review by Giovannelli and Graziati 1992). The orbital eccentricity is ~ 0.3, its X-ray outbursts occur during periastron passages. The spectral type of the massive (10–20 $M_\odot$) optical star was found to be O9.7 IIIe (Giangrande *et al.* 1980). The Be star and its surrounding envelope mainly give the optical emission of this binary. This X-ray source was subsequently identified with a variable Be star that was later designated as V725 Tau (HDE 245770).

The most comprehensive analysis of the star's photometric behavior over 100 years was performed by Lyutyi and Zaitseva (2000). The light curve from 1898 until 1975 could be traced using photographs from the Harvard and Sonneberg observatories and few photoelectric observations by different authors. Systematic photoelectric UBV observations of the star V725 Tau were begun at the Crimean Station of the Sternberg Astronomical Institute (SAI) in 1983. Some of these observations are presented in the papers by Gnedin *et al.* (1988), Lyutyi *et al.* (1989), and Lyutyi and Zaitseva (2000). The combined light curve constructed from all of these observations is given in the paper by Lyutyi and Zaitseva (2000). A gradual decline in brightness, on average, from $9^m.8$ to $9^m.9$ in B, was observed from 1898 until 1950. The minimum of 1945–1949 was followed by a quiescent state at a mean level of $9^m.83$, and then a rather rapid rise in brightness to the maximum of 1975–1980 began. Subsequent photoelectric observations revealed variations with a quasi-period of 1400 days against the background of a general gradual decline in brightness. In the fall of 1998, the star's brightness reached its minimum over the entire period of its photoelectric observations, $B = 9^m.9$, and remained at this level during the entire next observing season. The Hα emission line changed to an absorption one. The authors concluded that the star's active phase related to the envelope ejection by the Be star terminated.

This paper is a direct continuation of the series of studies of this star based, in particular, on photoelectric observations at the Crimean Station of the SAI (Gnedin *et al.* 1988; Lyutyi *et al.* 1989; Clark *et al.* 1998, 1999; Lyutyi and Zaitseva 2000).

OBSERVATIONS

The observations were performed with a UBV photometer attached to a 60-cm reflector at the Crimean Station of the SAI. The instrumental photometric system was close to Johnson's standard system (see Lyutyi and Zaitseva (2000) for the reduction coefficients). The same comparison star as previously was used; its V magnitude and color indices are also given in our previous paper (Lyutyi and Zaitseva 2000). The table presents our new observations over five seasons, from the fall of 1998

*E-mail: gvz@sai.crimea.ua

1063-7737/05/3102-0103$26.00

UBV observations of A0535+26 in the period 1998–2003

JD 2400000+	V	$B-V$	$U-B$	JD 2400000+	V	$B-V$	$U-B$
51197.308	9.453	0.406	−0.624	51532.174	9.220	0.465	−0.679
51197.315	9.447	0.408	−0.625	51532.241	9.223	0.458	−0.670
51197.351	9.447	0.409	−0.621	51549.289	9.266	0.457	−0.662
51199.261	9.433	0.408	−0.617	51549.297	9.258	0.479	−0.672
51199.267	9.432	0.411	−0.611	51579.290	9.149	0.485	−0.681
51199.307	9.438	0.404	−0.618	51579.300	9.163	0.474	−0.665
51235.307	9.458	0.410	−0.605	51581.235	9.139	0.504	−0.655
51235.315	9.470	0.407	−0.631	51581.242	9.153	0.489	−0.662
51235.328	9.464	0.397	−0.620	51586.323	9.169	0.495	−0.619
51264.260	9.449	0.406	−0.628	51605.282	9.240	0.475	−0.675
51264.269	9.446	0.417	−0.613	51615.269	9.243	0.463	−0.690
51264.284	9.446	0.422	−0.604	51615.277	9.248	0.459	−0.698
51266.252	9.462	0.404	−0.644	51618.239	9.217	0.472	−0.643
51266.259	9.465	0.398	−0.618	51618.245	9.225	0.468	−0.660
51274.254	9.430	0.416	−0.623	51627.231	9.232	0.477	−0.712
51274.262	9.458	0.400	−0.599	51627.250	9.213	0.468	−0.694
51274.269	9.490	0.398	−0.602	51628.243	9.178	0.498	−0.716
51281.263	9.472	0.432	−0.647	51629.248	9.190	0.483	−0.690
51432.554	9.296	0.461	−0.684	51641.250	9.196	0.491	−0.686
51432.562	9.310	0.458	−0.672	51641.258	9.186	0.488	−0.644
51433.558	9.277	0.455	−0.659	51645.254	9.188	0.491	−0.684
51433.570	9.279	0.452	−0.664	51645.262	9.194	0.505	−0.680
51438.535	9.307	0.446	−0.664	51798.592	9.079	0.539	−0.692
51438.549	9.295	0.461	−0.650	51816.510	9.122	0.520	−0.690
51439.566	9.303	0.459	−0.683	51819.487	9.114	0.514	−0.677
51439.572	9.304	0.457	−0.666	51822.478	9.112	0.524	−0.660
51445.533	9.321	0.459	−0.669	51824.508	9.130	0.508	−0.721
51445.544	9.322	0.453	−0.642	51824.515	9.131	0.515	−0.720
51452.513	9.447	0.405	–	51840.517	9.140	0.499	−0.680
51452.517	9.426	0.418	–	51840.524	9.137	0.508	−0.704
51454.461	9.326	0.450	−0.651	51841.435	9.132	0.508	−0.710
51454.520	9.330	0.429	−0.634	51842.518	9.148	0.505	−0.730
51455.473	9.338	0.438	−0.651	51848.456	9.193	0.499	−0.714
51455.508	9.342	0.434	−0.643	51853.399	9.098	0.497	−0.650
51467.438	9.309	0.437	−0.674	51864.429	8.983	0.518	−0.657
51468.424	9.301	0.436	−0.634	51865.443	9.019	0.518	−0.656
51491.474	9.337	0.415	−0.658	51866.369	9.008	0.526	−0.653
51491.482	9.341	0.420	−0.639	51867.408	9.011	0.532	−0.650
51492.401	9.315	0.452	−0.623	51869.338	9.014	0.553	−0.717
51492.417	9.337	0.425	−0.657	51869.349	9.021	0.527	−0.632
51493.435	9.358	0.430	−0.648	51879.351	9.054	0.531	−0.656
51493.443	9.361	0.424	−0.644	51901.269	9.051	0.530	−0.692
51493.486	9.365	0.431	−0.650	51901.274	9.048	0.531	−0.687
51502.398	9.366	0.450	−0.659	51903.238	9.054	0.531	−0.679
51502.404	9.351	0.460	−0.639	51903.243	9.057	0.521	−0.675
51516.475	9.245	0.468	−0.657	51924.216	8.987	0.523	−0.623
51516.480	9.253	0.465	−0.684	51925.266	9.012	0.525	−0.667
51524.417	9.268	0.469	−0.689	51932.329	9.015	0.541	−0.668
51933.228	9.028	0.521	−0.659	52346.263	9.012	0.540	−0.683
51951.216	9.040	0.536	−0.683	52376.305	9.011	0.554	−0.666
52004.282	9.114	0.524	−0.686	52536.505	9.142	0.515	−0.693
52185.576	9.049	0.523	−0.693	52557.536	9.228	0.491	−0.735
52185.583	9.029	0.530	−0.647	52613.412	9.223	0.495	−0.745
52187.557	9.032	0.534	−0.687	52613.416	9.231	0.471	−0.728
52187.564	9.031	0.541	−0.677	52619.277	9.180	0.489	−0.710
52192.542	9.045	0.539	−0.676	52619.282	9.174	0.489	−0.712
52193.517	9.063	0.529	−0.682	52635.444	9.081	0.518	−0.695
52196.542	9.076	0.523	−0.693	52635.457	9.083	0.512	−0.690
52208.471	9.089	0.530	−0.714	52636.381	9.073	0.524	−0.699
52209.536	9.074	0.525	−0.705	52675.324	9.181	0.496	−0.741
52249.335	9.049	0.532	−0.694	52684.210	9.146	0.501	−0.727
52254.360	9.085	0.515	−0.697	52684.219	9.146	0.497	−0.705
52308.259	9.018	0.531	−0.660	52691.243	9.127	0.506	−0.718
52309.260	9.035	0.534	−0.699	52691.259	9.111	0.524	−0.731
52313.302	9.039	0.523	−0.677	52697.312	9.157	0.499	−0.713
52324.264	9.020	0.531	−0.677	52697.332	9.154	0.512	−0.723
52332.268	9.025	0.557	−0.672	52698.254	9.169	0.492	−0.710
52339.315	9.034	0.515	−0.670	52698.268	9.158	0.502	−0.715
52343.228	9.003	0.545	−0.675				

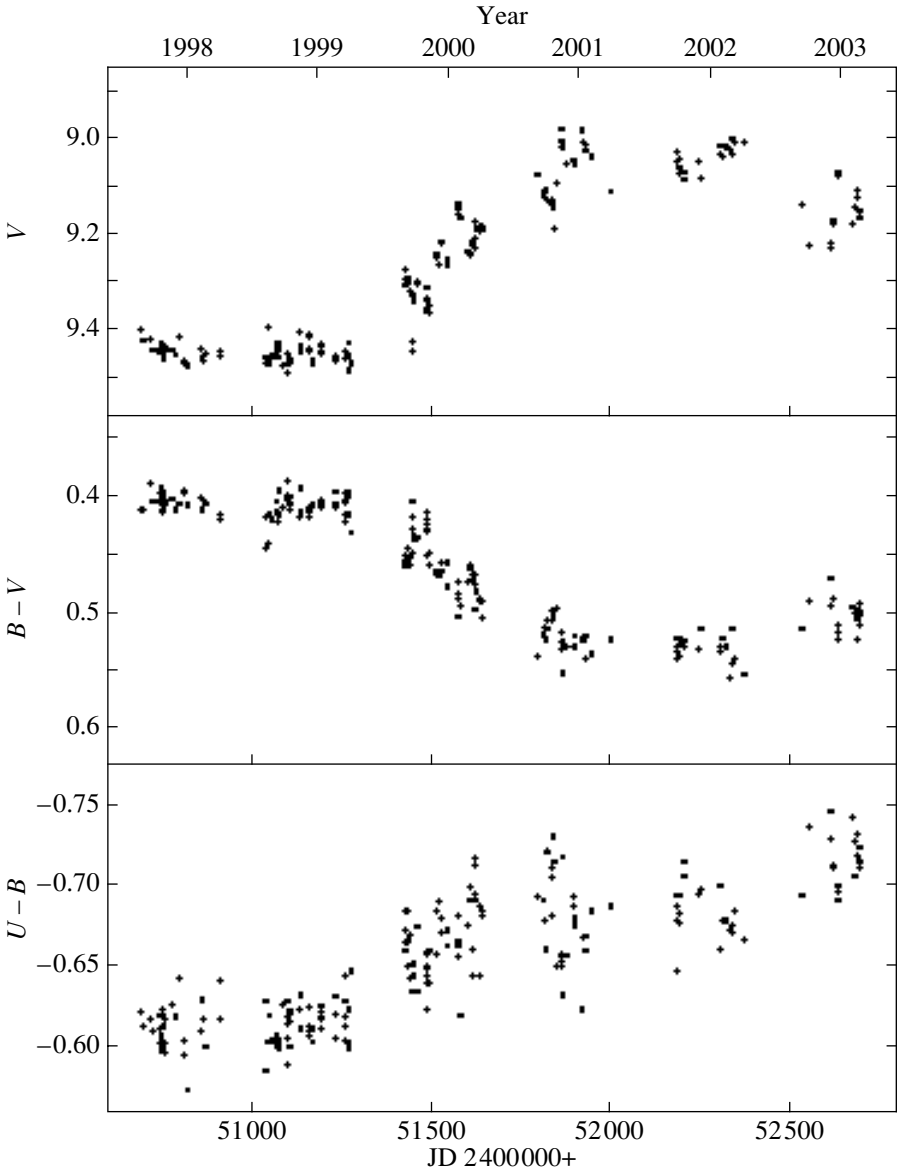

Fig. 1. Light and color curves of A0535+26 in 1998–2003.

until the spring of 2003; Fig. 1 shows the corresponding light and color curves for V725 Tau. During the first observing season, the star was at minimum light, with small fluctuations of a few hundredths of a magnitude. The star was in this state for more than 500 days. The star's brightness began to rise in the fall of 1999. A similar but slower brightening also occurred during the next observing season. The brightening from minimum to maximum lasted about 500 days. The mean brightness of the star again began to decline in 2002–2003. Figure 2 shows color–magnitude relations over the period of our observations. As the brightness rose from $9^m.5$ to $9^m.0$, the $B - V$ color index gradually increased from $0^m.40$ to $0^m.55$, while the behavior of the $U - B$ color index was ambiguous: it decreased as the brightness rose by half the amplitude and increased as the star brightened further. A significant scatter of data points exceeding the observational errors and attributable to the physical variability was observed. The star also exhibited similar color–magnitude relations during the previous observing seasons.

Thus, we recorded the deepest and longest minimum of the star's brightness over the entire period of its photoelectric observations and the fastest brightening from its minimum ($9^m.5$) to its maximum ($9^m.0$) over a period comparable to the time the star stayed at minimum light, about 500 days.

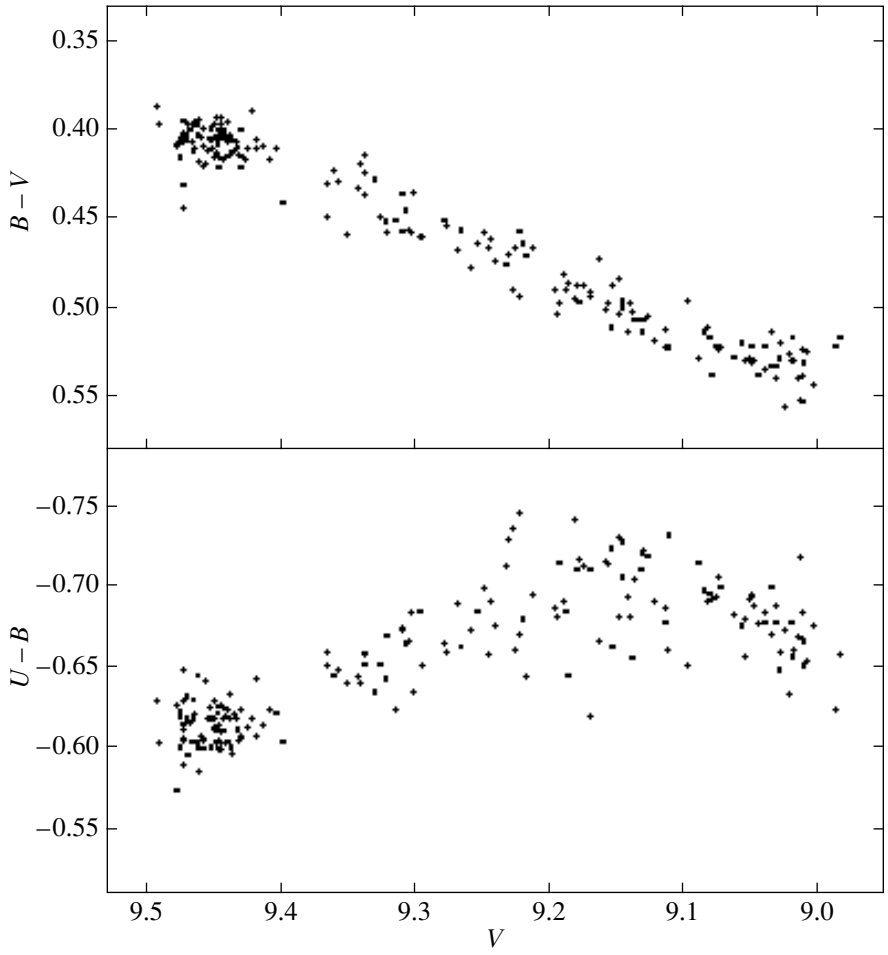

Fig. 2. Color—magnitude relations for A0535+26.

THE ADDITIONAL EMISSION

In general, the brightening episodes in early Be stars are attributed to envelope ejection. At minimum light, we observe the light from the star itself, while the contribution of the additional emission related to the circumstellar envelope increases as the brightness rises.

We attempted to compare the parameters of the additional emission responsible for the new brightening with those presented previously (Lyutyi and Zaitseva 2000). Note that, in the above paper, we considered the parameters of the additional emission averaged over a long time interval, almost five 1400-day quasi-periods, and only as a function of the brightness level, irrespective of whether the star was on the ascending or descending branch of the light curve. In contrast, in this paper, we consider a single episode of brightening from minimum to maximum.

The procedure for calculating the additional emission was similar to that used by Lyutyi and Zaitseva (2000). We assumed the minimum brightness to be $V_{\min} = 9\overset{m}{.}49$, $B_{\min} = 9\overset{m}{.}92$, $U_{\min} = 9\overset{m}{.}31$ and the color excesses corrected for interstellar reddening to be $E_{B-V} = 0\overset{m}{.}74$, $E_{U-B} = 0\overset{m}{.}48$. Using these values, we can determine the color indices of the additional emission responsible for the star's brightening since the end of 1998.

For this purpose, we transformed all of our observational data from magnitudes to fluxes using the absolute calibration by O'Dell *et al.* (1978) and averaged them by a moving average with a shift by half the bin. Subsequently, we plotted the color indices corrected for interstellar reddening on the two-color $(U-B)-(B-V)$ diagram. The additional emission at maximum light ($V_{\rm obs} = 9^m$) corresponds most closely to the emission of a plasma that is optically thick in the Balmer continuum ($T_{\rm e} \sim 1.5 \times 10^4$) and in the U, B, and V bands. The optical depth of the envelope in the continuum and lines decreases with declining brightness. In general, the change in the properties of the envelope during the last brightening in 1998–2002 was similar, within the error limits, to that found from the data averaged over a long time interval that included both the ascending and

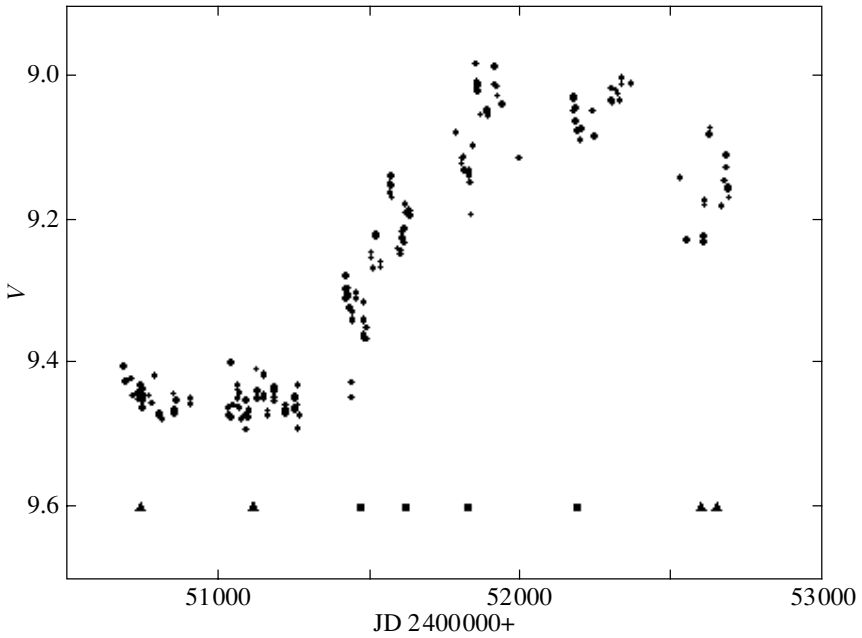

Fig. 3. V light curve for A0535+26. The triangles and squares indicate the times at which the spectrograms were taken by A.E. Tarasov and V.F. Esipov, respectively.

descending branches of the light curve (see Fig. 4 from Lyutyi and Zaitseva 2000).

THE DELAY OF THE Hα-LINE VARIATIONS WITH RESPECT TO THE CONTINUUM

During the last brightening episode, Hα spectrograms were taken by A.E. Tarasov at the Coude focus of the 2.6-m Crimean Astrophysical Observatory telescope and by V.F. Esipov with the 125-cm reflector at the Crimean Station of the SAI. The times at which these spectrograms were taken are indicated on the light curve in Fig. 3. The Hα emission profile (JD 2450755) persisted when the brightness reached its minimum. The next spectrograms were taken a year later, also at minimum light, and exhibited the Hα line in absorption. Thus, we may conclude that the absorption in the line appears no later than one year after the star reaches its minimum optical brightness. Another year later, the star began to brighten, the Hα line was in emission, and its equivalent width increased from 5 to 11 Å as the brightness rose. The Hα line also remained in emission during the fading that began in the fall of 2002. Thus, a delay of the line variations with respect to the continuum variations is observed. Unfortunately, the available spectroscopic data are scarce, and we can only conclude from them that this delay is no more than one year.

CONCLUSIONS AND DISCUSSION

The main results of our study are as follows:

(1) A rise in the brightness of the X-ray binary A0535+26 from its minimum ($9^m.5$) to its maximum ($9^m.0$) in ~500 days was recorded from 1998 until 2003, suggesting the beginning of the star's new activity phase.

(2) The physical parameters of the additional emission responsible for the new brightening match, within the error limits, those obtained from all of the averaged data, including both the ascending and descending branches of the light curve.

(3) The variations in the Hα line (the passage from emission to absorption and back) are delayed from those in the continuum by no more than one year.

In the previous observations of A0535+26, Clark *et al.* (1998) and Lyutyi and Zaitseva (2000) found a fairly high correlation between the variations in brightness and Hα equivalent width: $W_{H\alpha}$ increased with brightness. However, these authors pointed out that this dependence has a large scatter of data points. The delay between the line and continuum variations that we found can be responsible for this scatter. Moreover, Fig. 7 from Clark *et al.* (1998) shows that $W_{H\alpha}$ did not change and still remained at a low level in 1996 when the V brightness began to increase. This result may also be considered as evidence for the delay between the line and continuum variations.

The peculiarities of the brightness variations observed in A0535+26 in different periods (a long stay at minimum light, a fast brightening, and rapid outburst-like variations lasting for several weeks) are also typical of the fairly numerous class of early

Be stars in the Small Magellanic Cloud (Mennickent *et al.* 2002).

An ambiguous color–magnitude relation, in particular, the increase in $B-V$ with brightness, is characteristic of many Be stars whose light variations are attributable to the existence of an envelope. Thus, for example, Pavlovski *et al.* (1997) found such a relation for several early Be stars (V1293 Aql, HR 7807, etc.) from their UBV monitoring.

The closest analogy can be drawn between A0535+26 and the well-studied X-ray binary Be star X Per. Periods of low constant brightness were also observed in this star (Clark *et al.* 2001); they were accompanied by the passage from the emission to the absorption Hα line. The passage from the last emission line to the first absorption line at the minimum of 1990 lasted about 200 days. The absorption in the line appears at least 400 days after the star reaches its minimum optical brightness. Thus, the disk matter is found to gradually disappear over a period of 700 days, from the optical maximum to the last observed emission line (Roche *et al.* 1993). This time interval is comparable to that observed for A0535+26, for which our data reveal the transition from emission to absorption in about one year.

ACKNOWLEDGMENTS

I wish to thank V.F. Esipov and A.E. Tarasov, who provided their spectroscopic observations, and N.I. Ikonnikova, who reduced the spectrograms.

REFERENCES

1. J. S. Clark, V. M. Lyuty, G. V. Zaitseva, *et al.*, Mon. Not. R. Astron. Soc. **302**, 167 (1999).
2. J. S. Clark, A. E. Tarasov, A. T. Okazaki, *et al.*, Astron. Astrophys. **380**, 615 (2001).
3. J. S. Clark, A. E. Tarasov, I. A. Steele, *et al.*, Mon. Not. R. Astron. Soc. **294**, 165 (1998).
4. A. Giangrande, F. Giovannelli, C. Bartolini, *et al.*, Astron. Astrophys., Suppl. Ser. **40**, 289 (1980).
5. F. Giovannelli and Lola S. Graziati, Space Sci. Rev. **59**, 1 (1992).
6. Yu. N. Gnedin, G. V. Zaitseva, V. M. Larinov, *et al.*, Astron. Zh. **65**, 1196 (1988) [Sov. Astron. **32**, 624 (1988)].
7. V. M. Lyutyi and G. V. Zaitzeva, Pis'ma Astron. Zh. **26**, 13 (2000) [Astron. Lett. **26**, 9 (2000)].
8. V. M. Lyutyi, G. V. Zaitzeva, and I. D. Latysheva, Pis'ma Astron. Zh. **15**, 421 (1989) [Sov. Astron. Lett. **15**, 182 (1989)].
9. R. E. Mennickent, G. Pietrzynski, W. Gieren, and O. Szewezyk, Astron. Astrophys. **393**, 887 (2002).
10. S. L. O'Dell, J. J. Puschell, W. A. Stein, and J. W. Warner, Astrophys. J., Suppl. Ser. **38**, 267 (1978).
11. K. Pavlovski, P. Harmanec, H. Bozic, *et al.*, Astron. Astrophys. **125**, 75 (1997).
12. P. Roche, M. J. Coe, J. Fabregat, *et al.*, Astron. Astrophys. **270**, 122 (1993).
13. F. D. Rosenberg, C. J. Eiles, G. K. Skinner, and A. P. Wilmore, Nature **256**, 628 (1975).

Translated by N. Samus'

Astronomy Letters, Vol. 31, No. 2, 2005, pp. 109–116. Translated from Pis'ma v Astronomicheskiĭ Zhurnal, Vol. 31, No. 2, 2005, pp. 122–130.

Study of the Optical Variability of T Tau in the Period 1962–2003

S. Yu. Mel'nikov* and K. N. Grankin

Ulugh Beg Astronomical Institute, Academy of Sciences of Uzbekistan, Astronomicheskaya ul. 33, Tashkent, 700052 Uzbekistan

Received July 14, 2004

Abstract—We present the results of our long-term $UBVR$ observations of the star T Tauri performed at Mt. Maidanak Observatory from 1986 until 2003. These data, together with previous photoelectric observations of other authors, suggest that the long-term variations of the light curve are not periodic, but have a cycle with a time scale of 6–9 yr. The light curve also exhibits slower variations with time scales of ~30–40 yr. We confirm the existence of periodic brightness variations with a period of $P = 2\overset{\mathrm{d}}{.}798$ over many years; this process is peculiar in that the phase and shape of the phase curve change from season to season. We analyze the color behavior of the star. We found evidence of a strong flare occurred on October 5, 1999, when the brightness of the star reached $9\overset{m}{.}22$. This is the strongest flare recorded during its photoelectric observations. © *2005 Pleiades Publishing, Inc.*

Key words: *stars—variable and peculiar.*

INTRODUCTION

Recent studies have shown that the star T Tau, which provided the name for a whole class of young stars, is a unique object in many respects. First of all, it is a triple system in which the infrared component T Tau S lies $0\overset{''}{.}7$ south of the northern optical component T Tau N (Dyck *et al.* 1982); the southern component, in turn, is a binary system (Koresco 2000). In the above paper, the separation between the infrared components of T Tau S was estimated from the 1997 observations to be $\sim 0\overset{''}{.}05$. Loinard *et al.* (2003) presented evidence for a considerable relative motion between the infrared components of T Tau S, which may suggest that the low-mass component T Tau Sb is ejected from the system. Solf and Böhm (1999) found that both T Tau N and T Tau S have mutually perpendicular bipolar outflows. These authors suggested a model in which T Tau N is surrounded by an optically thick circumstellar disk viewed face-on, while the circumstellar disk of T Tau S is seen almost edge-on. The disk of T Tau N seen face-on obscures the optical light from T Tau S; as a result, we observe T Tau S only as an infrared source.

The optical photometry of T Tau N since the discovery of its variability in 1852 reveals a complex brightness behavior of the northern component (below, all of our discussions of the optical variability refer precisely to T Tau N). Studies of the historical light curve using photographic plates taken from 1858 until 1952 showed that, before 1917, the star exhibited significant variability with an amplitude of ~ 2–3^m (Lozinskii 1949; Beck and Simon 2001). After 1917, the variability decreased significantly in amplitude, and the star's brightness varied between $9\overset{m}{.}6$ and $10\overset{m}{.}6$ (in visual light) until the end of the period covered by photographic plates. The star's photoelectric photometry started in 1962 showed that, in the early 1960s, T Tau was in a minimum state, and its brightness varied between $10\overset{m}{.}4$ and $10\overset{m}{.}6$ (in the V band). Subsequently, the brightness began to gradually rise and reached its maximum state ($\sim 9\overset{m}{.}8$) at the end of 1983 (Zaitseva 1989). After 1983, the star's brightness rise gave way to a decline, and this decline in the yearly mean brightness was traced until 1997 (Ismailov and Samus' 2003). Periodic variations with a shorter period, ~2000 days (Zaitseva 1989), are superimposed on these long-term variations in the mean brightness. Based on the observations obtained by different authors before 1997 inclusive, Ismailov and Samus' (2003) derived the mean period of these variations: $P = 2200^{\mathrm{d}} \pm 150$ (about 6 years). In addition, short-period brightness variations were detected. Herbst *et al.* (1986) reported the existence of a 2.8-day period of brightness variations that may be related to the star's rotation period. At the same time, Zaitseva (1990) showed that although this period was present in the interval 1976–1988, it did not preserve its initial phase. Clearly, this behavior of the optical variability of T Tau is of interest for further studies.

*E-mail: stas@astrin.uzsci.net

1063-7737/05/3102-0109$26.00

In this paper, we discuss the photoelectric photometry of T Tau. We used our own long-term photometry obtained at Mt. Maidanak Observatory and the photometry from the Wesleyan database (Herbst *et al.* 1994) accessible via the Internet. Apart from our Mt. Maidanak observations (~700 measurements), the Wesleyan database contains about 2000 observations by other authors. In addition to unpublished photometry, this database includes the observations by Bouvier *et al.* (1988), Zaitseva (1977), Kardopolov and Filip'ev (1985), Rydgren *et al.* (1984), Herbst *et al.* (1983), Herbst and Koret (1988), and Holtzman *et al.* (1986). The collected $UBVR$ observations span the period from 1962 until 2003.

$UBVR$ PHOTOMETRY

Our absolute photometry was performed with a single-channel photoelectric photometer attached to a 48-cm AZT-14 reflector at Mt. Maidanak observatory. The detector in the pulse-counting photometer was a FEU-79 photomultiplier tube. Our photometric data were reduced to Johnson's international $UBVR$ system using standard reduction techniques.

In our observations, we used a differential method, and the comparison star was HD 27560 = BD + 19°704 ($V = 8\overset{m}{.}376$, $U - B = -0\overset{m}{.}065$, $B - V = 0\overset{m}{.}412$, $V - R = 0\overset{m}{.}384$). In general, we made one $(U)BVR$ measurement per night (the parentheses for the U filter imply that our BVR observations were not always accompanied by a U measurement). In this mode of observations, we observed no check star, and our observations of the variable star were checked for correctness by the counting stability for the comparison star. We obtained 715 $(U)BVR$ observations of the variable star from 1986 until 2003. The rms errors of a single measurement were $\sigma(V) = \sigma(V - R) = 0\overset{m}{.}01$, $\sigma(U - B) = 0\overset{m}{.}03$, and $\sigma(B - V) = 0\overset{m}{.}015$. The statistics of our observations is presented in the table, which contains the range of Julian dates for each observing season (JD) and the ranges of the V and color variations (the number of observations is given in parentheses after each value).

LONG-TERM BRIGHTNESS VARIATIONS

The combined V-band light curve for the period from 1962 until 2003 is presented in Fig. 1. As was noted above, the star's mean brightness gradually rose from $10\overset{m}{.}6$ after 1962 to $9\overset{m}{.}8$ at the end of 1983; subsequently, the brightness began to gradually decline. Our data show that the mean brightness continued to decline until 2001. In 2000–2001, the brightness dropped to almost $10\overset{m}{.}2$, and a local minimum was observed, but the star's brightness rose again in 2002–2003. It is not yet clear whether this brightening is only local and the star's mean brightness will continue to decline or the epoch of decline in mean brightness again gave way to its rise. Such long-term brightness variations are also seen in the observations by Lozinskiĭ (1949). Thus, two stages can be identified in the photometric history of T Tau: (1) from 1858 until 1917, when the star exhibited enhanced activity and its brightness varied with an amplitude of $\sim 2^m$ and (2) the period of smooth mean-brightness variations that began in 1917 and continues at present.

Cycles with a mean duration of about 2200 days (Ismailov and Samus' 2003) are seen against the background of these long-term variations in the mean brightness. Ismailov and Samus' (2003) determined the times of five minima that satisfactorily agree with this period. The times of the two last minima are JD 2447167 (1988) and JD 2449280 (1993). We attempted to improve this period using our Mt. Maidanak observations obtained in 1998–2003. For this purpose, we added our observations to the combined light curve, drew the enveloping curves through the upper and lower points of the combined light curve, and derived the times of the three last minima located at epochs with good observational coverage: JD 2446750 (1986), JD 2448860 (1992), and JD 2452150 (2001). The 1986–2003 part of the light curve constructed from our Mt. Maidanak observations is shown in more detail in Fig. 2. The times of the first two minima (1986, 1992) that we derived in this study slightly differ from those determined by Ismailov and Samus' (2003), but the difference between these times of minima coincides, within the error limits, with the period obtained by Ismailov and Samus'. At the same time, the difference between the times of the two last minima, JD 2448860 (1992) and JD 2452150 (2001), is about 3300 days, which is a factor of 1.5 larger than the period determined from the previous minima. If the epoch of the next-to-last minimum in the paper by Ismailov and Samus' (2003) is assumed to be closer to the true value than our value determined here, then the difference between the epochs of the two last minima will be 2870 days, and its deviation from the 2200-day period will still be several times larger than the error with which the 2200-day period was determined. Thus, we can assume that these variations are not strictly periodic, but rather cyclic in pattern.

THE $2\overset{d}{.}798$-DAY PERIOD

To find periodic brightness variations with a period within 2–10 days, we analyzed the individual observing seasons from 1987 until 2003. For this purpose,

Statistics of the observations of T Tau at Mt. Maidanak in 1986–2003

Year	JD	ΔV	$\Delta(U-B)$	$\Delta(B-V)$	$\Delta(V-R_J)$
1986	46665–46757	9.937–10.043(13)	0.167–0.731(13)	1.143–1.239(13)	1.115–1.192(13)
1987	47030–47173	9.850–10.050(44)	0.245–0.663(42)	1.123–1.209(44)	1.097–1.174(43)
1988	47372–47549	9.789–10.026(92)	0.224–0.663(59)	1.114–1.220(92)	1.035–1.143(92)
1989	47767–47887	9.752–9.998(51)	0.272–0.685(31)	1.097–1.216(51)	0.985–1.175(51)
1990	48109–48265	9.805–9.978(64)	0.046–0.650(35)	1.083–1.243(64)	1.086–1.183(64)
1991	48460–48589	9.807–10.037(69)	0.358–0.698(32)	1.103–1.255(69)	1.061–1.166(69)
1992	48844–48956	9.930–10.164(53)	0.247–0.684(17)	0.918–1.320(53)	0.956–1.161(52)
1993	49201–49287	9.881–10.088(59)	0.628(1)	1.138–1.263(59)	1.106–1.172(59)
1994	49631–49644	9.882–10.020(8)		1.114–1.205(8)	1.128–1.167(8)
1995	49938–50046	9.849–10.080(45)	0.154–0.662(16)	1.068–1.226(45)	1.094–1.167(45)
1996	50304–50415	9.775–10.059(33)	0.161–0.522(8)	1.018–1.224(33)	1.117–1.186(32)
1997	50680–50725	9.840–10.035(31)	0.376–0.547(3)	1.056–1.223(31)	1.078–1.164(31)
1998	51027–51109	9.765–10.075(23)	0.341–0.485(4)	1.030–1.187(23)	1.084–1.160(23)
1999	51392–51529	9.862–10.123(49)	−0.034–0.631(35)	1.089–1.202(49)	1.123–1.205(49)
2000	51782–51841	9.935–10.163(15)	0.181–0.549(8)	1.128–1.214(15)	1.129–1.217(15)
2001	52130–52176	9.973–10.174(17)	0.377–0.441(2)	1.149–1.248(17)	1.140–1.202(17)
2002	52556–52609	9.890–10.110(18)		1.054–1.187(18)	1.126–1.185(18)
2003	52882–52937	9.837–10.138(31)	−0.003–0.757(29)	1.097–1.319(31)	1.067–1.191(31)

we used the CLEAN algorithm adapted for analyzing univariate unevenly spaced time series (Roberts *et al.* 1987; Terebizh 1992). At the same time, we obtained comparatively few observations for T Tau in 1986, 1994, and 2000–2002; therefore, we did not analyze the data series obtained during these seasons.

A numerical analysis of our homogeneous observations confirms the existence of periodic variations with a 2.798-day period. The phased light curves in Fig. 3 were computed with the ephemeris from Herbst *et al.* (1986), i.e., for the initial phase JD = 2440000.0. These plots show that the period does not preserve its strict phase from season to season. For example, let us consider two neighboring years, 1991 and 1992. Whereas the minimum state of the light curve in 1991 occurred at phase 0.3, in 1992 it occurred at phase 0.7. This phenomenon was first pointed out by Zaitseva (1990), who found phase changes at four epochs: 1976–1977, 1985–1986, 1987, and 1988.

We also deemed it necessary to give the phased curves for the seasons when we failed to detected any periodic brightness variations in T Tau. As an example, Fig. 3 shows the phased curve for 1990. Despite the fairly large statistics (61 data points were obtained in this year), neither the numerical analysis of the time series nor the construction of the phased curve reveals the $2^d.798$ period.

At the same time, it remains unclear how the phase shifts. For example, in certain seasons (1991, 1995, 1999), a slight splitting of the phased curves was observed, which may be evidence for a change in the phase during the observing season. We attempted to detect this process by constructing the phased curves for the individual parts of the time series within each season. However, we failed to establish how the phase changed, abruptly or gradually, during a relatively long time interval. A third alternative where the periodic process completely disappears from the light curve and then reappears, but at a different phase, is possible. This assumption is supported by the presence of seasons when the $2^d.798$ period is not detected (e.g., 1990). 1998 may be an epoch when the birth of a periodic process with a new phase can be seen. Figure 3 shows that the periodic process in this year is not distinct enough, and the shape of the phased curve for this year differs markedly from that of the other phased curves. Whereas the periodic process can be roughly described by a sine wave for other seasons, a small sharp minimum is observed in the

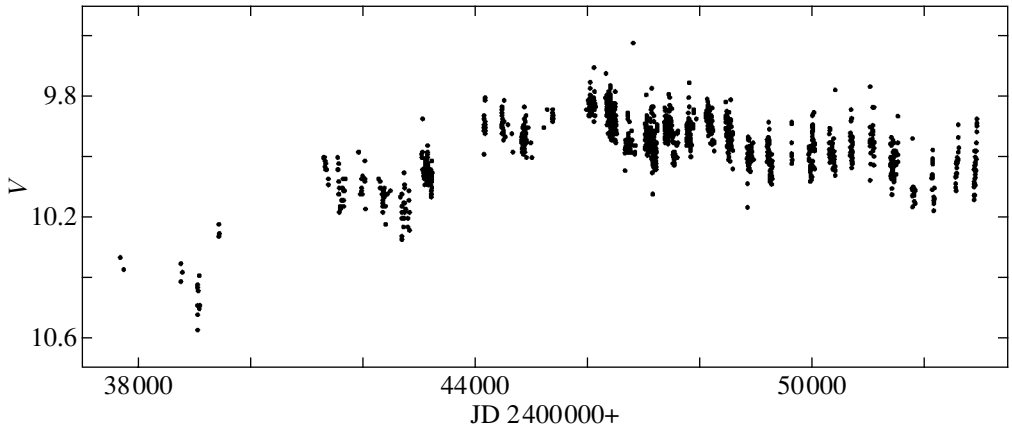

Fig. 1. Combined light curve of T Tauri for 1962–2003, as constructed from the observations by different authors.

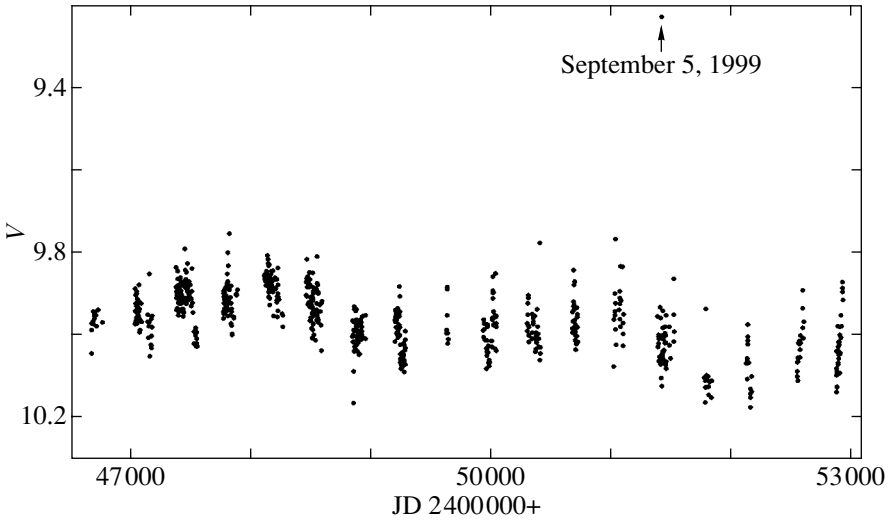

Fig. 2. Light curve of T Tauri for 1986–2003, as constructed from our Mt. Maidanak photoelectric photometry. The arrow indicates the possible flare of T Tauri on September 5, 1999.

phased curve for 1998, after which the star gradually returned to the state of maximum light. It can also be seen that relatively few data points in 1998 correspond to the minimum brightness state.

We also attempted to detect the $2\overset{d}{.}798$-day period in the appearance of an ultraviolet excess. For this purpose, we set the phases of all V-band minima equal to zero and recalculated the phases within each season. Thus, we reconciled the phases of the periodic process in different seasons to better reveal this period. To construct the corresponding combined phased curve, we used only the seasons when T Tau exhibited the periodic process. Using the derived phases, we constructed a similar combined phased curve for the color index $U-B$, but failed to detect any correlation between the $U-B$ variations and the $2\overset{d}{.}8$ period in the phased curve. Thus, the appearance of an ultraviolet excess does not correlate with the existing $2\overset{d}{.}8$-day period, which may be related to the star's rotation period.

THE COLOR BEHAVIOR

The combined $V-(U-B)$, $V-(B-V)$, and $V-(V-R)$ diagrams are shown in Fig. 4. We constructed these diagrams using not only the Mt. Maidanak observations obtained from 1984 until 2002, but also the observations by Zaitseva (1977, 1989). Collectively, these observations cover a wider range of brightness variations. All diagrams were constructed on the same scale. The lower group of data points that is present in the $V-(U-B)$, $V-(B-V)$ diagrams and absent in the $V-(V-R)$ diagram was taken from the paper by Zaitseva (1977), where the observations only in the U, B, V bands are given.

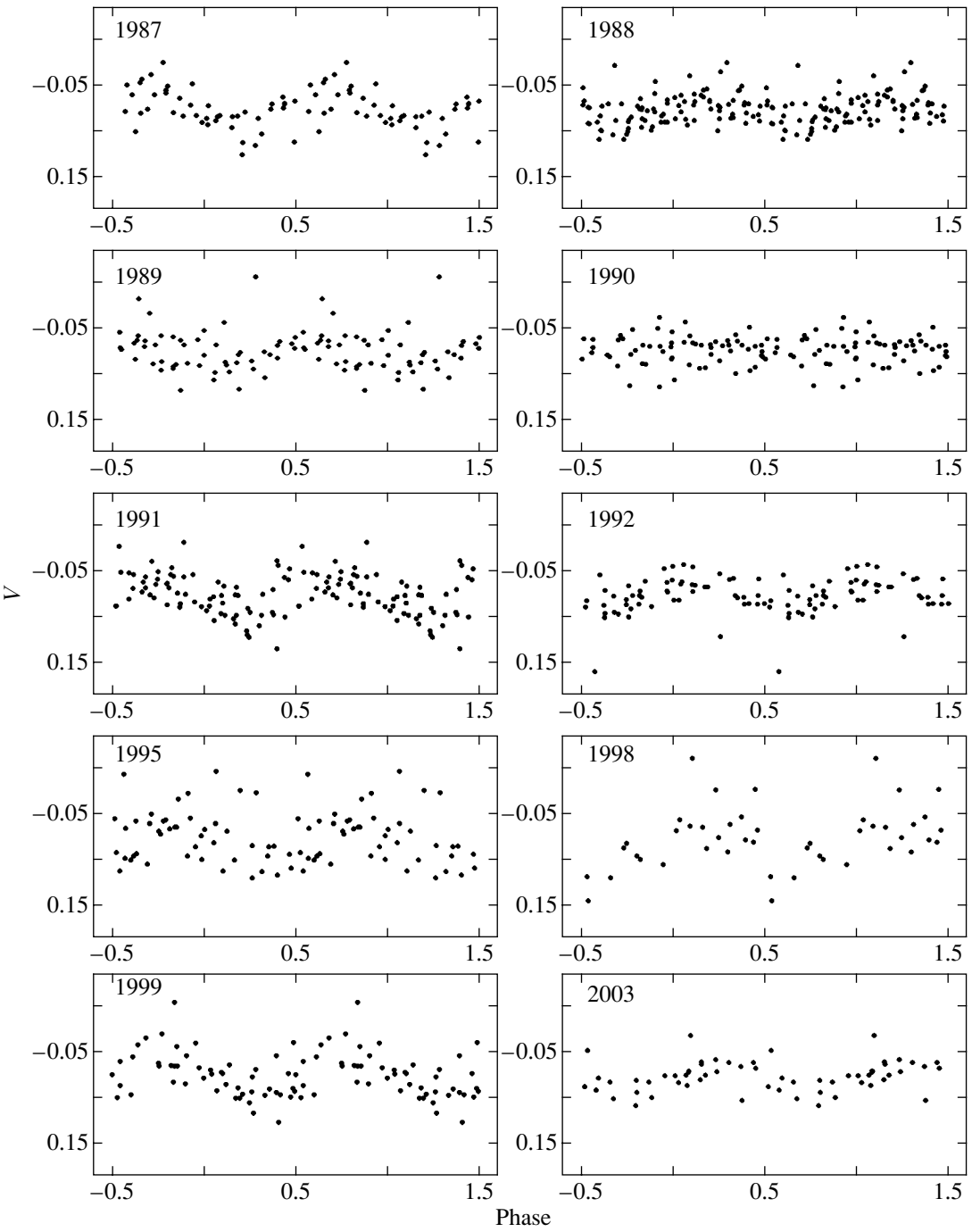

Fig. 3. Phased light curves of T Tauri folded with the $2^{d}.798$ period and the same initial epoch. The initial epoch is JD 2440000 from Herbst *et al.* (1986).

It is clearly seen from Fig. 4 that the $U-B$ color is subject to the largest variability, exhibiting the permanent appearance of an ultraviolet excess. For this reason, as we see from the figure, the $U-B$ variations poorly correlate with the V brightness variations, and the $V-(U-B)$ diagram greatly differs in appearance from the $V-(B-V)$ and $V-(V-R)$ diagrams. This phenomenon was described by Zaitseva (1989). The bluest color indices, $U-B=-0^{m}.17$ and $-0^{m}.4$, were recorded at JD 2443061 (October 9, 1976, the data point was taken from the paper by Zaitseva (1977)) and JD 2451427 (September 5, 1999, the Mt. Maidanak observations), respectively; we will discuss the observations at JD 2451427 below. Without these data points, the $U-B$ color varied between $-0^{m}.03$ and $0^{m}.86$.

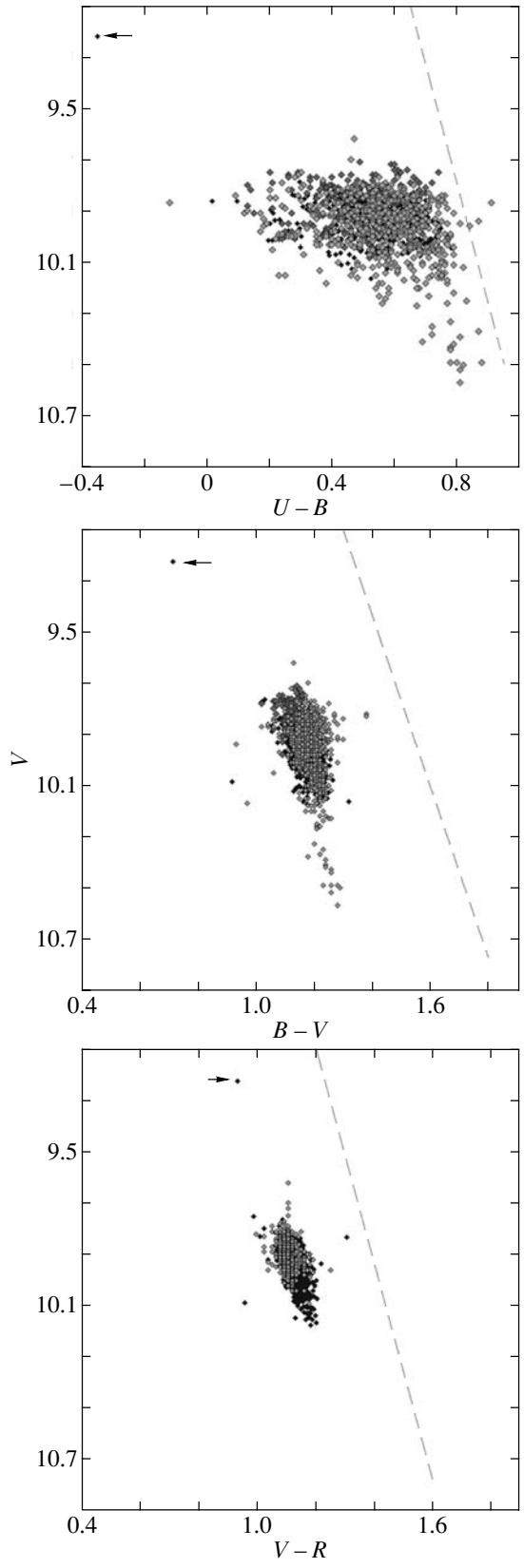

Fig. 4. Color–magnitude diagrams for T Tauri. The dashed straight line represents the interstellar reddening line. The arrows indicate the flare on September 5, 1999.

Note the change in the behavior of the $U-B$ color index with declining brightness (Fig. 4). There were virtually no ultraviolet flares from 1962 until 1972 (JD 2437675–2441684), when the star was fainter than $V = 10^{m}.1$. At this time, the $U-B$ color was, on average, redder than $0^{m}.7$, and it varied approximately along the interstellar reddening line. If we take the reddest $U-B$ values as the star's color indices distorted only by interstellar reddening and use the normal reddening law, then after dereddening, we will find that the star crosses the zero reddening sequence in the $(U-B)$–$(B-V)$ diagram near the spectral type K1, in agreement with the spectral type K0 derived from spectral lines (Herbig 1977).

We believe that the disappearance of ultraviolet flares when the star was fainter than $V = 10^{m}.1$ can be explained in terms of eclipses. If we assume that the fading during this period resulted from the star's eclipse by a circumstellar cloud, then the region where the excess ultraviolet radiation originated was subject to the strongest absorption, and this region was completely hidden from an Earth-based observer. The eclipsing mechanism is supported by the fact that the $B-V$ color in the $V-(B-V)$ diagram during this period varied along the interstellar reddening line and by the behavior of $U-B$ in the minimum brightness state.

In contrast to $U-B$, the $B-V$ and $V-R$ color indices depend more strongly on the brightness level and vary approximately along the reddening line with declining brightness. It may also be noted that the scatter of data points in the $V-(B-V)$ diagram is larger than that in the $V-(V-R)$ diagram. This is also confirmed by numerical estimates. Whereas the correlation coefficient for the $V-(B-V)$ relation is 0.5, the correlation coefficient for $V-(V-R)$ is about 0.7. We believe that this decrease in the scatter of data points in the color–magnitude diagram toward the longer wavelengths can stem from the fact that the nonstationary accretion to which the large U-band variability is attributed also affects the brightness in the B, V, and R bands, but the contribution of this process to the star's light decreases with increasing wavelength.

THE OPTICAL FLARE OF SEPTEMBER 5, 1999

On September 5, 1999 (JD 2451427), T Tau was unusually bright, $V = 9^{m}.224$, and its color indices were $U-B = -0^{m}.402$, $B-V = 0^{m}.713$, and $V-R = 0^{m}.931$, while its mean brightness and colors at neighboring dates were $V \sim 10^{m}.05$, $U-B \sim 0^{m}.5$, $B-V \sim 1^{m}.18$, and $V-R \sim 1^{m}.18$. This data point is not shown in Fig. 1 but is marked by an arrow in Figs. 2 and 3. The color indices had extremely low

values that had never been observed at the epoch of photoelectric photometry; at the same time, however, they approximately lie on the extension of the color relations in the $B-V$ and $V-R$ diagrams. A thorough check of the primary photometric data and the log of reductions shows that the fluxes from the comparison star, the background, and the neighboring program stars were normal, and the reductions were performed using standard procedures. Unfortunately, we failed to monitor this event, since we did not reduce and analyze our observations in real time and discovered the flare after the event ended. Furthermore, we failed to find additional published photometry at this date to confirm the existence of such a strong flare.

We believe that T Tau experienced a strong flare on September 5, 1999, one that was accompanied by a general bluing of its color indices. A comparison of the color indices during the flare with those in the normal state near September 5, 1999, shows that the amplitude of the flare decreased from U to R ($\Delta U = 2\overset{m}{.}19$, $\Delta B^m = 1.29$, $\Delta V = 0\overset{m}{.}83$, $\Delta R = 0\overset{m}{.}58$), while the ratios of the amplitudes in the U, B, and R bands to the V-band amplitude were 2.6, 1.5, and 0.7, respectively. An analysis of this flare with regard to the $2\overset{d}{.}798$-day period indicates that this periodic process was present in 1999 with a good signal-to-noise ratio, and the flare occurred on the ascending branch of the phased curve (Fig. 3) at phase $\phi = 0.13$.

Optical flares of T Tau have already been detected in the history of its photometric studies. During an optical monitoring of T Tau, Kilyachkov and Shevchenko (1976) recorded a flare on February 15, 1974 ($V_{\max} = 9\overset{m}{.}75$). Using five-color ($U$, β, B, V, R) photometry, they managed to derive more detailed photometric parameters of this flare. The duration of the flare was about 2 h. The maximum amplitude of the flare in the U band was $1\overset{m}{.}30$, and the minimal $U-B$ color index during the flare reached $-0\overset{m}{.}35$ (close to the $U-B$ color index for the flare on September 5, 1999). The ratios of the amplitudes in the U, B, R bands to the V-band amplitude were, respectively, 4.6, 1.1, and 0.6 (Kilyachkov and Shevchenko 1976). Thus, the common features of the 1976 and 1999 flares were a maximum amplitude in the U band and a significant decrease of the flare amplitudes toward the longer wavelengths.

A number of studies have shown that flares occur not only on classical T Tauri stars (CTTSs), but on weak-line T Tauri stars (WTTSs) as well (see Gahm (1990) and references therein). Stelzer *et al.* (2003) found eight flares during their optical monitoring of the WTTS V410 Tau (November 2001). Their measurements were made in both the Strömgren system and UBV. All of these flares also have a maximum amplitudes in the U band, and the amplitude decreases with increasing wavelength. This star shows a $1\overset{d}{.}87$ period on its light curve related to the star's rotation period. On the phased light curve, these flares lie on the ascending branch, and their phases range from 0.14 to 0.21.

Although the flares of T Tau and V410 Tau are similar in that the amplitude (in magnitudes) is at a maximum in the ultraviolet, the nature of their flares may be different. Stelzer *et al.* (2003) noted that the energy distribution for the flares of V410 Tau is in good agreement with the empirical relation derived for UV Ceti flare stars (Lacy *et al.* 1976). Comparing the statistical parameters for the flares of WTTSs and CTTSs, Gahm (1990) showed that the flares for these two types of stars could be divided into two groups and that they can differ in nature. Gahm (1990) assumes that the flares of CTTSs could be produced by accretion processes in the boundary layer of their accretion disks, while the mechanism of WTTS flares is similar to that suggested for ordinary flare stars.

As regards the positions of flares on the phased light curve, under the conditions of poor statistics, the similarity between the phases of the flares on V410 Tau and T Tau may be a chance coincidence.

CONCLUSIONS

Our study of the long-term photometric behavior of the star T Tauri has shown the following.

(1) The photoelectric light curve of T Tau exhibits long-term cyclic brightness variations on a time scale of 6–9 years. In addition, portions of a gradual rise and decline in the mean brightness with a maximum in 1983 can be seen in the 40-year-long light curve (1962–2003). These portions can be fragments of another periodic process with a variation time scale of about 30–40 years.

(2) Although the brightness variations with a period of $2\overset{d}{.}798$ are found in many parts of the light curve that we obtained during different seasons, the pattern of these periodic variations is rather complex. The salient feature is that the periodic variations do not preserve a constant phase from season to season. The shape of the phased curve also changes. There are epochs when no periodic process is found on the light curve. These may be the time intervals after which the periodic variations resume, but at a different phase.

(3) The correlation between the V-band brightness variations and the $U-B$, $B-V$, and $V-R$ color variations becomes stronger with increasing wavelength. The behavior of $U-B$ is virtually uncorrelated with the V-band brightness, since this color index changes abruptly due to the permanent appearance of an ultraviolet excess. However, the ultraviolet flares virtually disappeared when the star became fainter than $V > 10\overset{m}{.}1$ (as implied by the

observations of Zaitseva (1989)). We believe that the ultraviolet flares could disappear because of a circumstellar cloud eclipsing the region where the excess ultraviolet radiation originates.

(4) A strong flare was observed on September 5, 1999; its amplitude was at a maximum in the U band. This was the strongest flare in the entire history of photoelectric observations of T Tau. The star's brightness during the flare reached $V = 9^m.22$, while its brightness during the maximum of 1983 was $V \approx 9^m.8$.

ACKNOWLEDGMENTS

We wish to thank S.A. Lamzin for helpful discussions of the results obtained. We are grateful to M.A. Ibragimov, O.V. Ezhkova, and S.D. Yakubov, who took part in the observations.

REFERENCES

1. T. L. Beck and M. Simon, Astron. J. **122**, 413 (2001).
2. J. Bouvier, C. Bertout, and P. Boucher, Astron. Astrophys., Suppl. Ser. **75**, 1 (1988).
3. H. M. Dyck, T. Simon, and B. Zuckerman, Astrophys. J. **255**, L103 (1982).
4. G. F. Gahm, *Flare Stars in Star Clusters, Associations and the Solar Vicinity, IAV Symp. No. 137*, Ed. by L. V. Mirzoyan, B. R. Pettersen, and M. K. Tsvetkov (Kluwer Acad. Publ., Dordrecht, 1990), p. 193.
5. G. Herbig, Astrophys. J. **214**, 747 (1977).
6. W. Herbst, J. F. Booth, P. F. Ghugainov, *et al.*, Astrophys. J. **310**, L71 (1986).
7. W. Herbst, D. K. Herbst, E. J. Grossman, *et al.*, Astron. J. **108**, 1906 (1994).
8. W. Herbst, J. A. Holtzman, and R. S. Klasky, Astron. J. **88**, 1648 (1983).
9. W. Herbst and D. L. Koret, Astron. J. **96**, 1949 (1988).
10. J. Holtzman, W. Herbst, and J. Booth, Astron. J. **92**, 1387 (1986).
11. N. Z. Ismailov and N. N. Samus', Inform. Bull. Var. Stars, No. 5382 (2003).
12. V. I. Kardopolov and G. K. Filip'ev, Perem. Zvezdy **22**, 103 (1985).
13. N. N. Kilyachkov and V. S. Shevchenko, Pis'ma Astron. Zh. **2**, 494 (1976) [Sov. Astron. Lett. **2**, 193 (1976)].
14. C. D. Koresko, Astrophys. J. **531**, L147 (2000).
15. C. H. Lacy, T. J. Moffet, and D. S. Evans, Astrophys. J., Suppl. Ser. **30**, 85 (1976).
16. L. Loinard, L. F. Rodrígues, and M. I. Rodrígues, Astrophys. J. **587**, L47 (2003).
17. A. M. Lozinskiĭ, Perem. Zvezdy **7**, 76 (1949).
18. D. H. Roberts, J. Lehar, and J. W. Dreher, Astron. J. **93**, 968 (1987).
19. A. E. Rydgren, J. T. Schmelz, D. S. Zak, *et al.*, Publ. Naval Observ. **25**, part 1 (1984).
20. J. Solf and K.-H. Böhm, Astrophys. J. **523**, 709 (1999).
21. B. Stelzer, M. Fernández, V. M. Costa, *et al.*, Astron. Astrophys. **411**, 517 (2003).
22. V. Yu. Terebizh, *Time Series Analysis in Astrophysics* (Nauka, Moscow, 1992) [in Russian].
23. G. V. Zaitseva, Astrofiz. **14**, 17 (1977).
24. G. V. Zaitseva, Astrofiz. **31**, 489 (1989).
25. G. V. Zaitseva, *Flare Stars in Star Clusters, Associations, and the Solar Vicinity. IAU Symp. No. 137*, Ed. by L. V. Mirzoyan, B. R. Pettersen, and M. K. Tsvetkov (Kluwer Acad. Publ., Dordrecht, 1990), p. 173.

Translated by N. Samus'

Astronomy Letters, Vol. 31, No. 2, 2005, pp. 117–128. Translated from Pis'ma v Astronomicheskiĭ Zhurnal, Vol. 31, No. 2, 2005, pp. 131–142.

Photometric Elements, Apsidal Motion, and a Third Body in the Eclipsing Binary HP Aur

V. S. Kozyreva, A. V. Kusakin, and Kh. F. Khaliullin*

Sternberg Astronomical Institute, Universitetskiĭ pr. 13, Moscow, 119992 Russia

Received June 17, 2004

Abstract—Highly accurate $WBVR$ photometric measurements of the eclipsing binary HP Aur were performed in 2002–2003 with the 48-cm AZT-14 reflector at the Tien-Shan High-Altitude Observatory to determine the rate of apsidal motion. A consistent system of physical and geometrical parameters of the components and the binary as a whole has been constructed for the first time by analyzing these new measurements together with other published data: we determined their radii ($R_1 = 1.05R_\odot$, $R_2 = 0.82R_\odot$) and luminosities ($L_1 = 1.10L_\odot$, $L_2 = 0.46L_\odot$), spectral types (G2V + G8V) and surface gravities ($\log g_1 = 4.38$, $\log g_2 = 4.51$), age ($t = 9.5 \times 10^9$ yr), and the distance to the binary ($d = 197$ pc). We detected an ultraviolet excess in the spectra of both components, $\Delta(W - B) \simeq -0^m.25$, that is probably attributable to a metal deficiency in the atmospheres of these stars. In this system of two solar-type stars, we found a third body with the mass $M_3 \sin i_3^3 = 0.17M_\odot$ that revolved with the period $P_3 = 13.7$ yr around the eclipsing binary in a highly eccentric elliptical orbit: $e_3 = 0.70$ and $A_3 \sin i_3 \simeq 7$ AU. The orbit of the eclipsing binary itself was shown to be also elliptical, but with a low eccentricity ($e = 0.0025(5)$), while apsidal motion with a period $U_{\rm obs} > 80$ yr was observed at a theoretically expected period $U_{\rm th} \approx 92$ yr. At least 20 to 30 more years of photoelectric measurements of this star will be required to reliably determine $U_{\rm obs}$. © *2005 Pleiades Publishing, Inc.*

Key words: *stars—variable and peculiar, eclipsing binary stars, apsidal motion, photometric elements, third body in system.*

INTRODUCTION

The variability of the eclipsing binary HP Aur (HDE 280 603 = GSC 2401.1263 = BV 185, Sp = G2V + G8V, $V_{\max} = 11^m.20$) was discovered from photographic observations by Strohmeier (1958). Subsequently, this star was studied photographically by Perova (1960), Splittgerber (1971), and Mallama *et al.* (1977). The first photoelectric B and V light curve was obtained by Meinunger (1980), who found the orbit of this binary to be eccentric. The photometric elements from the solution of Meinunger's light curve were published by Giuricin *et al.* (1983) and Botsula (1987). Based on their UBV photoelectric observations, Liu *et al.* (1989) studied the short-period light variations in the binary and presented the results of the solution of their light curve. In 1985, Kozyreva (1990) obtained multicolor $WBVR$ photoelectric light curves that allowed her to determine the photometric and absolute elements and detected apsidal motion of the orbit. Having analyzed all of the available data, Wolf and Sarounova (1996) suspected the existence of a light-time effect at the times of minima with a period of about 20 years and an amplitude of $\sim 0^d.01$.

The photometric elements derived from the light-curve solution for HP Aur by different authors differ significantly. The difference in radii reaches 30–50%. In his paper devoted to a detailed spectroscopic analysis of HP Aur and several other solar-type stars, Popper (2000) particularly emphasized the mutual discrepancy between the photometric elements from different published sources. As a result, the absolute parameters of the components are determined with large errors, and their spectral types cannot be established even from spectroscopic measurements. This is because the determination of the line equivalent widths for the components and, accordingly, their spectral types depends on the relative contribution of the components to the intensity of the neighboring continuum, i.e., on the ratio L_2/L_1 that can be determined by analyzing the light curves.

To resolve the existing contradictions and to determine more accurate geometrical and physical parameters of the binary, we have continued our photoelectric studies of HP Aur.

*E-mail: valq@sai.msu.ru

1063-7737/05/3102-0117$26.00

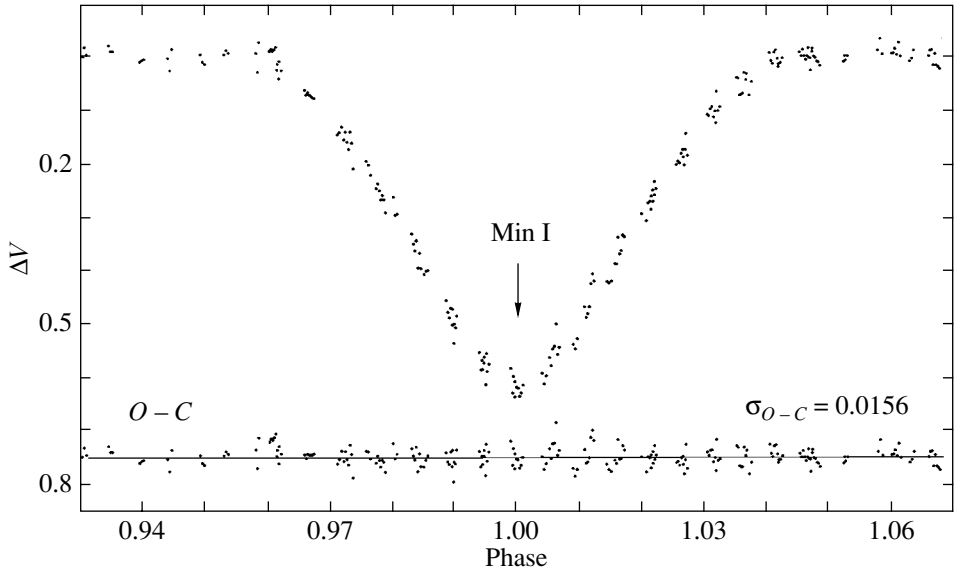

Fig. 1. The V light curve for HP Aur near the primary minimum derived from our photoelectric observations in 2002–2003. Residuals of the observations (O) from the theoretical curve (C) constructed with the photometric elements from Table 3 are shown below.

OBSERVATIONS

The photoelectric measurements of HP Aur in the $WBVR$ photometric system (Khaliullin *et al.* 1985) were performed by Kozyreva (1990) in 1985 at Tien-Shan High-Altitude Astronomical Observatory of the Sternberg Astronomical Institute (Moscow State University) using a photoelectric photometer attached to the 48-cm AZT-14 reflector. We continued these measurements in 2002–2003 with the same instrumentation and, mostly, with the same comparison star HD 280604. Only the observations in December 2003 were performed with the comparison star HD 33688. Within the limits of the measurement errors ($\sigma^V_{\rm obs} \leq 0^m.008$), no light variations were found in these standard stars.

Our differential measurements of HP Aur are accessible via the Internet at http//lnfm1.sai.msu.ru/~valq (broadband photometry). They were corrected for atmospheric extinction using a technique described by Moshkalev and Khaliullin (1985) and reduced to the system of the $WBVR$ catalog (Kornilov *et al.* 1991). The V light curves for HP Aur near the primary and secondary minima constructed from our observations in 2002–2003 are shown in Figs. 1 and 2, respectively.

PHOTOMETRIC AND ABSOLUTE ELEMENTS

To determine the photometric elements, we first analyzed a relatively compact (in time) set of our new V-band measurements. Since the reflection and ellipticity (<0.01) effects were negligible, we used standard light-curve rectification methods (Martynov 1971). Table 1 presents, in standard notation, the photometric elements of HP Aur that we found by the iterative method of differential corrections (Khaliullina and Khaliullin 1984) from an analysis of our observations in 2002–2003 for several fixed eccentricities e (in Table 1 and below, the rms errors of the sought elements are given in parentheses). The accuracy of the individual light curves is not very high due to the physical light fluctuations in the star: $\sigma_{O-C} = 0^m.01-0^m.03$. Therefore, the linear limb-darkening coefficients for the components (u_1 and u_2) cannot be determined from observations, and they were fixed at their theoretical values (Grygar *et al.* 1972). Our special studies show that the light-curve solution for this binary does not require invoking a third light (L_3). Therefore, we set $L_3 = 0$, although its presence in the binary up to a $\sim 3\%$ level of the total light cannot be ruled out.

We see from Table 1 that the standard deviation of the observations from the corresponding theoretical curve (σ_{O-C}) is virtually constant for a relatively broad range of fixed eccentricities. An analysis of other light curves for this star also yields a similar result. Combining the results of these solutions, we obtained $e = 0.002-0.050$. The derived uncertainty is great, although this is to be expected for a binary with a low eccentricity. Therefore, for the subsequent analysis, we fixed the orbital eccentricity of the eclipsing binary at $e = 0.0025$ that we found below in Apsidal Motion.

To elucidate the causes of the large differences between the photometric elements derived by different

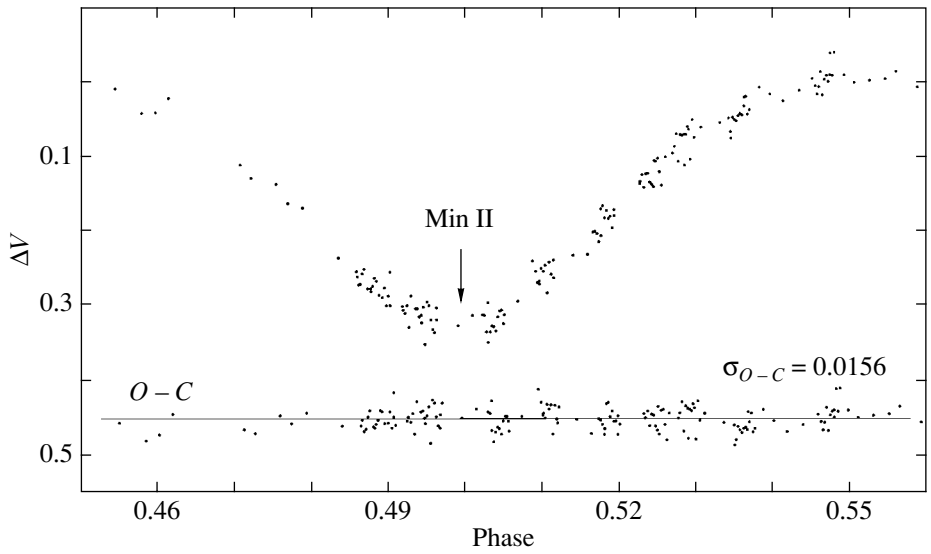

Fig. 2. Same as Fig. 1 near the secondary minimum.

authors, we analyzed all of the available light curves for HP Aur by the same iterative method of differential corrections. Our results are presented in the upper part of Table 2. In addition to our measurements in 2002–2003 and the light curves published by Meinunger (1980) and Kozyreva (1990), we used the unpublished CCD V and R light curves of HP Aur obtained in 1995–1999 and kindly made available to us by Wolf (2000) and Biro (2000).

We see from Table 2 that the difference between the radii found from different light curves reaches 20%, while the (V band) luminosity difference exceeds 30%. At the same time, the sum of the radii of the components, $r_1 + r_2$, is kept within 2% for all of the light curves. This is a characteristic result of the light-curve solution for binaries with partial eclipses where the sum of the radii is determined well, while their ratio $k = r_2/r_1$ is determined badly. The same result for other such binaries was obtained by Khaliullin *et al.* (1985) and Volkov and Khaliullin (2002).

To illustrate this, Table 3 gives the photometric elements of HP Aur that we obtained from the solution of the same light curve as that in Table 1, but for several fixed ratios of the radii of the components k. The data from this table are shown in Fig. 3 as the dependence $\sigma_{O-C}(k)$. We see from Table 3 and Fig. 3 that the admissible range for r_2/r_1 is found to be broad even from the solution of our complete and accurate light curve for HP Aur: from the minimum $k_{\min} \simeq 0.72$ to the maximum $k_{\max} \simeq 1.25$. This, in turn, leads to large uncertainties in the relative radii and luminosities of the components: $r_1 \simeq 0.125$–0.165, $r_2 \simeq 0.120$–0.157, $L_1 \simeq 0.51$–0.75, $L_2 \simeq 0.25$–0.49. Barely noticeable systematic deviations of the observations from the theoretical curve that are *symmetric about the central eclipse phases* and, hence, discernible against the background of random physical light fluctuations in the binary appear only at the boundaries of this range. Note that in the presence of physical light fluctuations in the components of an eclipsing binary, which act as the systematic errors when analyzing the light curves, the standard statistical methods (see, e.g., Goncharskii *et al.* 1985) cannot be used to estimate the confidence intervals of the sought parameters. Therefore, the most feasible and commonly used (but semi-intuitive) criterion for limiting the admissible ranges of parameters is the appearance of symmetric (about the central phases) waves in the $O - C$ diagrams (Popper 1982). We used this criterion above to estimate the range for k.

An analysis of other light curves from Table 2 also yields a similar result for k. Therefore, we may argue that the available light curves for HP Aur do not allow $k = r_2/r_1$ to be determined with the required accuracy (1–2%). This is the reason why the radii and luminosities of the components derived by different authors disagree. Therefore, we had to fix k based on the well-determined masses of the components from the paper by Popper (2000) and under the natural assumption that the binary components have the same age, as implied by the evolutionary models of stars from the papers by Claret and Gimenez (1989, 1992). The method of successive iterations yielded an optimal value of $k = 0.782$. With this fixed value of k, we determined the photometric elements of HP Aur by analyzing the combined light curve constructed from all of the available individual photoelectric V brightness measurements of the binary from the papers cited above and in Table 2; these elements are

Table 1. Photometric elements of HP Aur for several fixed eccentricities determined by analyzing our photoelectric V-band measurements of this star in 2002–2003

Parameter	e									
	0.000	0.003	0.005	0.010	0.020	0.030	0.040	0.050	0.060	0.070
r_1	0.161(3)	0.161	0.160	0.158	0.153	0.150	0.145	0.142	0.140	0.138
r_2	0.128(4)	0.130	0.131	0.134	0.141	0.146	0.152	0.157	0.161	0.164
i	86.°4(3)	86.°3	86.°2	86.°0	85.°6	85.°4	85.°2	85.°1	85.°0	85.°0
ω	–	100°(6)	96°	94°	92°	92°	92°	92°	92°	92°
u_1	0.64(fixed)	〃	〃	〃	〃	〃	〃	〃	〃	〃
u_2	0.70(fixed)	〃	〃	〃	〃	〃	〃	〃	〃	〃
L_1	0.718(18)	0.713	0.707	0.693	0.660	0.629	0.596	0.571	0.549	0.530
L_2	0.282(18)	0.287	0.293	0.307	0.340	0.371	0.404	0.429	0.451	0.470
$r_1 + r_2$	0.289	0.291	0.290	0.292	0.294	0.296	0.297	0.299	0.301	0.302
L_1/L_2	0.393	0.403	0.414	0.443	0.515	0.590	0.678	0.751	0.821	0.887
J_1/J_2	0.619	0.617	0.615	0.613	0.611	0.613	0.616	0.619	0.622	0.624
$k = r_2/r_1$	0.796	0.807	0.820	0.851	0.917	0.980	1.050	1.103	1.150	1.191
σ_{O-C}	$0^m.016$	$0^m.015$	$0^m.015$	$0^m.015$	$0^m.015$	$0^m.015$	$0^m.015$	$0^m.015$	$0^m.016$	$0^m.016$

given in the last column of Table 3 and were taken as the final ones to calculate the absolute parameters.

To check how well the derived r_1 and r_2 satisfy all of the observations, we solved the light curves of different authors for HP Aur at the fixed values of $r_1 = 0.1633$ and $r_2 = 0.1277$ from the last column of Table 3. The results are presented in the last row of Table 2. We see that σ_{O-C} for the upper (r_1 and r_2 are sought independently) and lower (r_1 and r_2 are fixed) parts differ insignificantly. Therefore, we may conclude that our final photometric elements satisfy well all of the observations; the differences in the luminosities of the components and the periastron longitude can be naturally explained in terms of the difference between the spectral bands and the epochs of observations by different authors.

The results of the light-curve solution for HP Aur in the W, B, and R bands for a fixed geometry of the binary are presented in Table 4 together with the data for the V band. The geometrical parameters were fixed at the values from the last column of Table 3, since there is no reason to believe that these parameter can depend on the spectral band. This implies that, in analyzing the multicolor measurements, we varied only the relative luminosities of the components L_1 and L_2, while the linear limb-darkening coefficients (different for different components and spectral bands) were fixed at their theoretical values (Grygar *et al.* 1972). The total magnitudes of the binary HP Aur outside the minima for different spectral bands were taken from Table II in the paper by Kozyreva (1990).

Unfortunately, the $(W-B, B-V)$ two-color diagrams do not allow the interstellar extinction for $G-K$ stars to be determined with a sufficient accuracy, since the interstellar reddening curves in this region of the diagram are almost parallel to the temperature reddening curves. Therefore, we took $A_v = 0^m.40$ for the binary under study based on the mean interstellar extinction of $2^m.0$ kpc^{-1} (Straizys 1977) and the distance to the binary $d = 197$ pc (Table 5) that we determined from the photometric distance modulus: $\log d = (V - M_v + 5 - A_v)/5$. After they were corrected for interstellar extinction with $A_v = 0^m.40$, the color indices $(B-V)$ and $(V-R)$ for the components of HP Aur found by solving the $WBVR$ light curves and presented in Table 4 correspond to the spectral types G2V and G8V for the primary and secondary components, respectively. However, both components exhibit ultraviolet excesses, $\Delta(W-B) \simeq -0^m.25$ and $\Delta(B-V) \simeq -0^m.08$, that are probably attributable to a metal deficiency in the atmospheres of these stars, but this result requires an independent confirmation.

Table 2. Photometric elements of HP Aur determined by analyzing the V and R observations of different authors when independently seeking for r_1 and r_2 (upper part) and at fixed r_1 and r_2 (lower part)

Parameter	Authors				
	Meinunger (1980) (V)	Kozyreva (1990) (V)	Wolf (2000); Biro (2000) (V)	Wolf (2000); Biro (2000) (R)	our data (V)
r_1	0.146(14)	0.137(10)	0.150(5)	0.153(3)	0.161(3)
r_1	0.151(11)	0.157(7)	0.149(4)	0.136(4)	0.129(4)
i	86°.03(24)	85°.03(8)	85°.54(11)	85°.80(20)	86°.3(3)
e	0.0025(fixed)	〃	〃	〃	〃
ω	9°(:)	5°(50)	79°(7)	93°(4)	102°(7)
L_1	0.59(8)	0.55(6)	0.614(25)	0.639(22)	0.715(13)
L_2	0.41(8)	0.45(6)	0.386(25)	0.361(22)	0.285(13)
u_1	0.64(fixed)	0.64	0.64	0.54	0.64
u_2	0.70(fixed)	0.70	0.70	0.59	0.70
$r_1 + r_2$	0.297	0.294	0.299	0.289	0.290
L_2/L_1	0.698	0.821	0.629	0.565	0.399
J_2/J_1	0.649	0.621	0.637	0.714	0.617
$k = r_2/r_1$	1.037	1.151	0.992	0.889	0.803
σ_{O-C}	$0^m.030$	$0^m.014$	$0^m.012$	$0^m.010$	$0^m.016$
r_1	0.1633(fixed)	〃	〃	〃	〃
r_1	0.1277(fixed)	〃	〃	〃	〃
i	87°.35(18)	86°.25(9)	86°.63(5)	86°.42(3)	86°.53(5)
e	0.0025(fixed)	〃	〃	〃	〃
ω	2°(:)	30°(19)	79°(8)	93°(4)	105°(7)
L_1	0.709(4)	0.7225(23)	0.7168(17)	0.6927(8)	0.7239(13)
L_2	0.292(4)	0.2775(23)	0.2832(17)	0.3073(8)	0.2761(13)
u_1	0.64(fixed)	0.64	0.64	0.54	0.64
u_2	0.70(fixed)	0.70	0.70	0.59	0.70
$r_1 + r_2$	0.2910(fixed)	〃	〃	〃	〃
L_2/L_1	0.411	0.384	0.395	0.444	0.381
J_2/J_1	0.671	0.628	0.645	0.726	0.623
$k = r_2/r_1$	0.782	0.782	0.782	0.782	0.782
σ_{O-C}	$0^m.031$	$0^m.015$	$0^m.012$	$0^m.010$	$0^m.016$

The spectral type of the secondary component can also be estimated by a different method. Taking $\mathrm{Sp}_1 =$ G2V and, accordingly, the effective temperature $T_1 =$ 5790 K (Straizys 1982) for the primary component, we can determine the effective temperature of the secondary component T_2 from the Planck function and the surface brightness ratio of the components J_2/J_1 in different spectral bands (see Table 4). The values of T_2 found in this way are 5220, 5230, 5270, and 5270 K for the W, B, V, and R spectral bands, respectively. Since the spectral energy distribution for stars of this spectral type in the W and B bands is generally distorted noticeably and since the bulk of the energy is radiated in the V and R bands, we

Table 3. Photometric elements of HP Aur for several fixed ratios of the radii of the components (for the same light curve as that in Table 1).

Parameter	k									Final elements
	0.70	0.75	0.80	0.90	1.00	1.10	1.20	1.30	1.40	
r_1	0.1602	0.1646	0.1610	0.1527	0.1448	0.1364	0.1290	0.1220	0.1149	0.1633(13)
r_2	0.1121	0.1235	0.1289	0.1374	0.1448	0.1499	0.1549	0.1586	0.1609	0.1277(15)
i	87.°98	86.°90	86.°36	85.°76	85.°45	85.°33	85.°33	85.°43	85.°64	86.°53(12)
e	0.0025(fixed)	〃	〃	〃	〃	〃	〃	〃	〃	〃
ω	113°	107°(6)	103°	98°	95°	92°	90°	88°	86°	105°(7)
u_1	0.64(fixed)	〃	〃	〃	〃	〃	〃	〃	〃	〃
u_2	0.70(fixed)	〃	〃	〃	〃	〃	〃	〃	〃	〃
L_1	0.7629	0.7388	0.7163	0.6704	0.6230	0.5791	0.5367	0.4986	0.4638	0.721(3)
L_2	0.2371	0.2612	0.2837	0.3296	0.3770	0.4209	0.4633	0.5014	0.5362	0.279(3)
$r_1 + r_2$	0.2723	0.2881	0.2899	0.2903	0.2896	0.2863	0.2839	0.2806	0.2758	0.2910
L_2/L_1	0.311	0.354	0.396	0.492	0.605	0.727	0.863	1.006	1.156	0.387
J_2/J_1	0.634	0.628	0.618	0.609	0.605	0.601	0.599	0.595	0.589	0.633
σ_{O-C}	$0^m.018$	0.016	0.016	0.016	0.016	0.016	0.016	0.017	0.017	0.016

Note: The last column gives the elements that were taken as final.

take $T_2 = 5270$ K and, accordingly, $\mathrm{Sp}_2 = \mathrm{G8}V$ as the final values. The ratio J_2/J_1 depends weakly on the sought geometrical parameters of the eclipsing binary; therefore, our value of T_2 is most reliable, and it is given in Table 5 along with other physical and geometrical parameters of the eclipsing binary HP Aur and its components. The two methods are seen to yield consistent results for the spectral types of the components: $\mathrm{Sp} = \mathrm{G2}V + \mathrm{G8}V$.

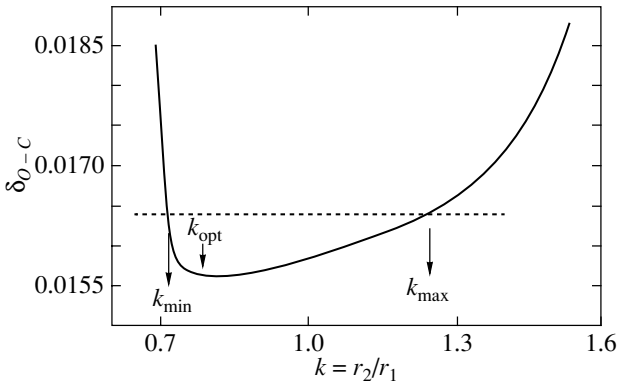

Fig. 3. σ_{O-C} versus fixed ratio of the radii of the components $k = r_2/r_1$; k_{min} and k_{max} are the minimum and maximum possible values of k, respectively, and $k_{\mathrm{opt}} = 0.782$ is the optimal value of k taken as the final one.

Knowing the luminosity ratio of the components, we could also determine their spectral types from the data of Popper (2000). Recall that Popper derived several alternative relations for the spectral types of the components of HP Aur (by analyzing the Na D line equivalent widths): from $(\mathrm{G5}V + \mathrm{G5}V)$ to $(\mathrm{G2}V + \mathrm{K0}V)$, depending on L_2/L_1 for the V band. Unfortunately, our value $L_2/L_1 = 0.39$ (see Table 4) lies outside Popper's working range for this parameter 0.5–0.6. Its extreme estimate $\mathrm{Sp} = \mathrm{G2}V + \mathrm{K0}V$ for $L_2/L_1 = 0.5$ is close to our results.

The trigonometric parallax has not been determined for HP Aur because it is relatively faint ($V = 11^m.20$). However, the distance to the binary d that we estimated from the photometric distance modulus seems reliable enough. It should be noted that the bolometric corrections must slightly differ from their means for the spectral type in question (Straizys 1982) that we used to calculate M_v due to the possible metal deficiency. However, according to our estimates, this difference does not exceed $0^m.1$, which is not very significant for the value of d given in Table 5.

We estimated the age of the binary, $t = (9.5 \pm 0.5) \times 10^9$ yr, simultaneously with the ratio of the radii of the components, $k = r_2/r_1 = 0.782$, by comparing the observed absolute radii with the evolutionary models of stars with the corresponding masses from Claret and Gimenez (1989, 1992) by the method of successive approximations from the equality condition for the ages of the binary components.

THE LIGHT-TIME EFFECT AND PARAMETERS OF THE THIRD BODY

To study the apsidal motion and to find a third body in the binary, we collected all of the published photoelectric times of minima of HP Aur in Table 6. If individual brightness measurements of the binary were available (from the papers by Meinunger 1980; Kozyreva 1990; Wolf 2000; Biro 2000; and our 2002–2003 observations), the times of minima corresponding to these observations were determined by solving the light curves at the fixed geometrical parameters (r_1, r_2, and e) from Table 3. These times are marked by an asterisk in Table 6. An analysis of the data in Table 6 yields the following linear ephemerides to predict the primary (Min I) and secondary (Min II) minima:

$$C_1(\text{Min I}) = \text{JD}_\odot 2446353^{\text{d}}\!.23521(14) + 1.42281984(4)E, \quad (1)$$

$$C_1(\text{Min II}) = \text{JD}_\odot 2446353^{\text{d}}\!.9481(4) + 1.42281937(12)E. \quad (2)$$

We see that the repetition periods of the primary, (P_{I}), and secondary, (P_{II}), minima differ:

$$\Delta P = P_{\text{I}} - P_{\text{II}} = 0^{\text{s}}\!.00000047(13) = 0^{\text{s}}\!.041 \pm 0^{\text{s}}\!.011.$$

This is a clear result of the orbital eccentricity and apsidal motion. We consider this problem in the next section. Note that ephemerides (1) and (2) are not the result of representing the times of the corresponding minima by a simple linear regression. They were obtained when seeking for the parameters of apsidal motion and the light-time effect by the method of successive approximations.

Figure 4 shows the residuals of the observed times of minima (O) in Table 6 from the theoretical ones (C_1) calculated using the linear ephemerides (1) and (2) for Min I and Min II, respectively. We see from this figure that these $(O-C)_1$ residuals exhibit a quasi-periodic wave. The $(O-C)_1$ values for the two minima closely correlate with one another, and their behavior with time leaves no doubt that there is a third body in this system. The orbital parameters of the multiple system can be determined from the so-called light equation (Martynov 1948):

$$\Delta(O-C)_1 + A = \frac{z}{c} = \frac{a_3 \sin i_3}{c}(1 - e_3 \cos E)\sin(v + \omega_3), \quad (3)$$

where c is the speed of light; v and E are the true and eccentric anomalies, respectively; a_3 is the semimajor axis; i_3 is the inclination; e_3 is the eccentricity; and ω_3 is the longitude of pericenter for the orbit of the center of mass of the close binary that revolves about the center of mass of the triple system.

Solving the light equation by the iterative method of differential corrections yielded the following orbital parameters for the triple system:

$$P_3 = 13.7 \pm 0.4\,\text{yr}, \quad T_3 = \text{JD}2449210^{\text{d}} \pm 350^{\text{d}},$$
$$e_3 = 0.7 \pm 0.2, \quad \omega_3 = 268^\circ \pm 25^\circ, \quad (4)$$
$$a_3 \sin i_3 = 0.64 \pm 0.15\ \text{AU}.$$

Here, P_3 is the revolution period of the third body, and T_3 is the time of its periastron passage. These

Table 4. Relative luminosities L_1 and L_2, magnitudes m_1 and m_2, surface brightness ratios J_2/J_1, and color indices of the primary (1) and secondary (2) components of HP Aur determined by analyzing its $WBVR$ light curves

Parameter	Band			
	W	B	V	R
L_1	0.781(13)	0.749(7)	0.720(7)	0.701(8)
L_2	0.219(13)	0.251(7)	0.280(7)	0.299(8)
L_2/L_1	0.280	0.335	0.389	0.427
$-2.5\log\frac{L_2}{L_1}$	$1^m\!.380$	$1^m\!.187$	$1^m\!.025$	$0^m\!.925$
m_{1+2}	$11^m\!.76(2)$	$11^m\!.91(2)$	$11^m\!.19(2)$	$10^m\!.62(2)$
m_1	$12^m\!.03(3)$	$12^m\!.22(3)$	$11^m\!.55(3)$	$11^m\!.01(3)$
m_2	$13^m\!.41(6)$	$13^m\!.41(4)$	$12^m\!.57(4)$	$11^m\!.93(4)$
J_2/J_1	0.458	0.547	0.636	0.698
Component	Color index			
	$W-B$	$B-V$	$B-R$	$V-R$
Primary	$-0^m\!.20(3)$	$0^m\!.68(3)$	$1^m\!.22(3)$	$0^m\!.54(3)$
Secondary	$-0^m\!.00(7)$	$0^m\!.84(4)$	$1^m\!.48(4)$	$0^m\!.64(4)$

Table 5. Basic physical and geometrical parameters of the eclipsing binary HP Aur and its components

Parameter	Component	
	primary	secondary
Mass M, $M_\odot$	0.958 ± 0.011	0.807 ± 0.010
Radius R, $R_\odot$	1.050 ± 0.012	0.821 ± 0.009
Luminosity L, $\log(L/L_\odot)$	0.042 ± 0.030	-0.335 ± 0.032
Effective temperature T_e, K	5790 ± 80	5270 ± 90
Spectral type Sp	G2V	G8V
Surface gravity $\log g$	4.375 ± 0.009	4.514 ± 0.011
Bolometric absolute magnitude M_{bol}	$4^m.61 \pm 0^m.08$	$5^m.56 \pm 0^m.08$
Visual absolute magnitude M_v	$4^m.68 \pm 0^m.09$	$5^m.70 \pm 0^m.09$
Relative radius r, a	0.1633 ± 0.0013	0.1277 ± 0.0015
V	$11^m.55 \pm 0^m.03$	$12^m.57 \pm 0^m.04$
$W-B$	$-0^m.20 \pm 0^m.04$	$0^m.00 \pm 0^m.07$
$B-V$	$0^m.68 \pm 0^m.03$	$0^m.84 \pm 0^m.04$
$V-R$	$0^m.54 \pm 0^m.03$	$0^m.64 \pm 0^m.04$
Orbital period P_a, days	1.42281960(6)	
Semimajor axis of relative orbit a, $R_\odot$	6.430 ± 0.024	
Orbital inclination to plane of sky i	$86^\circ.53 \pm 0^\circ.12$	
Theoretically expected apsidal period U_{th}, yr	92 ± 4	
Binary age t, yr	$(9.5 \pm 0.5) \times 10^9$	
Distance to binary d, pc	197 ± 8	
Photometric parallax π_{ph}	$0''.0051 \pm 0''.0002$	

$(O-C)_1$ residuals in Fig. 5 are folded with the period of the third body P_3; the time of periastron passage by the third body corresponds to a zero phase. The derived parameters allow the mass function of the triple system to be calculated:

$$f(M) = \frac{M_3^3 \sin^3 i_3}{(M_1+M_2+M_3)^2} = \frac{a_3^3 \sin^3 i_3}{P_3^2} = 0.0014 M_\odot. \quad (5)$$

Here, the masses are in solar masses, a_3 is in AU, and P_3 is in years. Substituting M_1 and M_2 from Table 5 yields

$$M_3 \sin i_3 = (0.17 \pm 0.04) M_\odot.$$

We can also estimate the semimajor axis of the orbit of the third body relative to the center of mass of the entire system:

$$A_3 \sin i_3 = a_3 \sin i_3 \frac{M_1+M_2}{M_3} = (6.7 \pm 1.5)\ \text{AU}.$$

The solid lines in Figs. 4 and 5 represent the theoretical curves for the light equation calculated with the parameters found above.

APSIDAL MOTION

In Fig. 6, $(O-C)_2$ is plotted against JD, the Julian date of observations. Here, $(O-C)_2$ are the residuals of the observed (O) times of minima for HP Aur in Table 6 from the times (C_2) calculated with the ephemerides

$$C_2(\text{Min I}) = \text{J D}_\odot 2451004^d.43325 + 1.42281960 + z/c, \quad (6)$$

$$C_2(\text{Min II}) = \text{J D}_\odot 2451004^d.43325 + P/2 + 1.42281960 + z/c, \quad (7)$$

where z/c is the light equation defined by relation (3) and parameters (4) found above. The linear parts of

Table 6. Observed heliocentric times of the primary (I) and secondary (II) minima for HP Aur

$JD_\odot 2400000+$	$(O-C)_2$	Min	Authors	$JD_\odot 2400000+$	$(O-C)_2$	Min	Authors
$42756^d.3471^*$	$0^d.00001$	I	Meinunger (1980)	42805.4391*	$0^d.00263$	II	Meinunger (1980)
43577.3113	0.00005	I	Meinunger (1980)	42842.4280*	−0.00169	II	Meinunger (1980)
43850.4903*	−0.00075	I	Meinunger (1980)	43014.5908*	0.00039	II	Meinunger (1980)
46008.9135	0.00001	I	Liu *et al.* (1989)	43498.3465	−0.00080	II	Meinunger (1980)
46018.8732	−0.00003	I	Liu *et al.* (1989)	43848.3592*	0.00020	II	Meinunger (1980)
46041.6383	−0.00008	I	Liu *et al.* (1989)	46013.8954	0.00026	II	Liu *et al.* (1989)
46045.9068	−0.00004	I	Liu *et al.* (1989)	46070.8100	0.00201	II	Liu *et al.* (1989)
46068.6719	−0.00009	I	Liu *et al.* (1989)	46355.3695*	−0.00266	II	Kozyreva (1990)
46353.2368*	0.00055	I	Kozyreva (1990)	50010.5913	−0.00060	II	Wolf and Sarounova (1996)
50008.4580	0.00074	I	Wolf and Sarounova (1996)	50013.4373*	−0.00025	II	Wolf (2000)
50099.5178*	−0.00031	I	Wolf (2000)	51080.5599**	−0.00600	II	Wolf (2000)
51196.5148*	−0.00008	I	Biro (2000)	51124.6625*	0.00014	II	Biro (2000)
51425.5903	0.00122	I	Agerer and Hubscher (2001)	51935.6673	−0.00237	II	Nelson (2002)
52263.6290	−0.00080	I	Lacy (2002)	52252.9581	−0.00005	II	Lacy (2002)
52267.8979	−0.00035	I	Lacy (2002)	52302.7587	0.00192	II	Lacy (2002)
52270.7433	−0.00059	I	Lacy (2002)	52332.6364	0.00045	II	Lacy (2002)
52287.8168	−0.00091	I	Lacy (2002)	52615.7779	0.00133	II	Lacy (2002)
52317.6964	−0.00049	I	Lacy (2002)	52570.2448*	−0.00162	II	This paper
52563.8448	0.00041	I	Lacy (2002)	52729.6033	0.00141	II	Lacy (2003)
52606.5288	−0.00010	I	Borkovits *et al.* (2003)	52935.9109	0.00070	II	Lacy (2003)
52607.9520	0.00028	I	Lacy (2002)	53001.3589*	−0.00081	II	This paper
52630.7169	0.00010	I	Lacy (2003)	52570.2448	−0.00162	II	Lacy (2003)
52666.2878*	0.00057	I	This paper				
52992.1123*	0.00008	I	This paper				
σ_{O-C}	0.00050			σ_{O-C}	0.00144		

Note: Here, $(O-C)_2$ are the residuals of the observations from the ephemerides corrected for the light-time effect and apsidal motion in the binary.

* The minima that we redetermined by analyzing the individual measurements of different authors.
** The minimum that we did not use in our data analysis. It may contain artificially introduced systematic error.

these ephemerides are specified by the common period P for both minima and the initial epochs for Min I and Min II, which differ by the constant $P/2$. For a circular orbit, we would see random deviations of the observations near $(O-C)_2 = 0$ for both minima in Fig. 6. However, despite the comparatively large scatter of points, the figure clearly shows systematic variations of $(O-C)_2$ with time. These variations for Min I and Min II are out of phase, which is typical of the apsidal motion of an elliptical orbit. As is well known (Martynov 1971), the times of minima in this case must be defined by the relations

$$\text{Min I} = \text{JD}_{\pi/2} + PE + \pi_1(\omega), \tag{8}$$

$$\text{Min II} = \text{JD}_{\pi/2} + P/2 + PE + \pi_2(\omega), \tag{9}$$

where the ω-dependent periodic terms are given by

$$\pi_{1,2} = \mp 2\frac{P}{2\pi}e\cos\omega + \frac{P}{2\pi}e^2\frac{1+2\sqrt{1-e^2}}{(1+\sqrt{1-e^2})^2}\sin 2\omega \pm \frac{2}{3}\,\frac{P}{2\pi}e^3\frac{1+3\sqrt{1-e^2}}{(1+\sqrt{1-e^2})^3}\cos 3\omega. \tag{10}$$

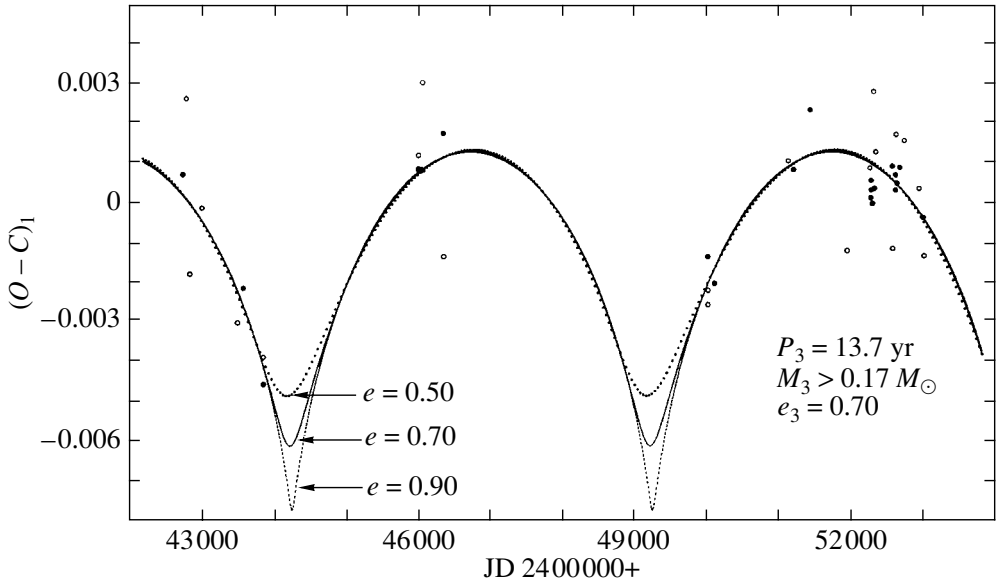

Fig. 4. $(O-C)_1$ versus JD: $(O-C)_1$ are the residuals of the observed times of the primary (filled circles) and secondary (open circles) minima for HP Aur from the linear ephemerides (1) and (2), respectively. The solid line represents the theoretical curve of the light equation constructed with the derived parameters of the triple system.

Here, $\omega = \pi/2 + \dot{\omega}E$, and $\mathrm{JD}_{\pi/2}$ is the initial time of Min I that corresponds to the epoch when $\omega = \pi/2$ (Khaliullin 1997).

Representing the observed times of minima for HP Aur from Table 6 corrected for the light-time effect z/c by relations (8) and (9), we obtained $\mathrm{JD}_{\pi/2} = 2\,451\,004\overset{\mathrm{d}}{.}43325$ and $P = 1\overset{\mathrm{d}}{.}42281960$, which were used above in ephemerides (6) and (7) to construct Fig. 6. However, our attempts to determine the parameters of apsidal motion using this representation show that only a lower limit can at present be set for the observed apsidal period due to the low eccentricity and the relatively short interval of photoelectric observations of this star (≈28 yr):

$$U_{\mathrm{obs}} > 80\ \mathrm{yr},$$

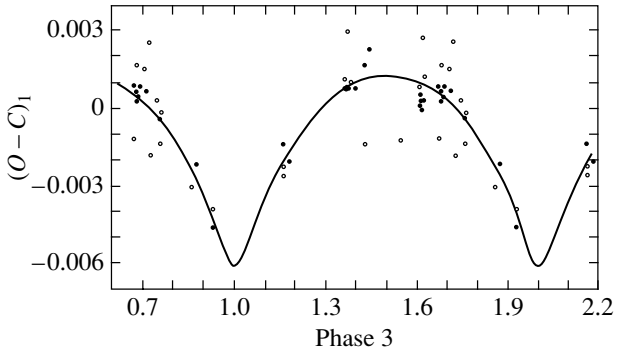

Fig. 5. $(O-C)_1$ versus orbital phase of the third body. The notation is the same as that in Fig. 4.

at the theoretically expected value $U_{\mathrm{th}} \simeq 92$ yr. At $U > 80$ yr, the theoretical curves defined by relations (8) and (9) actually represent the observed time of minima with the same accuracy. The sought values of $\mathrm{JD}_{\pi/2}$ and P are virtually independent of the adopted U, and only the orbital eccentricity changes. If we fix U at the theoretically expected value ($U_{\mathrm{th}} = 92$ yr), then the orbital eccentricity of the eclipsing binary can be determined reliably:

$$e = 0.0025 \pm 0.0005.$$

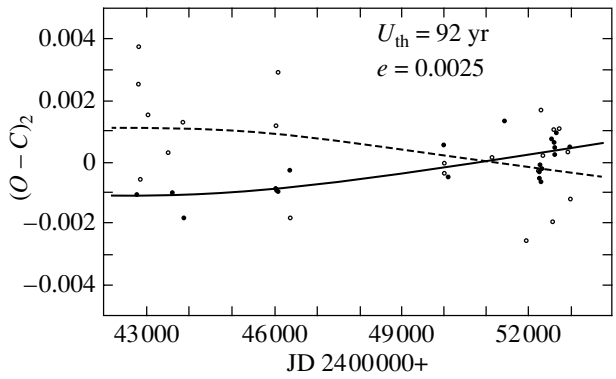

Fig. 6. $(O-C)_2$ versus JD: $(O-C)_2$ are the residuals of the observed times of the primary (filled circles) and secondary (open circles) minima for HP Aur corrected for the light-time effect from the linear ephemerides (6) and (7), respectively. The solid and dashed lines represent the theoretically expected curves for $U = 92$ yr and $e = 0.0025$ for the primary and secondary minima, respectively.

We took and fixed this eccentricity to determine the photometric elements (see above). As far as we know, this is the lowest eccentricity found when analyzing the light curves of eclipsing binaries. The theoretically expected curves (8) and (9) for $U_{\rm th}$ =92 yr and $e = 0.0025$ in Fig. 6 are indicated by the solid and dashed lines for Min I and Min II, respectively. As we see, they satisfactorily describe the observations. However, at least another 20–30 years of photoelectric observations are required to reliably determine the apsidal period for the orbit of this binary.

Table 6 lists the $(O-C)$ values, the residuals of the observations from the ephemerides corrected for the light-time effect and apsidal motion in the binary with the parameters found here:

$$\text{Min I} = \text{JD}_{\pi/2} + PE + \pi_1(\omega) + z/c, \qquad (11)$$

$$\text{Min II} = \text{JD}_{\pi/2} + P/2 + PE + \pi_2(\omega) + z/c. \quad (12)$$

As we see from the table, the standard $(O-C)$ value for the primary minimum ($\sigma_{O-C}(\text{Min I}) = 0\overset{\text{d}}{.}00050$) is almost a factor of 3 smaller than that for the secondary minimum: ($\sigma_{O-C}(\text{Min II}) = 0\overset{\text{d}}{.}00144$). This is probably because the brightness distribution over the disk of the secondary component (G8V) is more nonuniform and unstable. This, in turn, may be attributable to strong magnetic fields and spots on the disk of the secondary star.

CONCLUSIONS

Popper (2000), who constructed reliable radial-velocity curves for both components of HP Aur, expressed a highly pessimistic opinion about the possibility of determining acceptable photometric elements for this binary in the future. This pessimism stemmed mainly from the physical light fluctuations in the star under study. Nevertheless, our photoelectric measurements of this star in 2002–2003 and the highly accurate CCD photometry performed by Wolf (2000) and Biro (2000) in 1995–1999 allowed us to determine the radii (r_1 and r_2) and luminosities (L_1 and L_2) of the components in the multicolor $WBVR$ photometric system for reasonable constraints imposed on the elements (fixed $k = r_2/r_1$ in accordance with the evolutionary models of stars and fixed eccentricity e) with an accuracy of ~1%. This, in turn, made it possible to estimate the spectral types of the components (G2V+ G8V) and other physical and geometrical parameters of this binary given in Table 5. In particular, we detected an ultraviolet excess in the spectra of both components ($\Delta(W-B) \approx -0\overset{\text{m}}{.}25$) that is probably attributable to a metal deficiency in the atmospheres of these stars.

A careful analysis of the times of minima for this star, both the published ones and those that we determined by the iterative method of differential corrections from an analysis of the individual brightness measurements for the star, revealed a light-time effect (previously suspected by Wolf and Sarounova (1996)) and allowed us to determine its parameters ($P_3 =$ 13.7 yr, $e_3 = 0.7$, $A_3 \sin i_3 = 6.7$ AU) and to estimate the mass of the third body: $M_3 \sin^3 i_3 = (0.17 \pm 0.4) M_\odot$. The presence of a third body with such a low mass and a large semimajor axis close to the orbital radius of Jupiter in the eclipsing binary of two solar-type (G2V +G8V) stars is quite remarkable.

Wolf and Sarounova (1996) and Popper (2000) cast doubt on the orbital eccentricity of HP Aur. However, correcting the observed times of minima for the light-time effect removed these doubts: the orbit is eccentric, $e > 0.002$. Apsidal motion is observed: the difference between the repetition periods of Min I and Min II ($\Delta P = 0\overset{\text{s}}{.}047(13)$) is almost a factor of 4 larger than the error in this parameter. Unfortunately, the rate of apsidal motion cannot yet be determined due to the low eccentricity. Only a lower limit can be estimated for the apsidal period: $U_{\rm obs} > 80$ yr. Recall that the theoretically expected period is $U_{\rm th} = 92$ yr. The times of minima for this star must be determined every two or three years to estimate $U_{\rm obs}$.

ACKNOWLEDGMENTS

We wish to thank M. Wolf and B. Biro who kindly provided the light curves of HP Aur. This work was supported by the Federal Science and Technology Astronomy Program.

REFERENCES

1. F. Agerer and J. Hubscher, Inf. Bull. Var. Stars, No. 5016 (2001).
2. I. B. Biro, Private communication (2000).
3. T. Borkovits, I. B. Biro, T. Hegedus, *et al.*, Inf. Bull. Var. Stars, No. 5434 (2003).
4. R. A. Botsula, Perem. Zvezdy **22**, 572 (1987).
5. A. Claret and A. Gimenez, Astron. Astrophys., Suppl. Ser. **81**, 1 (1989).
6. A. Claret and A. Gimenez, Astron. Astrophys., Suppl. Ser. **96**, 255 (1992).
7. G. Giuricin, F. Mardirossian, and M. Mezzetti, Acta Astron. **33**, 159 (1983).
8. A. V. Goncharskiĭ, A. M. Cherepashchuk, and A. G. Yagola, *Ill-Posed Problems of Astrophysics* (Nauka, Moscow, 1985).
9. J. Grygar, M. L. Cooper, and I. Jurkevich, Bull. Astron. Inst. Czech. **23**, 147 (1972).
10. Kh. F. Khaliullin, *Binary Stars*, Ed. by A. V. Masevich (Kosmosinform, Moscow, 1997).
11. Kh. F. Khaliullin, A. V. Mironov, and V. G. Moshkalev, Astrophys. Space Sci. **111**, 291 (1985).

12. A. I. Khaliullina and Kh. F. Khaliullin, Astron. Zh. **61**, 393 (1984) [Sov. Astron. **28**, 228 (1984)].
13. A. I. Khaliullina, Kh. F. Khaliullin, and D. Ya. Martynov, Mon. Not. R. Astron. Soc. **216**, 902 (1985).
14. V. G. Kornilov, I. M. Volkov, and A. I. Zakharov, Tr. Gos. Astron. Inst. im. Shternberga **63** (1991).
15. V. S. Kozyreva, Astrophys. Space Sci. **165**, 1 (1990).
16. C. H. Lacy, Inf. Bull. Var. Stars, No. 5357 (2002).
17. C. H. Lacy, Inf. Bull. Var. Stars, No. 5487 (2003).
18. X. Liu, Z. Cai, and H. Tan, Astrophys. Space Sci. **154**, 1 (1989).
19. A. D. Mallama, P. A. Skillman, P. A. Pinto, and B. A. Krobusek, Inf. Bull. Var. Stars, No. 1249 (1977).
20. D. Ya. Martynov, Izv. Astron. Obs. É. **25**, 5 (1948).
21. D. Ya. Martynov, *Eclipsing Variable Stars*, Ed. by V. P. Tsecevich (Nauka, Moscow, 1971), p. 325.
22. L. Meinunger, Mitt. Veranderliche Sterne **8**, 121 (1980).
23. V. G. Moshkalev and Kh. F. Khaliullin, Astron. Zh. **62**, 393 (1985) [Sov. Astron. **29**, 227 (1985)].
24. R. H. Nelson, Inf. Bull. Var. Stars, No. 5224 (2002).
25. N. V. Perova, Perem. Zvezdy **12**, 371 (1960).
26. D. M. Popper, Annu. Rev. Astron. Astrophys. **18**, 115 (1980).
27. D. M. Popper, Astrophys. J. **254**, 203 (1982).
28. D. M. Popper, Astron. J. **119**, 2391 (2000).
29. E. Splittgerber, Inf. Bull. Var. Stars, No. 572 (1971).
30. V. Straizys, *Multicolor Stellar Photometry* (Mokslas, Vilnius, 1977).
31. V. Straizys, *Metal-Deficient Stars* (Mokslas, Vilnius, 1982).
32. W. Strohmeier, Kleine Veroffentlichungen, Bamberg, Band II, No. 21, 1 (1958).
33. I. M. Volkov and Kh. F. Khaliullin, Astron. Zh. **79**, 827 (2002) [Astron. Rep. **46**, 747 (2002)].
34. M. Wolf, Private communication (2000).
35. M. Wolf and L. Sarounova, Inf. Bull. Var. Stars, No. 4292 (1996).

Translated by V. Astakhov

Astronomy Letters, Vol. 31, No. 2, 2005, pp. 129–139. Translated from Pis'ma v Astronomicheskiĭ Zhurnal, Vol. 31, No. 2, 2005, pp. 143–153.

Two-Mirror Schwarzschild Aplanats: Basic Relations

V. Yu. Terebizh*

Sternberg Astronomical Institute, Universitetskiĭ pr. 13, Moscow, 119992 Russia

Received July 22, 2004

Abstract—The theory of aplanatic two-mirror telescopes developed by Karl Schwarzschild in 1905 is shown to lead to a unified description of both prefocal and postfocal systems. The class of surfaces in the ZEMAX optical program has been properly extended to ascertain the image quality in exact Schwarzschild aplanats. A comparison of Schwarzschild aplanats with approximate Ritchey–Chrétien and Gregory–Maksutov aplanatic telescopes reveals a noticeable advantage of the former at the system's fast focal ratio.

Key words: *telescopes, astronomical optics*.

INTRODUCTION

In a series of papers written a century ago, Karl Schwarzschild laid the foundations of the modern aberration theory of optical systems, including telescopes (see Born and Wolf 1999, Ch. 5; Wilson 1996, Section 3.2). The last section in part II of this series (Schwarzschild 1905) is devoted to seeking an aplanatic two-mirror telescope, i.e., a system in which both spherical aberration and coma were *rigorously* corrected near the optical axis. Schwarzschild managed to derive closed analytical formulas that described the shape of the mirror surfaces in such a telescope. Since he was primarily interested in fast systems (the photographic emulsions were then slow), a telescope with a primary mirror of moderate focal ratio $f/2.5$ and a concave secondary mirror that brought the total focal ratio of the telescope to $f/1.0$ (Fig. 5) was considered as an example. Subsequently, Born and Wolf (1999, §4.10.2) gave a general formulation of the problem of the simultaneous correction of spherical aberration and coma in an arbitrary optical system. Grazing-incidence Schwarzschild telescopes designed for X-ray observations were considered by Popov (1980, 1988)[1].

It is quite possible that the context in which Schwarzschild discussed the problem and the example mentioned above have spawned the widely held view that Schwarzschild's theory is applicable only to prefocal reducing systems (see the next section for an explanation of the terms). Meanwhile, this theory covers not only all prefocal systems, including Cassegrain telescopes, but also postfocal Gregorian systems. Moreover, Schwarzschild's formulas that define the mirror surfaces in an aplanatic telescope can be brought to a form that is valid for an arbitrary two-mirror system.

Since the analytical description of the shape of the mirror surfaces in exact aplanats is rather complex in form, the image quality provided by these telescopes has not been cleared up until now. Only the approximations of the surfaces by conic sections admissible for systems with slow focal ratios were considered. The expansions that emerge in this case were found by Schwarzschild (1905) himself. Subsequently, Chrétien (1922) and Maksutov (1932) concretized these expansions for Cassegrain and Gregorian systems, respectively, which gave rise to telescopes aplanatic in the third order of the aberration theory. Most major modern instruments belong to this class. The advantages of these systems and the discovery of a fast wide-field camera by Schmidt (1930) were responsible for the prolonged lack of interest in Schwarzschild's exact theory.

This situation was understandable as long as the diameter of Schmidt telescopes corresponded to the needs and technology capabilities of the time. At present, one can point out several problems of observational astronomy in connection with which it would be interesting to return to Schwarzschild's theory and ascertain the image quality achievable with *exact* aplanats. Thus, for example, it is important to carry

*E-mail: terebizh@crao.crimea.ua

[1] After the completion of this paper, we learned about the papers by Lynden-Bell (2002) and Willstrop and Lynden-Bell (2003) devoted to two-mirror aplanats. Having only part X of the fundamental study by Schwarzschild (1905) at their disposal, these authors repeated some of the results contained in a different form in the section "First-Order Characteristics" of this study.

1063-7737/05/3102-0129$26.00

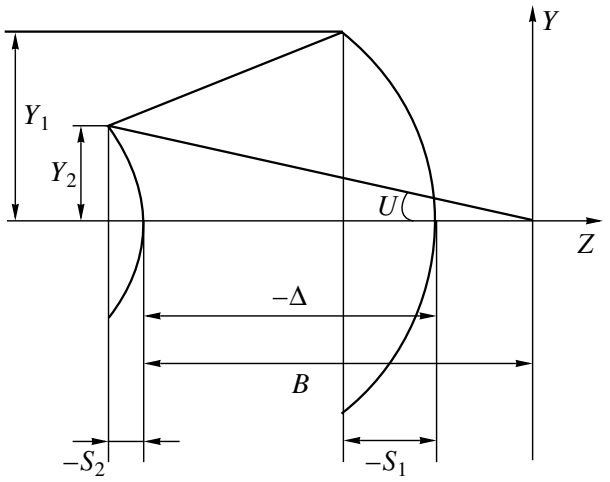

Fig. 1. Basic notation for a Cassegrain system as an example.

out deep sky surveys using telescopes with an effective aperture of 4–7 m and a 2°–3° field of view. This will allow us to study the evolutionary cosmological models and to follow the changes in the positions and brightness of faint objects on a time scale of the order of a day within the entire celestial sphere. An example of another important problem involves far-ultraviolet and X-ray observations from spaceborne platforms, implying the use of telescopes with a minimum number of reflective surfaces. As regards the technological capabilities in producing complex aspherical surfaces with a diameter of the order of several meters, an accuracy that ensures the diffraction-limited image quality has been achieved in recent years.

In this paper, we represent Schwarzschild's formulas in a form that is valid for arbitrary two-mirror aplanatic systems. We then analyze the image quality in aplanats calculated by extending the class of surfaces in the standard ZEMAX optical program [2]. We show that exact Schwarzschild aplanats with a fast focal ratio provide much better images than Ritchey–Chrétien and Gregory–Maksutov systems, which are aplanatic only in the third order of the aberration theory.

Types of two-mirror telescopes

System	Lengthening	Reducing
Prefocal	Cassegrain	Schwarzschild
$F, q, \beta > 0$	$0 < \beta < 1$	$\beta > 1$
Postfocal	Gregory	
$F, q, \beta < 0$	$0 < \lvert\beta\rvert < 1$	$\lvert\beta\rvert > 1$

FIRST-ORDER CHARACTERISTICS

Depending on whether the secondary mirror precedes or succeeds the focus of the primary mirror, the two-mirror telescopes are divided into two major classes: *prefocal* and *postfocal* systems (Maksutov 1932, 1946; Michelson 1976). The equivalent focal length F is positive and negative for prefocal and postfocal systems, respectively. Each of the major classes includes focal *reducing* and *lengthening* systems; F is smaller and larger in absolute value than the focal length of the primary mirror F_1 (we assume that $F_1 > 0$) for the former and the latter, respectively.

Let Δ be the difference between the axial coordinates of the secondary and primary mirror vertices, B be the back focal length of the system, Y_1 be the height of the ray incident on the primary mirror parallel to the optical axis; Y_2 be the height of this ray on the secondary mirror, S_1 and S_2 be the sags of the primary and secondary mirrors corresponding to this ray, and U be the angle between the ray emergent from the system and its optical axis. The notation used for a Cassegrain system is explained in Fig. 1. We assume that the entrance pupil of the telescope is located on the primary mirror, Δ is always negative, Y_1 and B are positive, the signs of S_1 and S_2 are identical to those of the vertex radii of curvature R_1 and R_2 for the corresponding mirrors, Y_2 and U are positive for a prefocal system and negative for a postfocal system. Since the system is axially symmetric, it will suffice to consider only their meridional section by the (Y, Z) plane to describe the shape of the surfaces.

We choose the following four parameters as the specified characteristics of the system:

(1) The diameter of the primary mirror D;

(2) The equivalent focal length of the telescope F;

(3) The relative value of the back focal length $q \equiv B/F$;

(4) The quantity $\beta \equiv F_1/F$ that is the reciprocal of the magnification on the secondary mirror.

To avoid misunderstandings, the classification of two-mirror telescopes used here is summarized in the table. The parameters q and β can take on any values from $-\infty$ to ∞. For slow telescopes, $|q|$ is approximately equal to the linear central obscuration

[2] ZEMAX Development Corporation, USA.

coefficient by the secondary mirror. We are mainly interested in values of $|q| < 1$; it is in this range that promising telescopes should be sought.

Clearly, the focal ratio of the telescope is $\phi \equiv |F|/D$, and the remaining first-order characteristics of all the systems under consideration may be represented in terms of the original parameters as

$$\Delta = -(1-q)\beta F, \quad R_1 = -2\beta F, \qquad (1)$$
$$R_2 = -\frac{2q\beta}{1-\beta}F.$$

For the following analysis, it is convenient to introduce the special designation

$$\delta \equiv (1-q)\beta, \qquad (2)$$

so $\Delta = -\delta F$.

SCHWARZSCHILD'S FORMULAS

A necessary condition for the absence of coma is the satisfaction of the Abbe sine condition in the system,

$$Y_1/\sin U = F = \text{const} \qquad (3)$$

for all of the ray heights Y_1 and aperture angles U. Schwarzschild managed to rigorously combine the sine condition and the equation for the ray passage in the system. The original calculations apply only to a reducing prefocal system for $\delta \neq 1$, but they are so general in nature that they can also be performed for systems of other types with minor modifications. Since these calculations are very cumbersome, we will not present them here, but only write out the final formulas in a form that is valid for an arbitrary two-mirror system.

The sought relations can be written in parametric form; they relate the ordinates of the light ray Y_1 and Y_2 at the points of its intersection with the mirror surfaces and the mirror sags S_1 and S_2 corresponding to these points to the free parameter

$$t = \sin^2(U/2), \qquad 0 \le t \le t_{\max}. \qquad (4)$$

Equation (3) and the condition $|Y_1| \le D/2$ yield the maximum aperture angle

$$U_{\max} = \arcsin(2\phi)^{-1} \qquad (5)$$

and substituting this value into (4) yields

$$t_{\max} = \frac{1}{2}\left[1 - \sqrt{1-(2\phi)^{-2}}\right]. \qquad (6)$$

Usually, $t_{\max}$ is small; $t_{\max} \simeq 0.067$ even for a fast system with a focal ratio of $\phi = 1$.

Let us also define the index

$$\gamma = (1-\delta)^{-1}, \qquad \delta \neq 1. \qquad (7)$$

The formulas that specify the primary mirror profile can then be written as

$$Y_1/|F| = 2\sqrt{t(1-t)}, \qquad (8')$$

$$S_1/F = \begin{cases} q\left[1-(1-t)^{\gamma}|1-t/\delta|^{2-\gamma}\right] - t(1-t)/\delta, & \delta \neq 1 \\ q\left[1-(1-t)^2 e^{t/(1-t)}\right] - t(1-t), & \delta = 1. \end{cases} \qquad (8'')$$

The analogous relations for the secondary mirror are

$$Y_2/|F| = 2\sqrt{t(1-t)}/\Theta(t), \qquad (9')$$

$$S_2/F = q - (1-2t)/\Theta(t), \qquad (9'')$$

where the auxiliary function

$$\Theta(t) = \begin{cases} t/\delta + q^{-1}(1-t)^{1-\gamma}|1-t/\delta|^{\gamma}, & \delta \neq 1 \\ t + q^{-1}(1-t)\,e^{-t/(1-t)}, & \delta = 1. \end{cases} \qquad (10)$$

Note that the results for $\delta = 1$ can be obtained both by repeating calculations similar to Schwarzschild's original calculations and by passing to the limit $\delta \to 1$. According to (2), $\beta = (1-q)^{-1}$ in the case under consideration, and formulas (1) take the form

$$\Delta = -F, \quad R_1 = -\frac{2}{1-q}F, \quad R_2 = 2F. \qquad (1')$$

Thus, assigning values from the interval $[0, t_{\max}]$ to the free parameter t, we find the profile of the mirror surfaces from formulas (8)–(10) that ensure

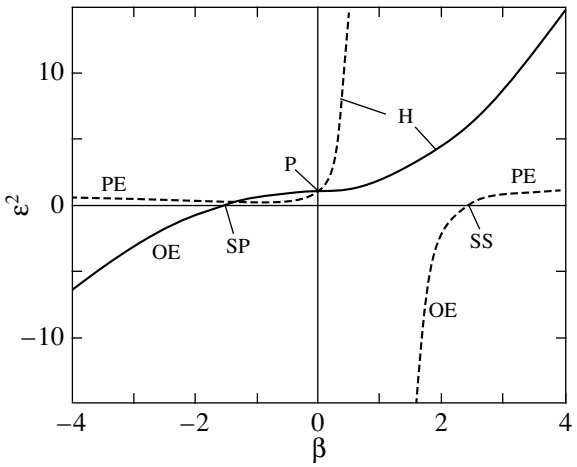

Fig. 2. Squares of the eccentricities of the primary (solid line) and secondary (dashed line) mirrors in approximate aplanats at $|q| = 0.30$ versus β: P—paraboloid, H—hyperboloid, PE—prolate ellipsoid, OE—oblate ellipsoid, SP—spherical primary mirror, SS—spherical secondary mirror.

the absence of spherical aberration and coma in an arbitrary two-mirror telescope.

SLOW SYSTEMS

According to (6), the upper boundary of the free parameter $t_{\max}$ is less than 0.01 even at $\phi = 2.6$ and, at an even slower focal ratio, is

$$t_{\max} \simeq (4\phi)^{-2} \ll 1. \tag{11}$$

For this case, Schwarzschild (1905) expanded the exact formulas in power series of the normalized ray heights $y_1 \equiv Y_1/F$ and $y_2 \equiv Y_2/F$, the first terms of which in our notation are

$$S_1/F = -\frac{1-q}{4\delta}y_1^2 + \frac{q}{32\delta}y_1^4 + q\frac{1+4\delta}{384\delta^2}y_1^6 + q\frac{2+11\delta+30\delta^2}{6144\delta^3}y_1^8 + \ldots, \tag{12}$$

$$S_2/F = -\frac{1-q-\delta}{4q\delta}y_2^2 + \frac{2-\delta-4q+2q^2+2q\delta}{32q^3\delta^2}y_2^4 + \ldots. \tag{13}$$

The expansions are also valid for $\delta = 1$.

The sag of an arbitrary conic section S_c is known to be

$$S_c/F = \frac{y^2}{r}\left[1+\sqrt{1-(1-\epsilon^2)(y/r)^2}\right]^{-1}, \tag{14}$$

where $r = R/F$ is the dimensionless radius of curvature at the vertex, and ϵ is the surface eccentricity. Hence, we can easily obtain the expansion

$$S_c/F = \frac{1}{2r}y^2 + \frac{1-\epsilon^2}{8r^3}y^4 + \frac{(1-\epsilon^2)^2}{16r^5}y^6 + \ldots. \tag{15}$$

Its comparison with (12) and (13) allows the approximation of exact aplanatic surfaces by conicoids for slow systems to be elucidated.

For the primary mirror, the first two expansion terms give the following expressions for the radius of curvature and the square of the eccentricity:

$$r_1 = -\frac{2\delta}{1-q}, \qquad \epsilon_1^2 = 1 + \frac{2q\delta^2}{(1-q)^3}. \tag{16}$$

Given the definition of the constant δ in (2), we see that the former expression is identical to that in (1), while it follows from the latter expression that

$$\epsilon_1^2 = 1 + \frac{2q\beta^2}{1-q}. \tag{17}$$

Just as above, we obtain for the secondary mirror

$$r_2 = -\frac{2q\delta}{1-q-\delta}, \tag{18}$$

$$\epsilon_2^2 = \left(\frac{1-q+\delta}{1-q-\delta}\right)^2 + \frac{2\delta^2}{(1-q-\delta)^3}.$$

The expression for r_2 is identical to that in (1), while the square of the eccentricity of the secondary mirror expressed in terms of the basic variables (q, β) can be written as

$$\epsilon_2^2 = \left(\frac{1+\beta}{1-\beta}\right)^2 + \frac{2\beta^2}{(1-q)(1-\beta)^3}. \tag{19}$$

Equations (17) and (19) form the basis for the theory of systems aplanatic in the third order of the aberration theory (see, e.g., Schroeder 2000, §6.2.b). For clarity, Fig. 2 gives a graphical representation of these expressions that is essentially identical to that in the book by Maksutov (1946, Section 21). An afocal Mersenne system of two paraboloids with coincident foci corresponds to $\beta = 0$. For $0 < \beta < 1$, Eqs. (17) and (19) describe a Ritchey–Chrétien system. The case of $\beta = 1$ corresponds to the so-called ring telescope with a planoid secondary mirror (Maksutov 1932; Churilovskiĭ 1958; Landi Dessy 1968). The domain $\beta > 1$ corresponds to the family of reducing Schwarzschild telescopes aplanatic in the third-order approximation. Over the domain $\beta > 0$, the primary mirror is a hyperboloid, while the secondary mirror is a hyperboloid in a lengthening aplanat and changes its shape for reducing systems from an oblate ellipsoid[3] to a hyperboloid, passing through

[3] This is the region of the ellipsoidal surface around the point of its intersection with the minor axis; previously, an oblate ellipsoid was commonly called an oblate spheroid.

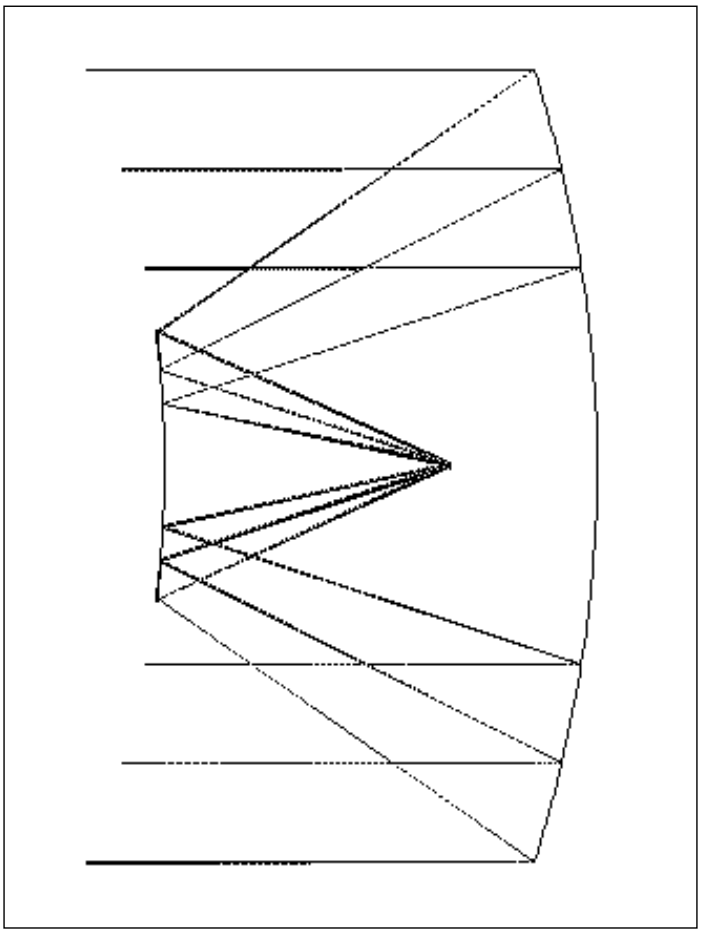

Fig. 3. Optical layout of the SA-01 telescope with a focal ratio of $\phi = 1.2$.

a sphere and a prolate ellipsoid. The domain $\beta < 0$ corresponds to the aplanatic version of the Gregory system. Here, the secondary mirror remains a prolate ellipsoid, while the primary mirror changes its shape from a prolate to an oblate ellipsoid, also passing through a sphere.

We emphasize that Fig. 2 describes slow systems in which only the third-order aberrations were corrected. Therefore, it gives only a rough idea of the family of exact aplanatic surfaces.

SCHWARZSCHILD SURFACES IN THE ZEMAX PROGRAM

Ascertaining the image quality in exact Schwarz schild aplanats requires either developing a special program for calculating the ray path in such systems or extending the class of surfaces in one of the existing optical programs. We chose the second approach, especially since the powerful ZEMAX optical program allows it to be implemented with relative ease. This requires writing additional programs in the C/C++ language, in which the new surfaces (8)–(10) and the optics based on them are described, and then compiling these programs and dynamically linking them with the main program. Thus, we can use the extensive set of tools for studying the properties of optical systems provided by ZEMAX.

In this way, we obtained the files ksp.dll and kss.dll (from Karl Schwarzschild primary/secondary) that define, respectively, the primary and secondary mirrors of an arbitrary aplanat. The quantities (D, F, q, β) defined in the section "First-Order Characteristics" should be specified as additional parameters when calling a surface.

EXAMPLES OF FAST APLANATS

An analysis of several model systems indicates that Ritchey–Chrétien and Gregory–Maksutov systems yield a satisfactory approximation to exact aplanatic systems for ϕ of $\sim$4 or larger. The volume of this publication does not allow us to illustrate the change

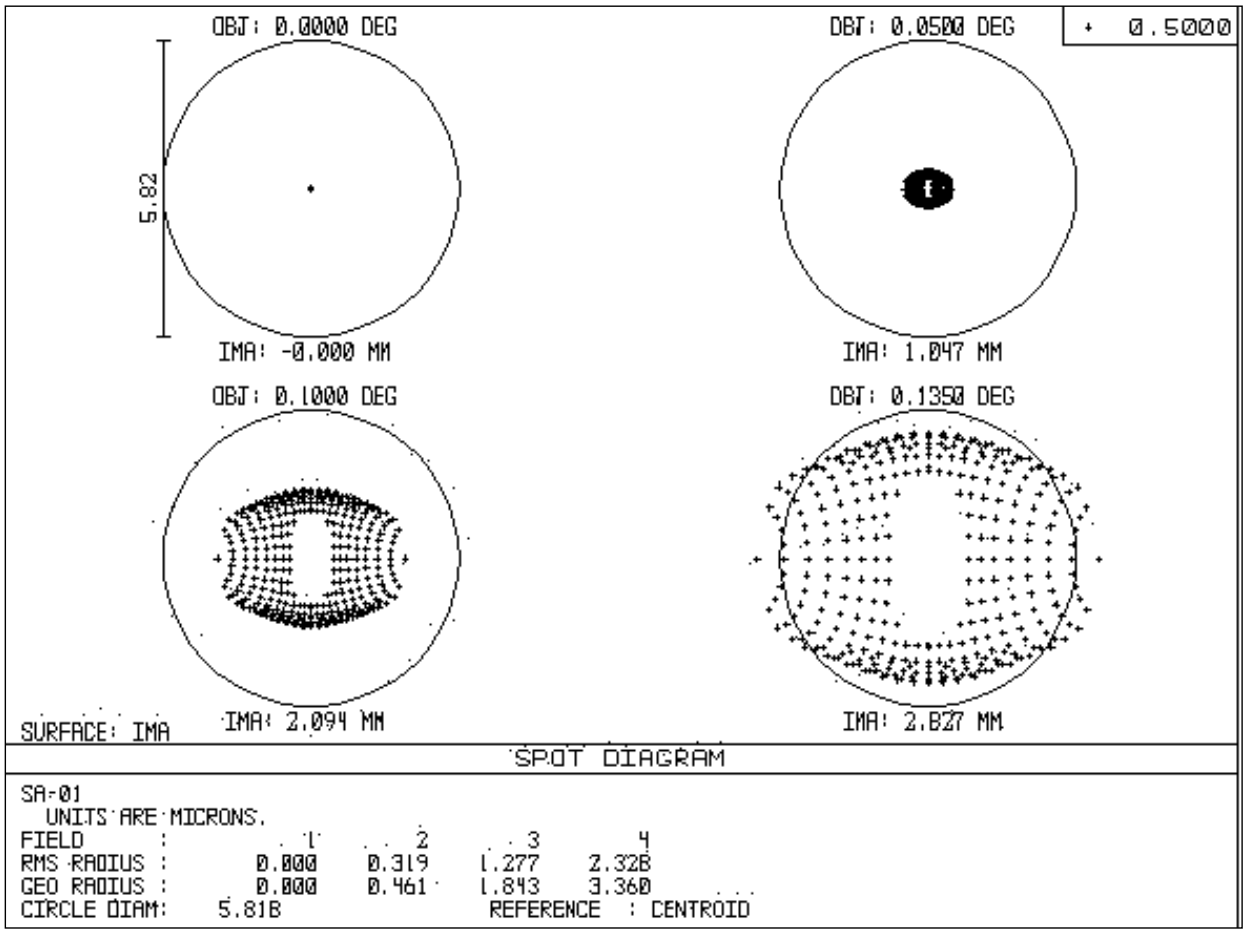

Fig. 4. Spot diagrams for the SA-01 telescope in the field of view $2w = 0°.27$ (the wavelength is 0.5 μm). The root-mean-square (RMS) and geometrical (GEO) image radii as well as the diameter of the circle corresponding to 1″ are given in micrometers.

in image quality as the focal ratio of the system becomes faster; here, we restrict our analysis to several examples. The optical telescope layouts considered below give a general idea of the quality of the images obtained with exact aplanats.

We characterize the image quality by the quantity D_{80}, the diameter of the circle within which 80% of the energy is concentrated in the diffraction image of a point source. Denote the diameter of the field of view, in which D_{80} does not exceed one arcsecond, by $2w_{\rm oas}$.

The astigmatism and the field curvature remain uncorrected in aplanatic systems. In general, these aberrations in mirror telescopes are removed by inserting lens correctors. A preliminary analysis shows that a simple corrector of three lenses with spherical surfaces inserted in a lengthening $f/1.2$ Schwarzschild aplanat provides a flat field of view about 1° in diameter (see the section "Including Schwarzschild Aplanats in Complex Systems"). We are going to systematically study the correctors in Schwarzschild aplanats later.

The Cassegrain System

Figure 3 shows the optical layout of the SA-01 telescope with an aperture diameter of 1 m and a focal ratio of $\phi = 1.2$. We chose $q = 0.30$ and $\beta = 0.65$ for the remaining parameters, so the magnification on the secondary mirror is $m \equiv 1/\beta \simeq 1.54$. The focal ratio for the primary mirror is $\phi_1 = 0.78$, which is achievable at the present state of the art.

The field of view $2w_{\rm oas}$ is $0°.27$ ($16'.2$) in this case; the image quality is illustrated by the spot diagrams[4] in Fig. 4. The Airy circle is 1.5 μm in diameter, so the image quality in the central part of a $10'$ field of view is determined by the diffraction of light. Given the field of view, the central obscuration coefficient is 0.34. The

[4] The spot diagram is the distribution of light rays in the image of a star on the focal surface.

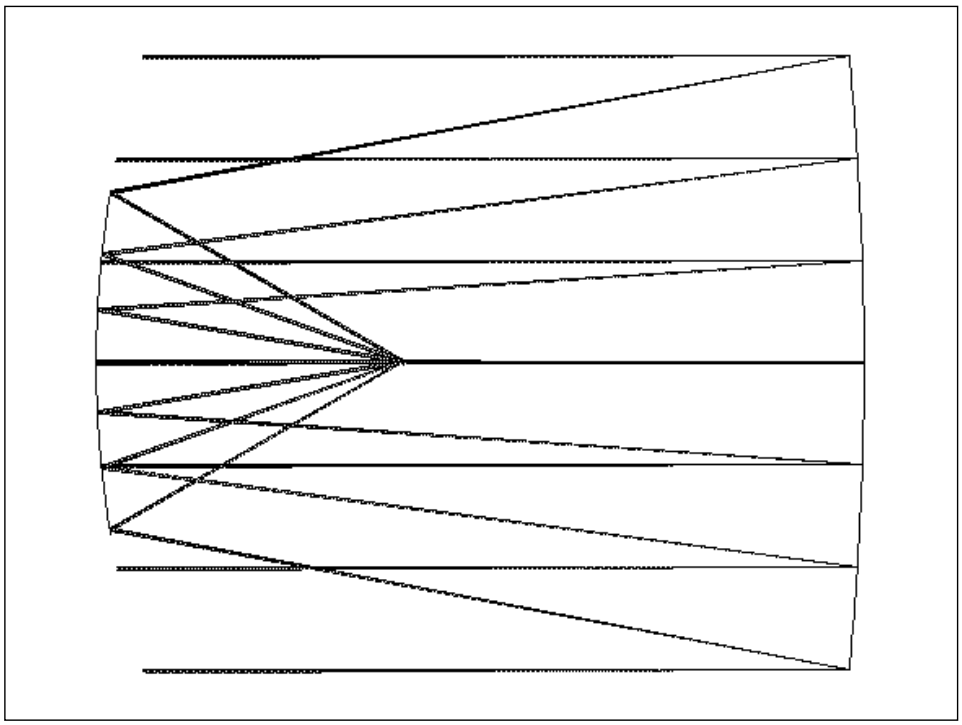

Fig. 5. Optical layout of the SA-02 telescope with a focal ratio of $\phi = 1.0$.

optimum radius of curvature of the focal surface is $R_{\rm im} = -281.4$ mm, so its maximum deviation from the plane in the field of view is 14.2 μm. Since the focal ratio of the system is fast, direct imaging with a flat detector would increase the root-mean-square (rms) image radius at the edge of the field from 2.3 to 5.2 μm. The system is compact: its length, 546 mm, is almost half the aperture diameter.

In the Ritchey–Chrétien system, RC-01, with the same original parameters, the squares of the mirror eccentricities are $\epsilon_1^2 = 1.362143$ and $\epsilon_2^2 = 50.379425$. The rms image diameter of a point source on the optical axis is more than 0.5 mm, so it would be unreasonable to talk about a useful field of view.

For the coincident vertices of the primary mirrors in the exact aplanat, SA-01, and the Ritchey–Chrétien system, RC-01, the difference between their profiles changes monotonically, reaching 88.9 μm at the edge; the sag for SA-01 is smaller in absolute value than that for RC-01. A similar picture is also observed for the secondary mirrors: the largest deviation of the surfaces is 180.6 μm, and the sag for SA-01 is smaller in absolute value than that for RC-01.

The Schwarzschild System

As an example, Schwarzschild (1905) considered a reducing telescope with a diameter of 1 m and a focal ratio of $\phi = 1.0$; recalculating the original parameters to those used here yields $q = 0.50$ and $\beta = 2.50$. The focal ratio for the primary mirror is $\phi_1 = 2.50$. Figures 5 and 6 are similar to Figs. 3 and 4.

In this case, the field of view $2w_{\rm oas}$ is 0°.43. Given the field of view, the central obscuration coefficient is 0.56. The optimum focal surface is close to a plane, $R_{\rm im} = 2758$ mm, so imaging with a flat detector at such a fast focal ratio of the system would increase the rms image radius at the edge of the field from 1.8 to only 2.1 μm. The length of the system is 1250 mm.

The rms image diameter on the optical axis in the Ritchey–Chrétien system with the same initial parameters reaches almost 2 mm (the back focal length and the radius of curvature of the focal surface were optimized).

Including Schwarzschild Aplanats in Complex Systems

It is quite clear that Schwarzschild aplanats are not only of interest in their own right, but can also form the basis for complex optical systems: telescopes, fast objectives, etc. As an example, we restrict ourselves to a three-lens corrector to the SA-01 system considered above. The problem is to make the field of view flat and to increase the diameter of the field of subarcsecond image quality from the initial 0°.27 to about 1°, while retaining the focal ratio of the system at the previous level of $\phi \simeq 1.2$. For simplicity,

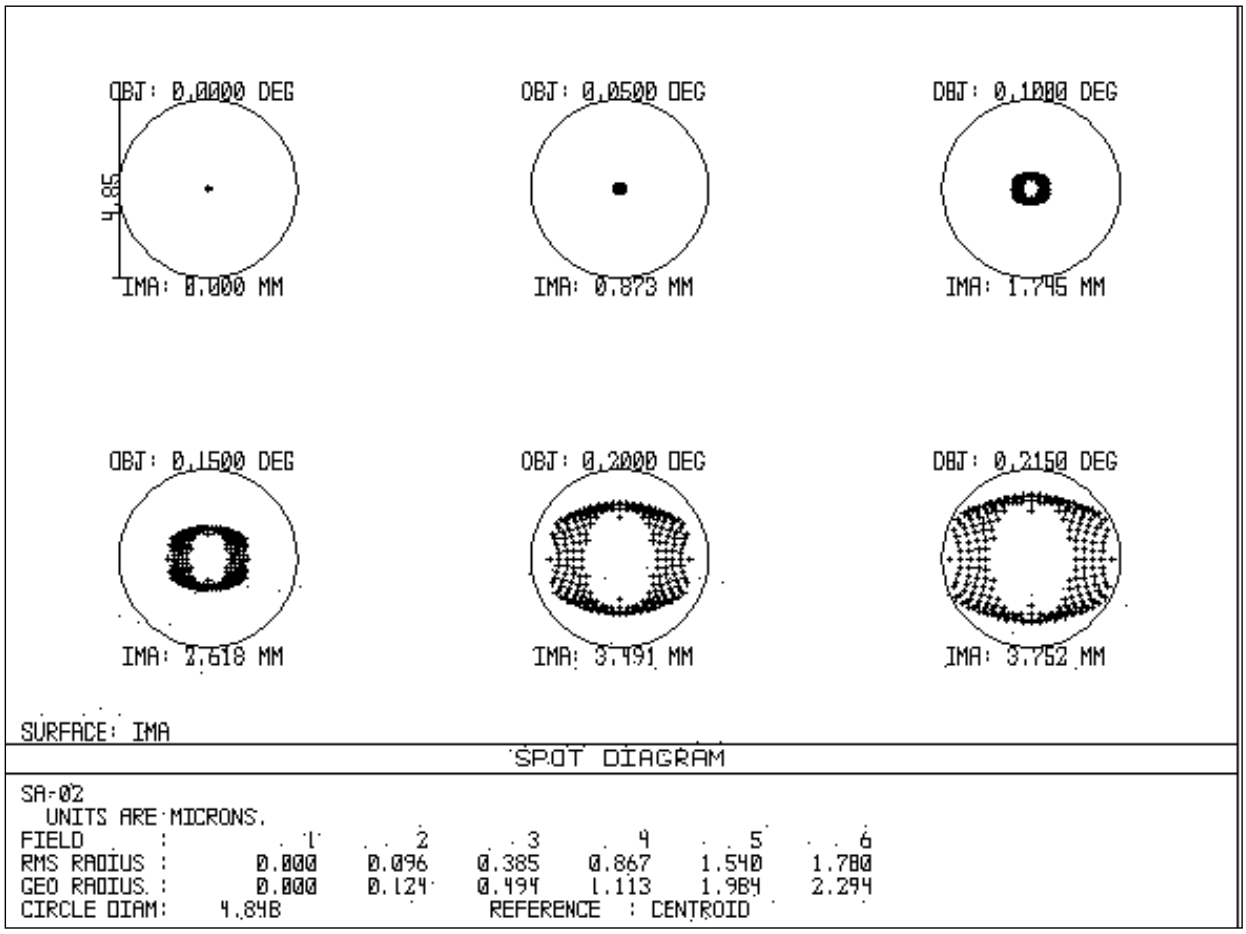

Fig. 6. Spot diagrams for the SA-02 telescope in the field of view $2w = 0°.43$ (the wavelength is 0.5 μm). The root-mean-square (RMS) and geometrical (GEO) image radii as well as the diameter of the circle corresponding to 1″ are given in micrometers.

we assume that all of the lens surfaces are spherical in shape and that the parameters of the two-mirror telescope are fixed.

The optical layout of this corrector is shown in Fig. 7; the corresponding spot diagrams in polychromatic light with wavelengths from 0.40 to 1.0 μm are shown in Fig. 8. The focal ratio of the system is $\phi = 1.169$. The lens diameters are small, they are equal to (in the ray path) 94.7, 44.1, and 40.2 mm; the types of glass are Schott SF15, LAK16A, and SK11, respectively; the back focal length (the gap between the last lens and the detector) is 20 mm. The image diameter of a point source D_{80} at the edge of a 1° field of view is 1″.02. Naturally, the image quality is higher in the narrow spectral bands where observations are commonly performed. A larger field of view can be achieved by simultaneously optimizing the correctors and the two mirrors.

CONCLUDING REMARKS

First of all, it should be noted that a field of ~1° in diameter is insufficient to carry out the sky surveys mentioned in the Introduction. Either a single mirror with a lens corrector at the prime focus (Blanco *et al.* 2002; McPherson *et al.* 2002; Terebizh 2004) or an aplanatic (in the third order) two-mirror system supplemented with a corrector (Angel *et al.* 2000; York *et al.* 2000; Hodapp *et al.* 2003) forms the basis for the currently designed telescopes with a 2°–3° field of view. A lens corrector at the prime focus of a hyperbolic mirror allows a 3° field of view of subarcsecond quality to be achieved by relatively simple means: all lenses are made of glass of the same, virtually arbitrary type, and their surfaces are spherical in shape, but the sizes of the entire system are large. On the other hand, telescopes based on the fast Cassegrain design are quite compact, but the lens or mirror–lens corrector that supplements them is very complex. The choice of a Schwarzschild aplanat as the basic two-mirror system may allow the lens part of wide-

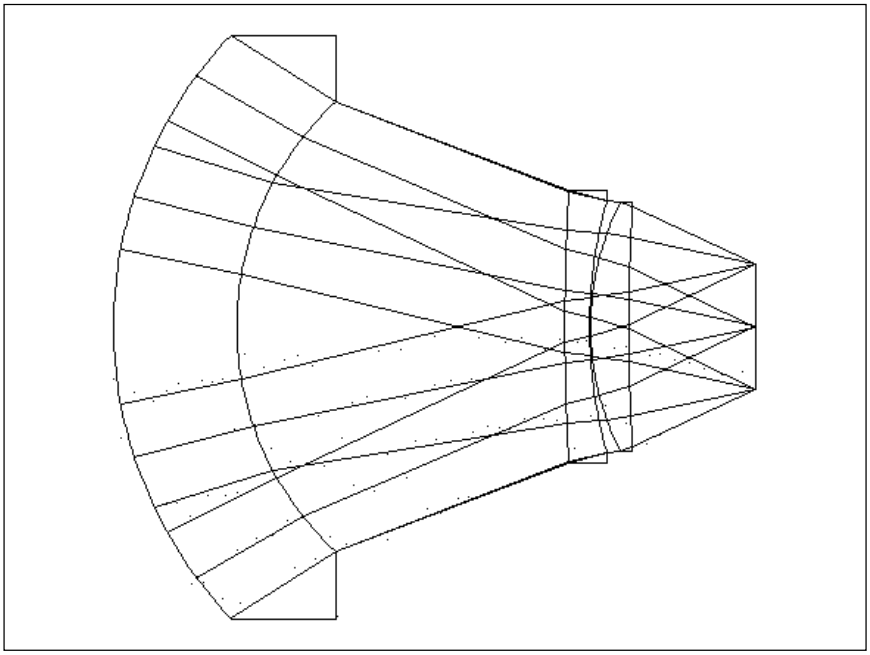

Fig. 7. Three-lens field corrector to the SA-01 telescope.

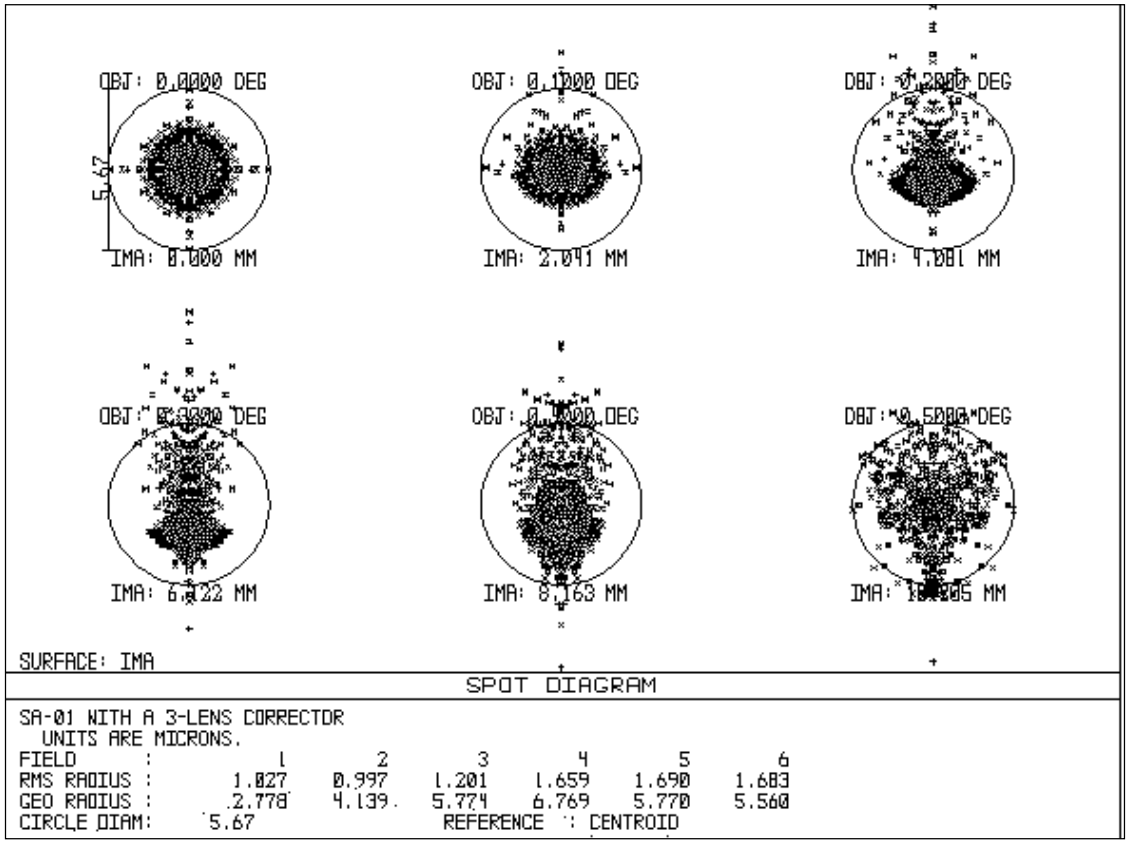

Fig. 8. Spot diagrams for the SA-01 telescope with the corrector shown in Fig. 7. The diameter of the flat field of view is $2w = 1°$; polychromatic light with wavelengths of 0.4–1.0 μm is considered. The root-mean-square (RMS) and geometrical (GEO) image radii as well as the diameter of the circle corresponding to $1''$ are given in micrometers.

field telescopes to be simplified, while preserving their compactness.

In principle, the production of Schwarzschild surfaces poses no specific problems compared to the production of conicoids. Since in both cases the difficulties grow rapidly as the focal ratio becomes faster, particular attention should be paid to the reliability of optics control. Offner's conventional system with two small lenses or mirrors has a number of degrees of freedom that is large enough to achieve focal ratios $\phi \sim 1$ (Offner 1978). The system with a Hartmann screen in the convergent beam proposed by Biryukov and Terebizh (2003) also seems promising; the relative complexity of the data analysis is compensated by the exceptional ease of the experimental facility.

The difficulty of producing the surfaces described by Eqs. (8)–(10) can be roughly estimated if we approximate them by conic sections. The largest deviation of a conicoid from the nearest sphere is known to be

$$\delta S_{\max} = \frac{D\epsilon^2}{4096\phi^3}, \qquad (20)$$

where D, ϵ, and ϕ are, respectively, the diameter, eccentricity, and focal ratio of the surface (see, e.g., Maksutov 1946, Section 20). Thus, for example, the asphericity of the primary mirror in the 1.8-m Vatican Observatory telescope ($\phi = 1.0$, $\epsilon^2 = 1.0$) is very large, 440 μm. Nevertheless, in the early 1990s, this mirror was produced with an accuracy that ensured an rms error of the wavefront[5] equal to only 1/30 of the wavelength $\lambda = 0.5$ μm (Update on Progress at the Steward Obs. 1991).

Dierickx (1999) noted that the *relative slope* of the aspherical surface, rather than the departure from the nearest sphere, is important. It is convenient to use the following dimensionless quantity as a parameter that characterizes the difficulty of producing a surface:

$$\omega = \frac{\epsilon^2}{8\phi^3}, \qquad (21)$$

the reciprocal of the parameter δc introduced by Dierickx. The point is that ω is proportional to the relative slope of the aspherical surface. Thus, a greater production difficulty corresponds to a larger ω, and characteristics (20) and (21) become similar in this sense. For the mirror of the Vatican Observatory mentioned above, $\omega = 1/8$. At present, fast mirrors with $\epsilon^2 \simeq 5$–10 are produced, so we may consider $\omega \sim 1$ to be achievable.

[5]Recall that, according to Maréchal's well-known criterion, an optical system may be considered diffraction-limited if the rms error of the wavefront does not exceed ~1/14 of the wavelength (Born and Wolf 1999, §9.3).

Let us consider the SA-01 system from this point of view. For the primary mirror, $\epsilon_1^2 \simeq 1.36$ and $\phi_1 = 0.78$, which yields $\omega_1 = 0.36$. For the secondary mirror, $\epsilon_2^2 \simeq 50.4$ and $\phi_2 \simeq 2$, which yields $\omega_2 \simeq 0.79$. We see that producing aplanatic surfaces is a major but resolvable problem.

The question of light baffles is particularly acute for fast systems. Recently, exact analytical expressions have been derived for the sizes of optimum baffles in a Cassegrain system with mirrors in the shape of arbitrary conic surfaces (Terebizh 2001). Similar expressions can also be easily derived for postfocal systems. Since Schwarzschild surfaces differ from conicoids, the result mentioned is generally inapplicable to exact aplanats, but the path of rays in them does not change as significantly as do the images, and the analytical expressions can be used to obtain a satisfactory approximation.

With regard to aplanatic (in the third order) systems, Maksutov (1946) wrote: "Aplanatic mirror telescopes have a great future, since only these systems will allow superpowerful and fast instruments with the fields of first-rate photographic images sufficient for practical purposes to be made." This opinion is all the more valid for exact Schwarzschild aplanats.

ACKNOWLEDGMENTS

I am grateful to V.V. Biryukov (Moscow State University) for his helpful discussion of the questions dealt with here.

REFERENCES

1. J. R. P. Angel, M. Lesser, R. Sarlot, *et al.*, ASP Conf. Ser. **195**, 81 (2000).
2. V. V. Biryukov and V. Yu. Terebizh, Izv. Krym. Astrofiz. Obs. **99**, 152 (2003).
3. D. R. Blanco, G. Pentland, C. H. Smith, *et al.*, Proc. SPIE **4842**, 85 (2003).
4. M. Born and E. Wolf, *Principles of Optics*, 7th ed. (Cambridge Univ. Press, Cambridge, 1999).
5. H. Chrétien, Rev. d'Opt. **1** (13), 49 (1922).
6. V. N. Churilovskiĭ, Izv. Vyssh. Uchebn. Zaved., Priborostr. **2**, 102 (1958).
7. P. Dierickx, *Proc. Bäckaskog Workshop on Extremely Large Telescopes* (1999), p. 224.
8. K. W. Hodapp, U. Laux, and W. A. Siegmund, Pan-STARRS Doc. Control PSDC-300-001-00 (2003).
9. J. Landi Dessy, Bol. Assoc. Argent. Astron., No. 14, 21 (1968).
10. D. Lynden-Bell, Mon. Not. R. Astron. Soc. **334**, 787 (2002).
11. D. D. Maksutov, Tr. Gos. Opt. Inst. **8** (86) (1932).
12. D. D. Maksutov, *Astronomical Optics* (Gostekhizdat, Moscow, 1946) [in Russian].
13. A. McPherson, S. C. Craig, and W. Sutherland, Proc. SPIE **4837**, 82 (2003).

14. N. N. Mikhel'son, *Optical Telescopes. Theory and Construction* (Nauka, Moscow, 1976) [in Russian].
15. A. Offner, *Optical Shop Testing*, Ed. by D. Malacara (1978), Chap. 14.
16. G. M. Popov, *Aspherical Surfaces in Astronomical Optics* (Nauka, Moscow, 1980) [in Russian].
17. G. M. Popov, *Modern Astronomical Optics* (Nauka, Moscow, 1988) [in Russian].
18. B. Schmidt, Mitteilungen Hamburger Sternwarte in Bergedorf **7** (36), 15 (1930). Reprinted: *Selected Papers on Astronomical Optics*, SPIE Milestone Ser. **73**, 165 (1993).
19. D. J. Schroeder, *Astronomical Optics* (Academic Press, San Diego, 2000).
20. K. Schwarzschild, Astronomische Mittheilungen der Königlichen Sternwarte zu Göttingen **10**, 3 (1905), Part II. Reprinted: *Selected Papers on Astronomical Optics*, SPIE Milestone Ser. **73**, 3 (1993).
21. V. Yu. Terebizh, Exp. Astron. **11**, 171 (2001).
22. V. Yu. Terebizh, Pis'ma Astron. Zh. **30** (3), 231 (2004) [Astron. Lett. **30** (3), 200 (2004)].
23. *Update on Progress at the Steward Obs. Mirror Lab.* (Dec. 1991).
24. R. V. Willstrop and D. Lynden-Bell, Mon. Not. R. Astron. Soc. **342**, 33 (2003).
25. R. N. Wilson, *Reflecting Telescope Optics* (Springer, Berlin, 1996), Vol. I.
26. D. G. York, J. Adelman, J. E. Anderson, *et al.*, Astron. J. **120**, 1579 (2000).

Translated by V. Astakhov

Astronomy Letters, Vol. 31, No. 2, 2005, pp. 140–146. Translated from Pis'ma v Astronomicheskiĭ Zhurnal, Vol. 31, No. 2, 2005, pp. 154–160.

Orbital Evolution of the Distant Satellites of the Giant Planets

M. A. Vashkov'yak* and N. M. Teslenko**

Keldysh Institute of Applied Mathematics, Russian Academy of Sciences, Miusskaya pl. 4, Moscow, 125047 Russia

Received July 1, 2004

Abstract—We study the evolution of several distant satellite orbits. These are the orbits (including the improved ones) of the recently discovered Neptunian satellites S/2002 N1, N2, N3, N4; S/2003 N1 and the orbits of Jovian, Saturnian, and Uranian satellites with librational variations in the argument of the pericenter: S/2001 J10 (Euporie), S/2003 J20; S/2000 S5 (Kiviuq), S/2000 S6 (Ijiraq), and S/2003 U3. The study is performed using mainly an approximate numerical–analytical method. We determine the extreme eccentricities and inclinations as well as the periods of the variations in the arguments of pericenters and longitudes of the ascending nodes on time intervals $\sim 10^5$–10^6 yr. We compare our results with those obtained by numerically integrating the rigorous equations of satellite motion on time intervals of the order of the circulation periods of the longitudes of the ascending nodes (10^2–10^3 yr).

Key words: *planetary satellites, orbital evolution.*

INTRODUCTION

Distant (or outer) satellites have peculiar orbits with large eccentricities and/or inclinations to the equatorial plane of the central planet and are called irregular satellites. The origin of these satellites and the evolution of their orbits have invariably aroused the interest of researchers, which has increased appreciably in recent years in connection with the recent discoveries of dozens of irregular satellites around the Jovian planets.

Noteworthy among the recent studies on this issue are the works by Cuk and Burns (2004) who suggested a new model for the secular evolution of irregular Saturnian satellites and Burns *et al.* (2004) who analyzed the evolution of orbits close to the ω-librating orbit of the Saturnian satellite Kiviuq. We particularly point out the comprehensive paper by Nesvorny *et al.* (2003) who used mostly numerical methods to analyze the *"orbital and collisional evolution"* of 60 000 fictitious satellites of the giant planets and 50 real distant satellites known by August 2003. In particular, computations on a time interval of 10^8 yr revealed regions of stable orbits of irregular satellites and their individual groups similar to the families of asteroids. In addition, the above paper gives a complete list of works on the evolution of distant satellite orbits. This list can also be supplemented with the bibliographic review on the dynamics of natural planetary satellites by Ural'skaya (2003).

In this paper, we analyze the evolution of distant satellite orbits using an approximate numerical–analytical method (Vashkov'yak 2005). It is based on Zeipel's method and the 1965–1972 series of papers by A.A. Orlov, beginning with the fundamental paper by Orlov (1965). This method includes the solar perturbations and the orbital evolution of the central planet. The short- and intermediate-period perturbations are calculated analytically, while the evolution system in mean elements is integrated numerically. The admissible (for the solution of the evolution problem) integration step for the equations free from the most rapidly osculating functions of time is of the order of several satellite orbital periods.

THE ORBITAL EVOLUTION OF DISTANT NEPTUNIAN SATELLITES

The orbits of the distant Neptunian satellites (except Nereid) discovered in 2002 were improved in the second half of 2003. Improving the orbits of the satellites S/2002 N1 and N3 (Marsden 2003a–2003c) led to an appreciable change in the extreme eccentricities, ecliptic inclinations, and circulation periods of the arguments of pericenters and longitudes of the ascending nodes compared to our data (Vashkov'yak 2003). As regards the satellite S/2002 N2 (Marsden 2003d), the evolution of its

*E-mail: vashkov@keldysh.ru
**E-mail: teslen@keldysh.ru

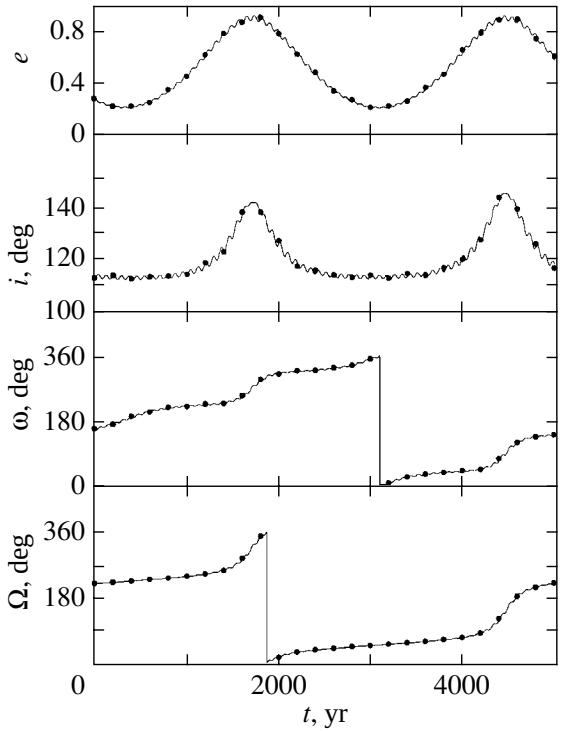

Fig. 1. Time dependence of the elements of the evolving orbit of the Neptunian satellite S/2002 N1: the solid curves and the dots represent the numerical integration of the rigorous equations and the numerical–analytical method, respectively; the angular variables are in degrees.

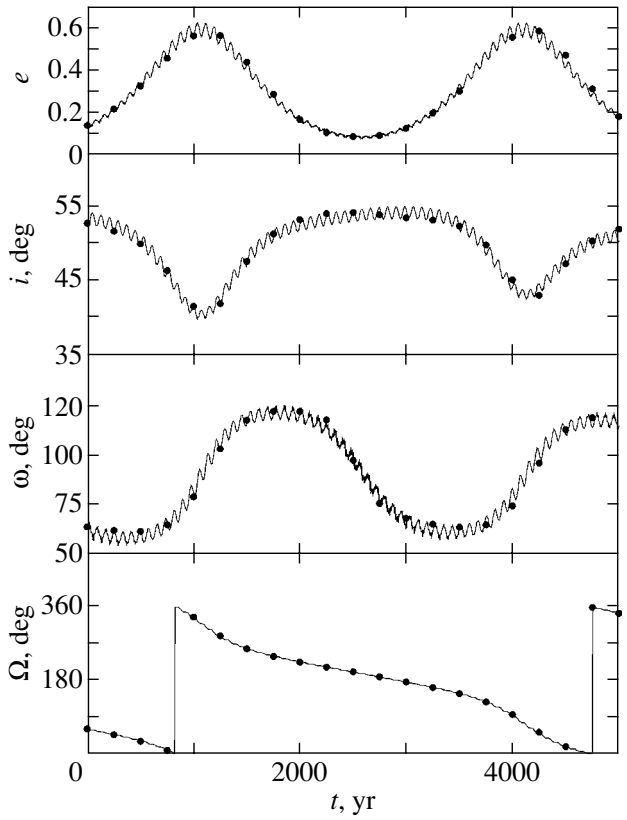

Fig. 2. Same as Fig. 1 for S/2002 N2.

improved orbit also proved to be qualitatively different; more specifically, the argument of pericenter was found to librate.

The two new satellites S/2002 N4 and S/2003 N1 discovered later (Marsden 2003e, 2003f) are the most distant satellites known to date. The semimajor axes of their orbits (a) are approximately 47 and 49 million km, respectively, or more than half of the radius of Neptune's sphere of influence with respect to the Sun. Furthermore, the evolution of the former is accompanied by librational variations in the argument of pericenter. Figures 1–5 show the time dependences of the orbital elements for the five satellites mentioned above.

In these figures, the solid curves and the dots represent the results of our numerical integration of the rigorous equations of satellite motion and the orbital elements obtained by the numerical–analytical method, respectively; e is the eccentricity, i is the inclination, ω is the argument of pericenter, and Ω is the longitude of the ascending node (the angular elements, in degrees, refer to the ecliptic and equinox 2000.0). The right-hand sides of the rigorous (unaveraged) equations include both the most important (solar) perturbations and the secondary perturbations from the oblateness of the central planet and the attraction by other planets. The time intervals for each orbit correspond roughly to T_ω and T_Ω, the periods of the variations in ω and Ω. The agreement between the two methodologically different results proves to be satisfactory for all of the satellites except the last. The results for the most distant satellite, S/2003 N1, graphically differ appreciably starting even from $t \approx 500$ yr (Fig. 5). This has been probably attributable to the large value of $\delta = n_N/n \approx 0.16$ (the ratio of the mean motions of Neptune and the satellite) and the insufficient accuracy of the numerical–analytical method constructed by including terms proportional to $\delta^{k\leq 4}$. This has been indirectly corroborated by the fact that, when the terms $\sim\delta^4$ were discarded as a test, the variation in ω for the orbit of this satellite was librational and did not correspond to the real circulation variation. Therefore, there is hope that including the terms $\sim\delta^5$ could lead to better quantitative agreement between the results. Note that a different number of approximations in Zeipel's method affects, in particular, the extreme eccentricities, with the effect being different for prograde and retrograde orbits; a detailed analysis

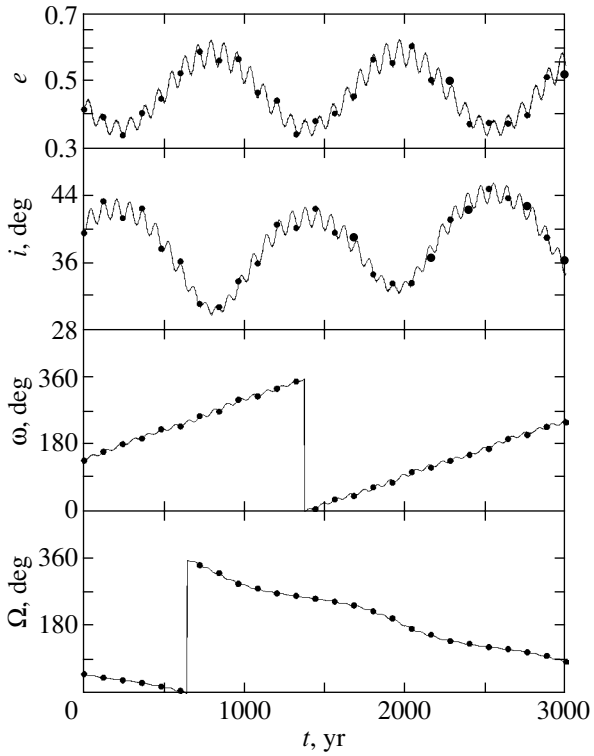

Fig. 3. Same as Fig. 1 for S/2002 N3.

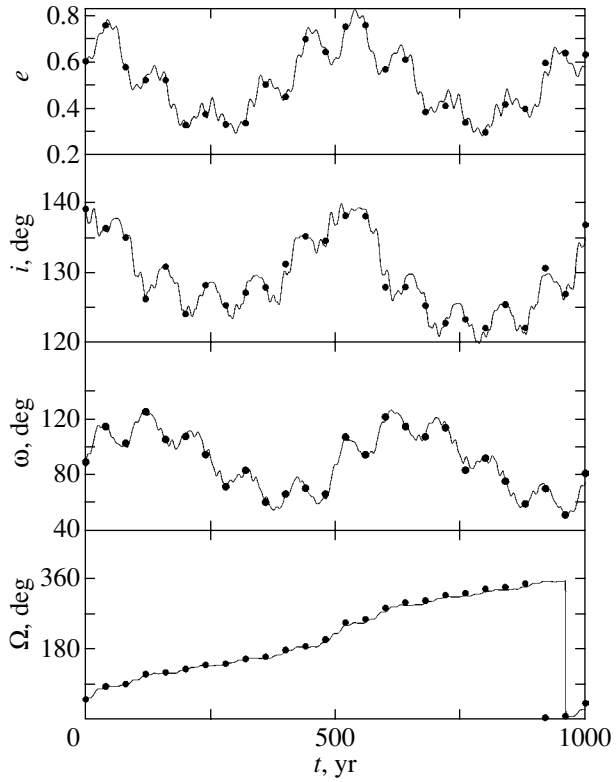

Fig. 4. Same as Fig. 1 for S/2002 N4.

for the outer Jovian satellites was performed by Orlov and Solovaya (1983).

The orbits of the Neptunian satellites under consideration are subject not only to secular and long-period perturbations, but also to perturbations with a period equal to half the orbital period of Neptune ($T_N/2 \approx 82.4$ yr), which is particularly clearly seen in Figs. 4 and 5. The short-period perturbations with the satellite orbital periods T also show up against the background of these variations in the intermediate period. These are most pronounced for the satellite S/2002 N2 ($T \approx 8$ yr, Fig. 6). For this satellite, Fig. 7 shows the differences between the orbital elements calculated by the above two methods on a long time interval (the elements obtained by numerically integrating the rigorous equations of motion are subtracted from those determined by the numerical–analytical method). The deviations δe of the order of several hundredths and δi, $\delta\omega$, and $\delta\Omega$ of the order of several degrees determine the time interval ~5000–6000 yr on which the proposed numerical–analytical method yields time dependences of the orbital elements that satisfactorily agree with those obtained by numerically integrating the rigorous equations of motion.

As regards the extreme eccentricities (e_{min}, e_{max}) and inclinations (i_{min}, i_{max}) of satellite orbits and the periods of the variations in the arguments of their pericenters (T_ω) and longitudes of the ascending nodes (T_Ω), this method is also applicable on longer time intervals. Table 1 gives the data obtained for a one-million-year time interval. For two ω-librators, we also give the amplitudes of the variations in the arguments of pericenter, $\delta\omega$, about one of the equilibrium values, $\omega^* = 90$.

THE EVOLUTION OF LIBRATIONAL ORBITS

Orbits with librational variations in the argument of pericenter exist in the satellite systems of all giant planets. Figures 8–11, which are similar to Figs. 1–5, show the time dependences of the elements for the evolving orbits of Uranian (S/2003 U3), Saturnian (S/2000 S5 Kiviuq, S/2000S6 Ijiraq), and Jovian (S/2003 J20) satellites.

Table 2, which is similar to Table 1, lists the evolution parameters of these orbits calculated by the numerical–analytical method on a time interval of one million years. We italicize the results obtained for the Saturnian satellites by Nesvorny *et al.* (2003) on a much longer time interval of 10^8 yr, which probably explains the difference in the extreme eccentricities and inclinations for the orbits of Kiviuq and Ijiraq.

All four orbits (as well as those of S/2002 N2 and S/2002 N4) satisfy the Lidov–Kozai resonance

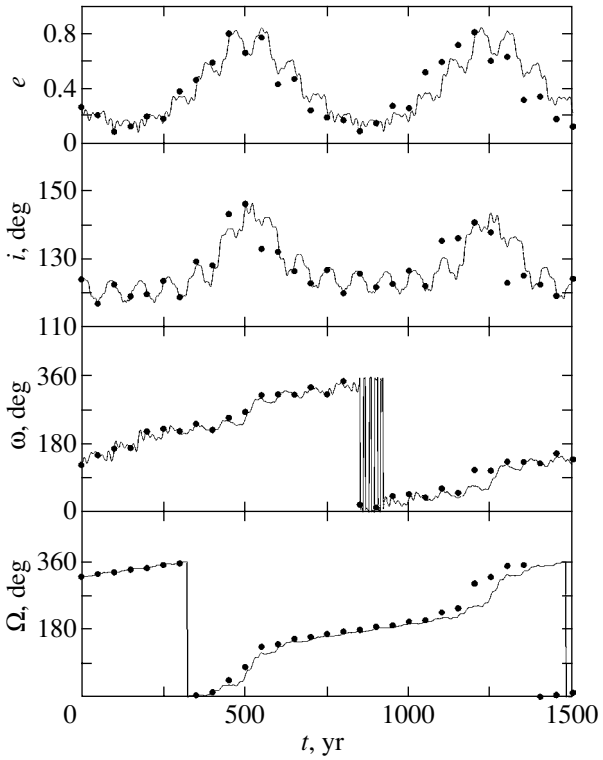

Fig. 5. Same as Fig. 1 but for S/2003 N1.

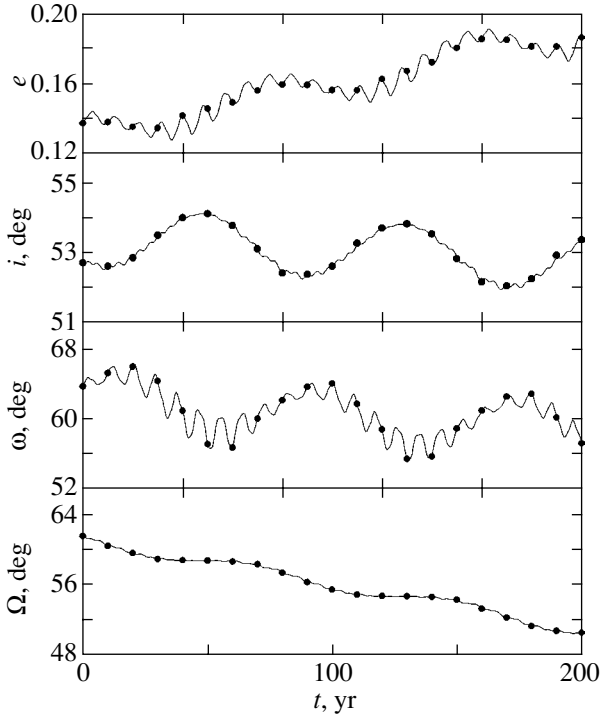

Fig. 6. Same as Fig. 2 for a 200-year time interval.

conditions

$$\dot{\omega} \approx 0, \quad c_1 < 3/5, \quad c_2 < 0, \tag{1}$$

where

$$c_1 = (1 - e^2)\cos^2 i = \text{const}, \tag{2}$$
$$c_2 = e^2(2/5 - \sin^2 i \sin^2 \omega) = \text{const}$$

and

$$c_0 = a = \text{const} \tag{3}$$

are the first integrals of Hill's double-averaged problem (Lidov 1961; Kozai 1962).

For orbits, the long-period perturbations of the elements e, i, and ω (together with the secular perturbations for Ω) noticeably predominate over the short- and intermediate-period perturbations.

The orbit of the satellite S/2001 J10 exhibits a distinctly different pattern of evolution. Figure 12 shows the results of our numerical integration of the rigorous equation of motion for this satellite.

For this orbit, the short-period perturbations of the elements e, i, ω and the perturbations of the intermediate period $T_J/2$ are comparable in amplitude to the long-period perturbations. The influence of the terms of the double-averaged perturbing function $\sim\delta^2$ proves to be negligible, so the variation of e, i, and ω is determined mainly by the terms $\sim\delta^3$. Therefore, although the ω-libration conditions in the model of Hill's double-averaged problem are not satisfied ($c_1 > 3/5$ and $c_2 > 0$ for this orbit), the ω libration actually takes place in the next approximation in δ. The extreme arguments of pericenter calculated by the numerical–analytical method are close to their values of 65° and 115° obtained by numerically integrating the rigorous equations of motion. However, the time dependences of the orbital elements differ significantly from those shown in Fig. 12. In particular, the two methods yield extreme eccentricities that differ by more than 0.1 on a 300-yr time interval. The influence of the terms $\sim\delta^3$ in the perturbing function, which predominate over the terms $\sim\delta^2$ for the orbit in question, appears to create difficulties in constructing the perturbation theory and require the development of its special version.

CONCLUDING REMARKS

We have briefly described and graphically illustrated the results of our study of the orbital evolution of distant satellites around the giant planets. The numerical–analytical method used is applicable to most of the satellites considered. It provides an accuracy of several hundredths and several degrees for the eccentricities and the angular variables, respectively, on time intervals of the order of several thousand years. This accuracy is high enough to find approximate time dependences of the orbital elements. This

Table 1. Orbital evolution parameters for the distant Neptunian satellites

Satellite	$e_{\min}$	$e_{\max}$	$i_{\min}$, deg	$i_{\max}$, deg	$\delta\omega$, deg	T_ω, yr	T_Ω, yr
S/2002 N1	0.188	0.905	109.0	145.1	Circulation	5600	4950
S/2002 N2	0.050	0.633	39.3	56.1	±36.1	3000	3900
S/2002 N3	0.332	0.624	29.3	45.9	Circulation	2350	3000
S/2002 N4	0.270	0.830	119.2	143.1	±39.6	500	1000
S/2003 N1	0.069	0.874	116.4	147.5	Circulation	1400	1300

Table 2. Evolution parameters for the ω-librators of Jupiter, Saturn, and Uranus

Satellite	$e_{\min}$	$e_{\max}$	$i_{\min}$, deg	$i_{\max}$, deg	$\delta\omega$, deg	T_ω, yr	T_Ω, yr
S/2003 J20	0.197	0.707	43.5	59.6	±31.6	60	100
S/2000 S5	0.142	0.553	39.5	53.4	±28.2	550	850
(Kiviuq)	0.0945	0.5713	40.33	52.68			
S/2000 S6	0.126	0.572	39.4	53.0	±29.0	600	800
(Ijiraq)	0.0940	0.5733	40.40	52.69			
S/2003 U3	0.440	0.859	45.0	67.9	±30.0	500	1000

method can also be used on longer time intervals to solve other evolution problems, in particular, to determine the extreme elements of evolving orbits. At the same time, we found that the method requires further

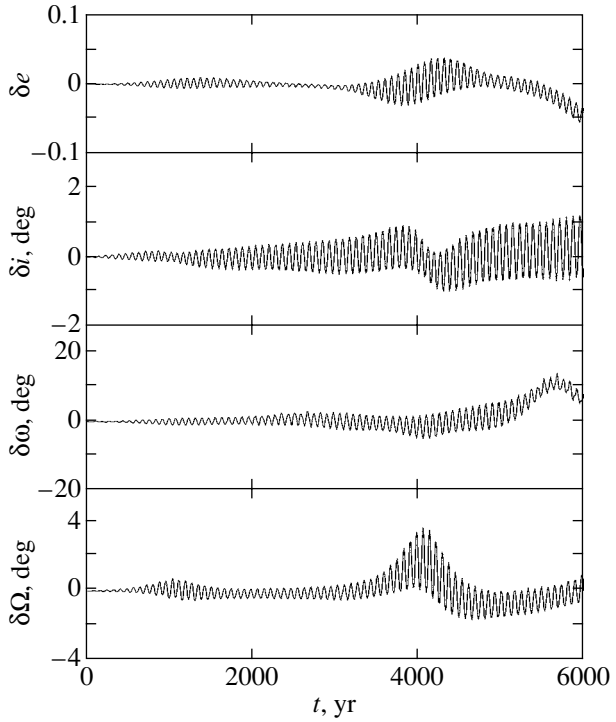

Fig. 7. Differences between the orbital elements of the satellite S/2002 N2 calculated by the two methods on a time interval of 6000 yr.

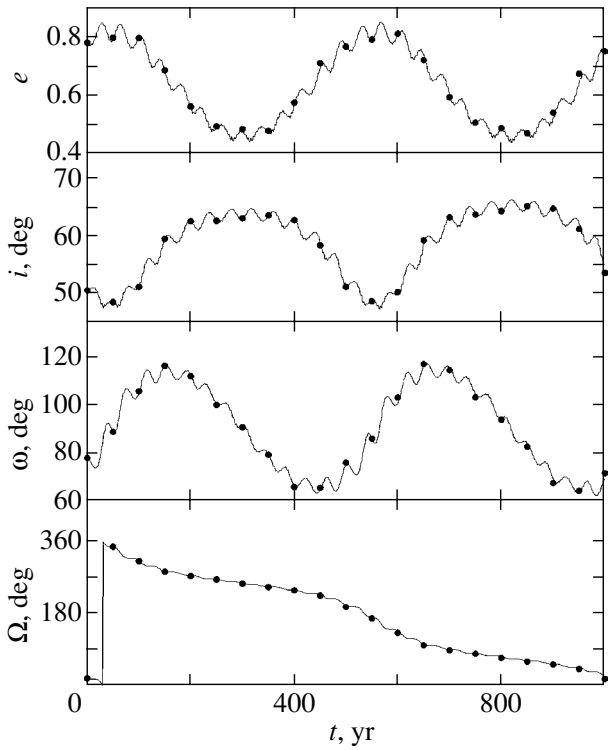

Fig. 8. Same as Fig. 1 for S/2003 U3.

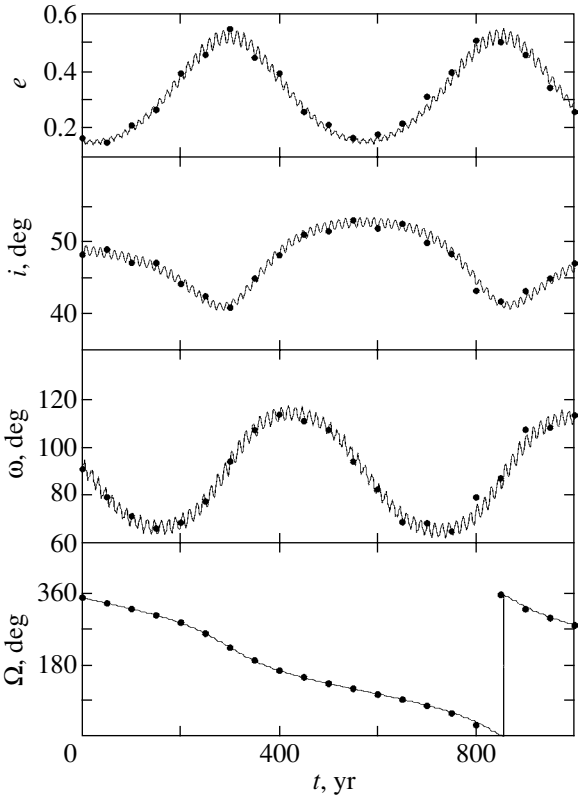

Fig. 9. Same as Fig. 1 for S/2000 S5 Kiviuq.

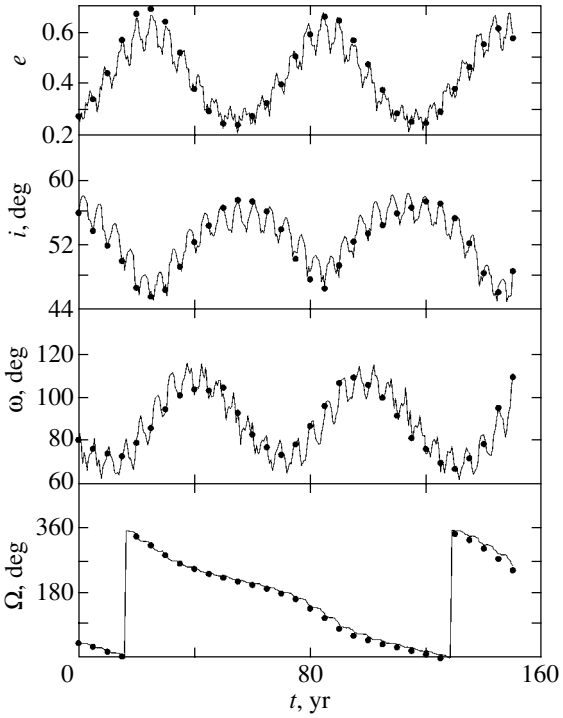

Fig. 11. Same as Fig. 1 for S/2003 J20.

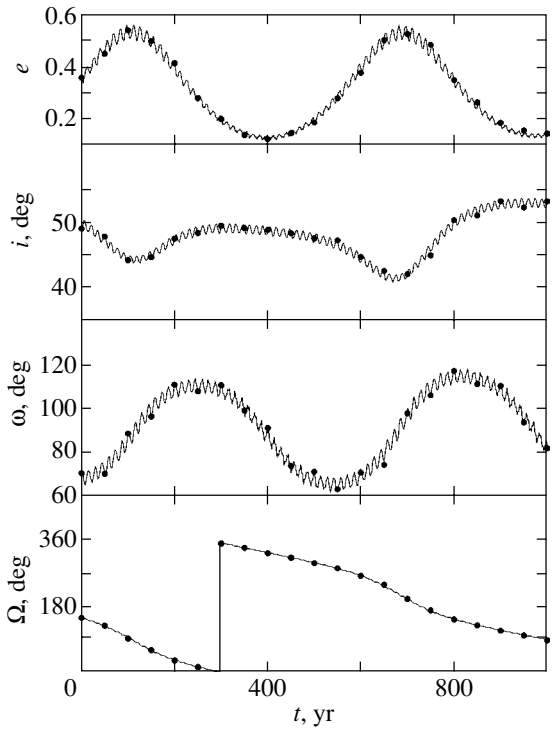

Fig. 10. Same as Fig. 1 for S/2000 S6 Ijiraq.

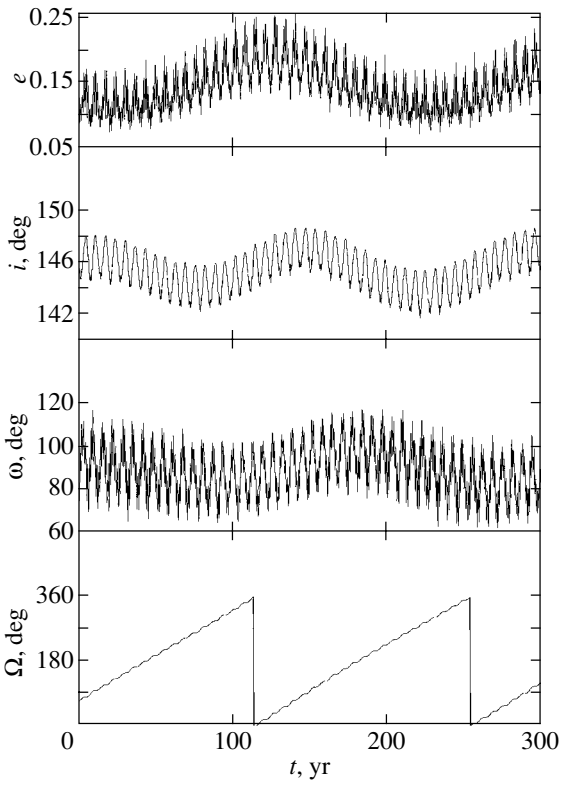

Fig. 12. Time dependences of the elements of the evolving orbit for the Jovian satellite S/2001 J10 (the numerical integration of the rigorous equations of motion).

methodological improvements. Our method proved to be not accurate enough for the satellite S/2003 N1 when a large parameter δ is used to construct the procedure of successive canonical transformations of Zeipel's method, while for the satellite S/2001 J10, a fundamentally new methodological approach to solving the evolution problem is required. This approach is described, for example, in the preprint by M. Cuk and J.A. Burns "On the Behavior of Irregular Satellites" (http://www.lanl.gov/abs/astroph/0408119) submitted for publication in *Astronomical Journal*. M. Cuk kindly sent me information about this preprint after the paper was submitted for publication.

REFERENCES

1. J. A. Burns, V. Carruba, D. Nesvorny, *et al.*, Amer. Astron. Soc., DDA Meeting **35**, 07.06 (2004).
2. M. Cuk and J. A. Burns, Amer. Astron. Soc., DDA Meeting **35**, 09.03 (2004).
3. Y. Kozai, Astron. J. **67**, 591 (1962).
4. M. L. Lidov, Iskusstvennye Sputniki Zemli **8**, 5 (1961).
5. B. G. Marsden, MPECirc. R18 (2003a).
6. B. G. Marsden, MPECirc. S95 (2003b).
7. B. G. Marsden, MPECirc. S106 (2003c).
8. B. G. Marsden, MPECirc. S67 (2003d).
9. B. G. Marsden, MPECirc. S107 (2003e).
10. B. G. Marsden, MPECirc. R19 (2003f).
11. D. Nesvorny, J. L. A. Alvarellos, L. Dones, *et al.*, Astron. J. **126**, 398 (2003).
12. A. A. Orlov, Byull. Inst. Teor. Astron. **5** (118), 360 (1965).
13. A. A. Orlov and A. A. Solovaya, Vestn. Mosk. Univ., Ser. 3: Fiz., Astron. **24**, 23 (1983).
14. V. S. Ural'skaya, Astron. Vestn. **37**, 371 (2003) [Solar Syst. Res. **37**, 337 (2003)].
15. M. A. Vashkov'yak, Pis'ma Astron. Zh. **29**, 782 (2003) [Astron. Lett. **29**, 695 (2003)].
16. M. A. Vashkov'yak, Pis'ma Astron. Zh. **31**, 66 (2005).

Translated by A. Dambis

Astronomy Letters, Vol. 31, No. 2, 2005, pp. 73–79. Translated from Pis'ma v Astronomicheskiĭ Zhurnal, Vol. 31, No. 2, 2005, pp. 83–90.

Search for Gravitational Lenses Near the Extragalactic Double Object CSL-1

M. V. Sazhin[1*], O. S. Khovanskaya[1], M. Capaccioli[2,3], G. Longo[3], J. M. Alcalá[2], R. Silvotti[2], and M. V. Pavlov[2]

[1] *Sternberg Astronomical Institute, Universitetskiĭ pr. 13, Moscow, 119992 Russia*

[2] *Osservatorio Astronomico di Capodimonte, via Moiariello 16, I-80131 Napoli, Italy*

[3] *Dipartimento di Scienze Fisiche, Univ. Federico II, Polo delle Scienze e della Tecnologia, via Cinthia, 80126 Napoli, Italy*

Received June 17, 2004

Abstract—We consider additional arguments in favor of the first observable cosmic string. We discuss candidates for gravitational lensing events near the extragalactic double source CSL-1 (Capodimonte-Sternberg-Lens Candidate no. 1) discovered in the Osservatorio Astronomico di Capodimonte Deep Field (OACDF). The detected excess of candidates for such events cannot be explained in terms of the theory of gravitational lensing by standard extragalactic objects (galaxies, groups of galaxies, etc.) and is in close agreement with the proposed model of gravitational lensing by a cosmic string. © *2005 Pleiades Publishing, Inc.*

Key words: *theoretical and observational cosmology, gravitational lensing, cosmic string.*

INTRODUCTION

In recent decades, cosmic strings have been widely discussed in theoretical cosmology (Zeldovich 1980; Vilenkin 1981). As was pointed out, for example, by Allen and Shellard (1990), the theoretically predicted number of cosmic strings in the Universe must be fairly large, but all attempts to observe at least indirect manifestations of cosmic strings have failed so far.

Sazhin *et al.* (2003, 2004) considered the unusual photometric and spectroscopic properties of the extragalactic double source CSL-1 (Capodimonte-Sternberg-Lens Candidate no. 1), discovered in the Osservatorio Astronomico di Capodimonte Deep Field (OACDF).

CSL-1 is either a system of two resolved giant low-ellipticity galaxies with an absolute magnitude of $M_R = -22.3 \pm 0.1$ and the same redshift $z = 0.46 \pm 0.008$, or one such galaxy and its image produced by gravitational lensing. The distance from the barycenter of the Solar system to CSL-1 is about 1900 Mpc (the Hubble parameter is $H = 65$ km s^{-1} Mpc^{-1}). The visual angular separation between the components of the pair is $1''.9$. Although the object belongs to an open cluster of galaxies, the field is highly rarefied: other extragalactic objects are offset by distances from several arcseconds to several arcminutes (Fig. 1).

An important peculiarity of the two images is that they are resolved and their isophotes (the sections of the three-dimensional brightness distribution by surfaces of constant brightness) are undistorted. Thus, the nature of CSL-1 can be interpreted in only two ways. Either we are dealing with two noninteracting galaxies that are identical both morphologically and spectroscopically and that are arranged in such a way that the visual separation between them corresponds to the observed $1''.9$, or CSL-1 is the result of the gravitational lensing of a galaxy by an object with the distinctive property of not distorting the isophotes of the extended background lensed galaxy.

The first of these interpretations was considered in detail by Khovanskaya and Sazhin (2005). These authors placed constraints on the maximum and minimum physical separations between the galaxies by analyzing the observational data and showed that the probability of this projection of two galaxies is extremely low, attributable primarily to the high correlation between the two spectra of the pair.

As regards the second interpretation, it is important to note that, despite their variety, the standard gravitational lenses (galaxies, groups of galaxies, dark compact lenses, etc.) are three-dimensional (mostly ellipsoidal) objects and, thus, produce a nonuniform gravitational field that distorts significantly the background lensed objects (Zakharov and Sazhin 1998; Schneider *et al.* 1992; Keeton 2002).

*E-mail: sazhin@xray.sai.msu.ru

1063-7737/05/3102-0073$26.00

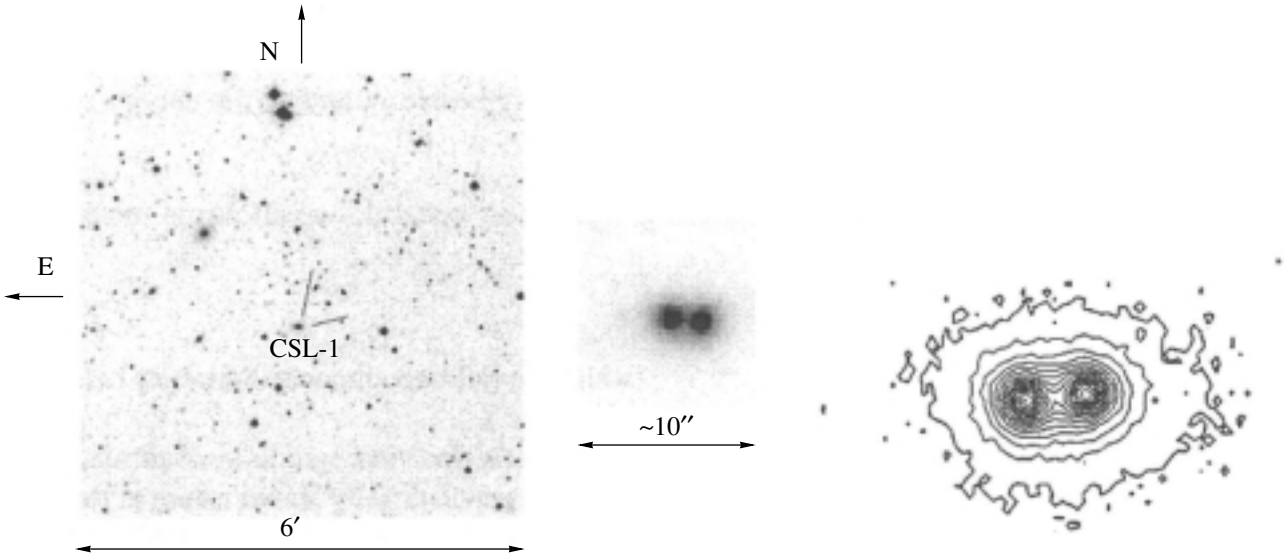

Fig. 1. CSL-1 in the R filter (on the left and at the center). The separation between the brightness centers of the pair components is $1\overset{''}{.}9$. One image pixel corresponds to $0\overset{''}{.}238$, the angular resolution is $\sim 1''$, and the photometric accuracy is 10%. Each of the pair components is a giant low-ellipticity galaxy with a redshift of $z = 0.46 \pm 0.008$ and an absolute magnitude of $M_R = -22.3 \pm 0.1$. Isophotes in the 914-nm filter, i.e., the sections of the three-dimensional brightness distribution by surfaces of constant brightness at certain steps, are shown on the right. The brightness profile of CSL-1 corresponds to de Vaucouleurs's law.

The only known gravitational lens that does not distort the background images is a cosmic string. The cosmic strings that, according to theory, were produced by phase transitions in the early Universe may be considered one-dimensional objects with a high accuracy. The diameter of such a string is much smaller than its length.

Having analyzed the observational data, Sazhin *et al.* (2003) found the deficit angle of a cosmic string to be $1\overset{''}{.}9$. This corresponds to a linear string density of $4 \times 10^{-7} m_{\rm Pl}^2$ in Planck units or 5.4×10^{21} g cm^{-1}.

There are several methods for identifying cosmic strings. In particular, cosmic strings can be identified by rapid variability in extragalactic objects (Sazhin and Khlopov 1988; Schild *et al.* 2004). Cosmic strings can also be detected by anisotropy in the cosmic microwave background radiation: Sazhin *et al.* (2003) initiated a search for cosmic string by statistically analyzing the WMAP data (Jeong and Smoot 2004). Note that the upper limit on the deficit angle given by Jeong and Smoot is larger than that obtained by Sazhin *et al.* (2003).

Sazhin *et al.* (2003) and Khovanskaya and Sazhin (2005) showed that observations with an angular resolution of several milliarcseconds and with a higher photometric accuracy are required to unequivocally disentangle these two interpretations of the object CSL-1. However, since there are no such observations, the second method must be used. It has been theoretically substantiated by Vilenkin and Shellard (1994), Hindmarsh (1990), Bernardeau and Uzan (2001), de Laix and Vachaspati (1996), and Huterer and Vachaspati (2003). Here, we effectively apply this method to the observational data obtained by a ground-based telescope with an angular resolution of the order of one arcsecond, since it does not require the high angular resolution mentioned above.

Let us consider this method.

The projection of a background lensed extragalactic object (galaxy) into the deficit angle of a cosmic string is a random process determined by the surface density of the distribution of extragalactic objects that are background ones with respect to the string and by the area of the band in which the string lies. The band area is determined by the band width and the string length. The angular width of the band is the deficit angle; the length of the string depends on its geometry and can vary from minimum (straight string) to maximum (Brownian string).

If we assume *a priori* that there is a cosmic string in a field, then the number of gravitational lensing events will clearly increase with increasing area of this field. All of the background lensed objects and their gravitational-lens images will be located along the string in a narrow band whose angular width is equal to the string deficit angle. Speaking metaphorically, a new milky way of galaxies and their gravitational-lens images must be formed along the string, and the

string configuration in the sky can clearly be reconstructed from this trace.

We will consider only galaxies as the background lensed objects; quasi-stellar background objects at optical wavelengths may be disregarded.

In the simplest case of a straight string, we can easily estimate the expected number N of lensed galaxies. Their mean number is

$$\langle N\rangle = n_{\rm g} 2\delta l, \qquad (1)$$

where $n_{\rm g}$ is the galaxy density per unit solid angle, δ is the deficit angle of the cosmic string, and l is the string length in the chosen field; δ and l are the angles.

In general, the string is bent (Huterer and Vachaspati 2003). Clearly, the length of such a string in the chosen field will be larger than the length of a straight string in the same field:

$$l = R\,(R/l_{\rm c})^{a}\,,$$

where $l_{\rm c}$ is the correlation length of the string, $R = |\mathbf{r} - \mathbf{r}_1|$ is the separation between the points $\mathbf{r}$ and $\mathbf{r}_1$, and the parameter a changes from zero (a straight string) to one (a randomly bent string).

More specifically, $a = 1$ corresponds to the Brownian bending of the string (an illustrative interpretation: if a particle executed a Brownian motion, then its path would correspond to the location of the string); in this case, $R \sim \sqrt{l}$. The band area of a bent string will also be larger than that of a straight string.

For $a = 1$, the expected number of gravitational lenses can be estimated as follows:

$$\langle N\rangle = 2\frac{\delta}{l_{\rm c}} n_{\rm g}\Omega.$$

The product of the area of the chosen sky region Ω and the surface density of galaxies $n_{\rm g}$ is the total number of galaxies in this field.

In this paper, as previously (Sazhin *et al.* 2003), we consider the OACDF R filter as the main one. Thus, our goal is to estimate (for the R filter) the expected number of lensed galaxies with magnitudes as faint as the maximum accessible (in OACDF) magnitude ($\sim 24 m_{\rm R}$) in the field with CSL-1.

For the number of lensed galaxies to be counted, we must know the mean number of galaxies in this field whose magnitudes lie within a certain interval. It is important to note that there are virtually no counts of faint sources for the R filter in the literature (see, e.g., Kummel and Wagner 2001; Gardner *et al.* 1996; Thomson *et al.* 1999; Gardner 1998, based on Hubble Space Telescope observations). Thus, the available data must be interpolated to be used in our problem.

The available data reveal that the galaxy number counts have a large uncertainty (by an order of magnitude) in the magnitude interval $20 < m < 24$. Using the data from Kummel and Wagner (2001) and extrapolating them to a magnitude of $m_R = 24$, we find that the total number of galaxies in the interval $20 < m_R < 24$ in the CSL-1 field ($16' \times 16'$) is $\sim$2200. This number corresponds to the number of extended sources counted in the OACDF. Thus, the estimate obtained (2200 galaxies) is in good agreement with the number of galaxies that are actually observed in the OACDF in the same magnitude interval.

According to our modeling, on average, about nine gravitational lensing events are expected along a straight string. About 200 gravitational lensing events whose number depends on the parameter a are expected for a randomly bent string.

It is important to note that, in addition to the events of gravitational lensing by a string, a number of standard events of gravitational lensing by galaxies and other well-studied objects will clearly be observed in the field under consideration. The mean density of the galaxies lensed by standard objects and the role of this effect in cosmology have been considered by many authors (see, e.g., Fukugita *et al.* 1992; Kochanek 1993; Chiba and Yoshi 1999; Ofek *et al.* 2003). The mean number of such events in the CSL-1 field ($16' \times 16'$) in the magnitude interval $20 < m_R < 24$ is no more than two (Covone *et al.* 2004), almost an order of magnitude smaller than the expected number of gravitational lensing events even for a straight cosmic string.

Thus, if the number of gravitational lensing events in the above field will be much larger than the expected mean number of such events, this would be a major argument for the presence of a cosmic string in this field.

GRAVITATIONAL-LENS CANDIDATES NEAR CSL-1

Modeling the Gravitational Lensing by a Cosmic String

We modeled the gravitational lensing of background extragalactic sources by a straight cosmic string for the real distribution of galaxies as follows: We chose a 1000×1000-pixel field, with each pixel corresponding to a resolution of $0''.238$ (for correspondence to the real OACDF resolution). Thus, the model field covers a $4' \times 4'$ region and contains about 100 galaxies (which corresponds to the expected number of galaxies in the field of this size and in the magnitude interval $20 < m_R < 24$ (see Thomson *et al.* 1999; Gardner 1998) and was confirmed by the OACDF observations). The brightness profile of each galaxy was assumed to be proportional

to $r^{1/4}$ (de Vaucouleurs's law); for simplicity, the brightness was set equal to zero starting from ten effective radii. In the model field, such galaxies were distributed randomly; their absolute magnitudes were also distributed randomly in the interval $20 < m_R < 24$. Subsequently, we smoothed the model images of galaxies with a function that matched the experimentally measured OACDF point spread function (PSF) (the resolution of the telescope) and added noise with a Gaussian distribution with a zero mean and a variance corresponding to the noise variance of the real field containing CSL-1 (in the R filter). For simplicity, the cosmic string was assumed to be straight and crossing the model field vertically.

As soon as the angular separation between the galaxy and the string becomes smaller than the string deficit angle, a gravitational lensing event occurs.

We performed our modeling for several model fields by comparing the results of various model fields. On average, three to five events of gravitational lensing of galaxies by the string were found. This result closely agrees with the theoretical predictions (see (1)).

Thus, our modeling indicates that, if there is a straight cosmic string in a $4' \times 4'$ field, then, on average, three to five events of gravitational lensing of background galaxies with magnitudes in the interval $20 < m_R < 24$ must be observed.

The Real Field

After our modeling, we studied the real field with CSL-1 in an effort to find and count the number of gravitational lensing events and to compare the number of such events with the observational statistics of standard gravitational lensing events and with the theoretical statistics of gravitational lensing events induced by a cosmic string.

Thus, we visually inspected the OACDF 4000×4000-pixel field with CSL-1 at the center. The OACDF is a deep image of the sky region in four broad-band color filters: U (ultraviolet), B (blue), V (visible), R (red), and in seven narrow-band filters: 753, 770, 791, 815, 837, 884, 914 nm (for a detailed description of the OACDF, see, e.g., Alcalá *et al.* 2004). If there is a straight cosmic string in this field, then, according to the modeling results presented in the previous section, seven to nine gravitational lensing events may be expected. Clearly, there must be more such events in the case of a bent string.

To select gravitational-lens candidates, we used the following necessary conditions (Schneider *et al.* 1992):

(1) Two or more images must be separated by a small angular distance;

(2) The ratios of the image intensities must be the same in all color filters.

To be more precise, we searched for objects separated by an angular distance of no less than one arcsecond (this value is determined by the maximum resolution of the telescope in the field under consideration) and no more than four arcseconds (this value is determined by the deficit angle of the presumed cosmic string, which, in turn, is determined from the angular separation between the components of the pair CSL-1).

To estimate the ratio of the image intensities, we introduced the functions $\{e_i\}$, $i = 1, \ldots, N$, where N is the number of filters. In particular, if $i = 1$, then

$$e_1 = e_{RV} = 1 - \frac{I_R}{I_r}\frac{I_v}{I_V}.$$

Here, I_R is the intensity of the R-filter light from the brighter object of the close pair, I_r is the intensity of the R-filter light from the fainter component of the pair, I_V is the intensity of the V-filter light from the brighter object of the close pair, and I_v is the intensity of the V-filter light from the fainter component of the pair.

By analogy, we can introduce the functions $\{e_i\}$ to compare the image intensities in the R filter and in all of the OACDF filters: $e_2 = e_{RB}$, $e_3 = e_{R753}$, $e_4 = e_{R770}$, etc.

If the objects are gravitational lenses in nature, then, according to the second necessary condition, all of their functions $\{e_i\}$ must become equal to zero. Clearly, the functions $\{e_i\}$ for the real data will not be strictly equal to zero due to observational errors. To estimate the error, let us calculate the functions $\{e_i\}$ for CSL-1, which, as follows from the spectral analysis performed by Sazhin *et al.* (2003) and Khovanskaya and Sazhin (2004), is a gravitational-lens object with a high probability.

The functions $\{e_i\}$ can be expressed in terms of the magnitudes of the objects in various filters. Thus, for example, for $e_1 = e_{RV}$:

$$-2.5\log(1 - e_{RV}) = m_{1R} - m_{2R} + m_{2V} - m_{1V}.$$

Here, m_{1R}, m_{2R}, m_{2V}, and m_{1V} are the brighter and fainter components of CSL-1 in the R and V filters, respectively. Since the error in the magnitude (photometric accuracy) is $\sim 10\%$ and since all magnitudes are independent, the function e_1 contain an error of about $\sqrt{4} \times 10\% = 20\%$.

Thus, the error in the functions $\{e_i\}$ is 20%. In general, the spectra of gravitational-lens candidates, as was done for CSL-1, are required to achieve a higher accuracy; this will be done in the future.

A visual inspection of the CSL-1 field revealed 47 candidates, from which we subsequently chose

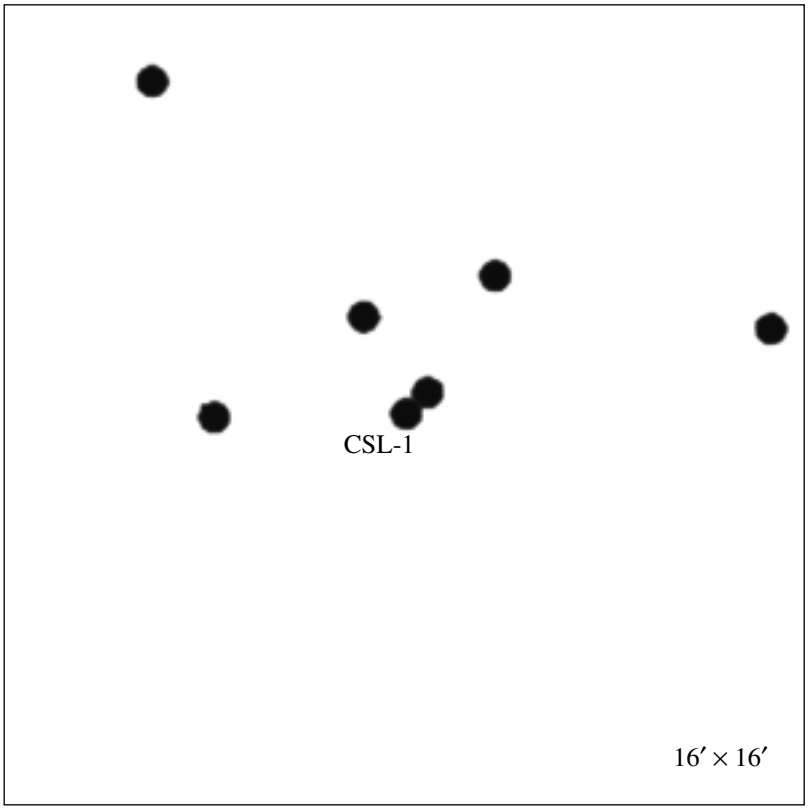

Fig. 2. The six brightest gravitational-lens candidates found in the 16′ × 16′ field are indicated by the filled circles. Each circle corresponds to one pair. CSL-1 is located at the center of the field.

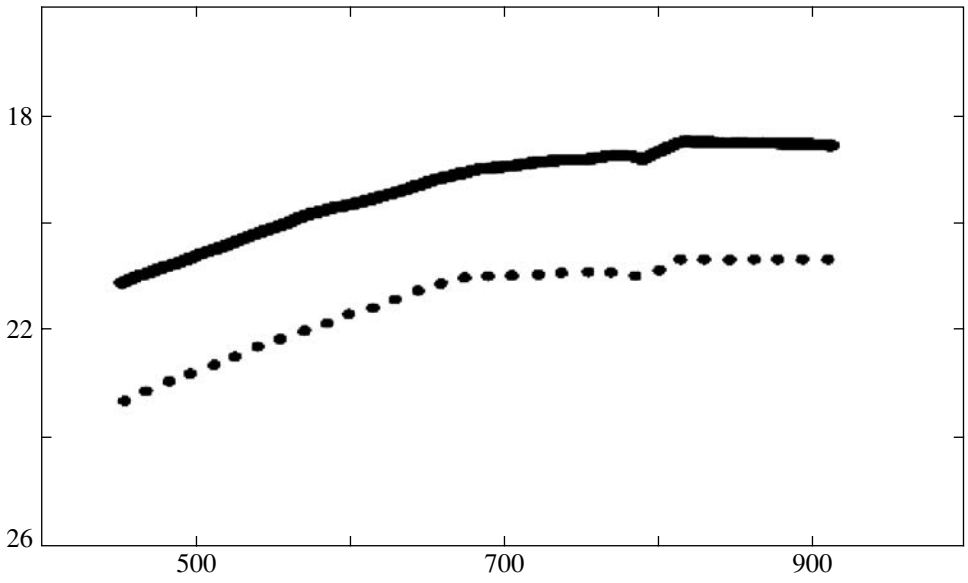

Fig. 3. Spectral distribution for a typical gravitational-lens candidate constructed from the OACDF observations in four broad-band color filters: U (ultraviolet), B (blue), V (visible), R (red), and in seven narrow-band filters: 753, 770, 791, 815, 837, 884, 914 nm. The filters and absolute magnitudes are along the horizontal and vertical axes, respectively. The solid and dotted lines represent the brighter and fainter components of the pair, respectively.

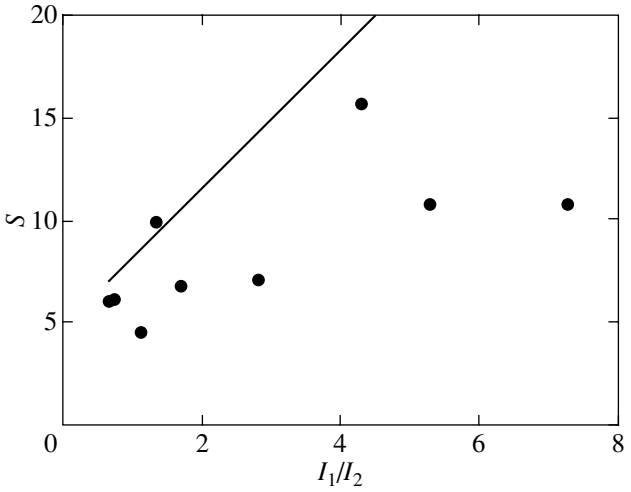

Fig. 4. Weak correlation of the angular separation between the brightness centers of a background object and its gravitational-lens image with their magnitude difference: the dots represent the observations of candidates, and the solid line represents the expected theoretical prediction made by modeling. The exposure ratio I_1/I_2 of the brighter and fainter components of the pair (in the R filter) is along the horizontal axis; the angular separation S between the pair components (in pixels, one pixel is $0''.238$) is along the vertical axis.

the best eleven candidates that satisfied the above two necessary conditions (see Fig. 2). The number of candidates is in good agreement with the scenario for the gravitational lensing of background galaxies by a cosmic string under consideration. All of them are mostly faint: their R magnitudes lie within the interval from 19^m to 24^m, as expected (see, e.g., Huterer and Vachaspati 2003). It is also important to note that all of the candidates brighter than 21^m are extended objects.

As an example, Fig. 3 shows the spectral distribution for candidate no. 1. Within the error limits, the spectra of the remaining candidates show a similar pattern of behavior.

It is important to note that the match between the colors based on broad-band and narrow-band photometry is only a necessary condition in our case. It also becomes a sufficient condition for identifying gravitational microlensing events (Zakharov and Sazhin 1998; Alcock *et al.* 1993). This is quite natural, since when gravitational microlensing events are observed from Earth, we cannot separately observe the two images and take photographs of their spectra. For the gravitational lensing of extragalactic objects, we can separately observe each of the images. Thus, identifying the two spectra (not the colors) is a necessary and sufficient condition for the identification of gravitational lenses (Schneider *et al.* 1992; Zakharov 1997).

CORRELATION OF THE ANGULAR SEPARATION BETWEEN CANDIDATES WITH THEIR MAGNITUDE DIFFERENCE

Theory predicts that when a pointlike background source is gravitationally lensed by a cosmic string, the angular separation between the images must be exactly equal to the deficit angle of the string. When an extended background source is gravitationally lensed by a cosmic string, we expect a weak correlation of the separation between the brightness centers of the source and its image with the magnitude difference between the source and its image. More specifically, when a small part of the extended background object falls within the string band, a weak image is formed on the opposite side of the string band. In this case, the separation between the brightness centers is, clearly, the sum of the deficit angle (the string band width) and the size of the object itself. Thus, there is a correlation between the intensity ratio of the object and its image and the angular separation between the brightness centers.

In Fig. 4, the angular separation (in pixels, one pixel is $= 0''.238$) between the brightness centers is plotted against the exposure ratio (in the R filter) for the brightest candidates found. The observed weak correlation is another argument for the presence of a cosmic string in the CSL-1 field.

CONCLUSIONS

Sazhin *et al.* (2003) and Khovanskaya and Sazhin (2005) discussed in detail the properties of the double object CSL-1, a system of two resolved low-ellipticity galaxies with identical spectra and redshifts and an angular separation of $\sim 2''$. Sazhin *et al.* (2003) showed that this object could be interpreted as the first observed result of the gravitational lensing of a galaxy by a cosmic string. Khovanskaya and Sazhin (2004) considered in detail the possibility of a chance projection of two galaxies as an alternative explanation of the nature of CSL-1; this explanation runs into several difficulties, the most important of which is the identity of the spectra for the two components.

In this paper, based on the suggestion that the cosmic string has an extended structure and forms nonlocal inhomogeneities in the Universe, we analyzed the statistics of gravitational lensing events near the double object CSL-1.

According to our modeling, on average, seven to nine gravitational lensing events were expected in the CSL-1 field, as confirmed by a visual inspection of the

$16' \times 16'$ field with CSL-1 at the center. Using the introduced functions $\{e_i\}$, we found eleven candidates that possess all of the properties of gravitational-lens objects (Schneider *et al.* 1992). This number is almost an order of magnitude larger than the mean expected number of standard gravitational lensing events, i.e., lensing by galaxies, groups of galaxies, and other objects with well-studied properties.

More accurate spectroscopic studies of the candidates found are needed, since the available data argue for the gravitational-lens nature of these objects only with an accuracy of no more than 20%.

ACKNOWLEDGMENTS

M.V. Sazhin is grateful to the Osservatorio Astronomico di Capodimonte for financial support. This work was supported by the Russian Foundation for Basic Research (project no. 04-02-17288). We wish to thank A.N. Vilenkin for his interesting discussions and a number of useful remarks.

REFERENCES

1. J. M. Alcalá, M. Pannella, E. Puddu, *et al.*, Submitted to Astron. Astrophys. (2004); astro-ph/0408220.
2. C. Alcock, C. W. Akerloff, R. A. Allsman, *et al.*, Nature **365**, 621 (1993).
3. B. Allen and E. P. S. Shellard, Phys. Rev. Lett. **64**, 119 (1990).
4. F. Bernardeau and J.-P. Uzan, Phys. Rev. D **63**, 023 005 (2001).
5. M. Chiba and Yu. Yoshi, Astrophys. J. **510**, 42 (1999).
6. G. Covone, R. de Ritis, E. Piedipalumbo, and M. Sereno, Submitted to Mon. Not. R. Astron. Soc. (2004).
7. M. Fukugita, T. Futamase, T. Kasai, and E. L. Turner, Astrophys. J. **393**, 3 (1992).
8. J. Gardner, Publ. Astron. Soc. Pac. **110**, 291 (1998).
9. J. P. Gardner, R. M. Sharples, B. E. Carraso, and C. S. Frenk, Mon. Not. R. Astron. Soc. **282**, L1 (1996).
10. A. Hindmarsh, *The Formation and Evolution of Cosmic Strings*, Ed. by G. Gibbons, S. W. Hawking, and T. Vachaspathi (Cambridge Univ. Press., Cambridge, 1990).
11. D. Huterer and T. Vachaspati, astro-ph/0305006 (2003).
12. E. Jeong and G. F. Smoot, astro-ph/0406432 (2004).
13. Ch. Keeton, http://cfa-www.harvard.edu/castles/ (2002).
14. O. S. Khovanskaya and M. V. Sazhin, Astron. Zh. (2005, in press).
15. C. S. Kochanek, Mon. Not. R. Astron. Soc. **261**, 453 (1993).
16. M. W. Kummel and S. J. Wagner, astro-ph/0102036 (2001).
17. A. A. de Laix and T. Vachaspati, Phys. Rev. D **54**, 4780 (1996).
18. E. O. Ofek, H-W. Rix, and D. Maoz, Mon. Not. R. Astron. Soc. **343**, 639 (2003).
19. M. V. Sazhin and M. Yu. Kholopov, Astron. Zh. **1**, 191 (1998).
20. M. Sazhin, O. Khovanskaya, M. Capaccioli, and G. Longo, in *Proceed. Conf. Thinking, Observing and Mining the Universe, Sorrento, Italy, September 22–27, 2004*.
21. M. Sazhin, G. Longo, M. Capaccioli, *et al.*, Mon. Not. R. Astron. Soc. **343**, 353 (2003).
22. R. E. Schild, I. S. Masnyak, B. I. Hnatyk, and B. I. Zhdanov, astro-ph/0406434 (2004).
23. P. Schneider, J. Ehlers, and E. E. Falco, *Gravitational Lenses* (Heidelberg, Springer, 1992).
24. R. I. Thomson, L. J. Storrie-Lombardi, R. Weymann, *et al.*, Astron. J. **117**, 17 (1999).
25. A. N. Vilenkin, Phys. Rev. D **23**, 852 (1981).
26. A. N. Vilenkin and E. P. S. Shellard, *Cosmic Strings and Other Topological Defects* (Cambridge Univ. Press., Cambridge, 1994).
27. A. F. Zakharov, *Gravitational Lenses and Microlenses* (Yanus, Moscow, 1997).
28. A. F. Zakharov and M. V. Sazhin, Usp. Fiz. Nauk **168**, 10 (1998).
29. Ya. B. Zeldovich, Mon. Not. R. Astron. Soc. **192**, 663 (1980).

Translated by V. Astakhov

Astronomy Letters, Vol. 31, No. 2, 2005, pp. 80–87. Translated from Pis'ma v Astronomicheskiĭ Zhurnal, Vol. 31, No. 2, 2005, pp. 91–98.

Leading Wave as a Component of the Spiral Pattern of the Galaxy

A. M. Mel'nik*

Sternberg Astronomical Institute, Universitetskiĭ pr. 13, Moscow, 119992 Russia

Received June 8, 2004

Abstract—The spiral pattern of the Galaxy, identified by analyzing the kinematics of young stars within 3 kpc of the Sun, is Fourier decomposed into spiral harmonics. The spiral pattern of the Galaxy is shown to be representable as a superposition of trailing and leading waves with interarm distances of $\lambda = 1.8 \pm 0.4$ and 4 ± 2 kpc, respectively. Shock waves are probably present only in the portions of the trailing spiral pattern where it crosses the crest of the leading wave. The small interarm distance of the trailing spiral wave ($\lambda = 1.8$ kpc) can be explained by its evolution—by the decrease in the interarm distance as the wave is displaced toward the inner Lindblad resonance. The Carina arm may be part of this resonance ring.

Key words: *Galaxy, spiral pattern, kinematics and dynamics, Fourier analysis.*

INTRODUCTION

An analysis of the velocity field for young stars (OB associations and Cepheids) revealed periodic variations in the radial and azimuthal components of the residual velocity along the Galactic radius vector with an amplitude of $f_R = f_\theta = 7 \pm 2$ km s^{-1} and a scale length of $\lambda = 2 \pm 0.2$ kpc (Mel'nik *et al.* 1999, 2001). We determined the kinematic locations of the Carina, Cygnus, and Perseus arms as the locations of the minima in the distribution of the radial residual velocity of OB associations. The identified arm fragments deviate from an ideal spiral pattern (smooth trailing spiral arms). The Carina arm ($R = 6.5$ kpc) is displaced from the Cygnus arm ($R = 6.8$ kpc) so that together they fall best on the leading spiral arm. The Perseus arm unexpectedly terminates, and we see its extension in the III quadrant neither from the kinematics of young stars nor from the increase in the density of young objects. An analysis of various spur generation mechanisms showed that the identified arm fragments are not spurs and are located near the minimum of the potential (Mel'nik 2003). The potential perturbation itself is probably not an ideal monochromatic spiral wave.

Following Kalnajs (1975), let us assume that the spiral pattern of the Galaxy is a superposition of several spiral waves and let us try to identify the various components of its spiral pattern. Kalnajs (1975) was the first to perform a Fourier analysis of the spiral pattern of a galaxy using the distribution of H II regions in the galaxy M 31. This analysis revealed a dominant one-armed leading spiral in it.

The spiral pattern of the Galaxy is difficult to analyze, because we do not have a complete picture of the distribution of young objects in its disk. On the other hand, only our Galaxy makes it possible to identify arm fragments kinematically. Therefore, we have not just a sample of spiral-arm indicators, but a sample of potential-minimum indicators.

FOURIER ANALYSIS OF THE GALACTIC SPIRAL PATTERN IN THE SOLAR NEIGHBORHOOD

The Method and Models

The complex spiral pattern of any galaxy can be represented as a superposition of spiral components with different numbers of arms m, and each m-component, in turn, can consist of several spiral waves with different pitch angles.

An elementary logarithmic spiral wave is defined by the equation

$$R = R_1 e^{\tan i(\theta - \theta_1)}, \qquad (1)$$

where i is the pitch angle, θ and θ_1 are the Galactocentric angles, and R and R_1 are the Galactocentric distances.

The amplitudes of the spiral oscillations in the distribution of N objects in the galactic plane can be determined from the relation

$$A(p, m) = \frac{1}{N} \sum_{j=1}^{N} e^{-i[m\theta_j + p \ln(R_j/R_0)]}, \qquad (2)$$

where $p = -m/\tan i$ (Kalnajs 1975; Considere and Athanossoula 1982).

*E-mail: anna@sai.msu.ru

1063-7737/05/3102-0080$26.00

Only the interarm distance λ and, in certain cases, the sense of arm winding can be reliably determined by analyzing the spiral pattern of the Galaxy within 3 kpc of the Sun. The number of spiral arms m and their mean pitch angle i remain indeterminate, although all three parameters are related by

$$|\tan i| = \frac{\lambda m}{2\pi R_0}, \qquad (3)$$

where R_0 is the Galactocentric distance.

The number of spiral arms cannot be determined by analyzing the distribution of young stars within 3 kpc of the Sun, because all of the m-components are very similar to one another, and the Fourier amplitude $A(p, m)$ actually depends only on the parameter p. Therefore, only the Fourier spectrum of the $m = 1$ spiral component is shown on the plots.

Let us consider two models of the Galactic spiral arms: In model 1, the spiral pattern of the Galaxy is represented by 15 real OB associations (Blaha and Humphreys 1989) that are located near the minimum in the distribution of the radial residual velocity V_R and that have $V_R < -5$ km s^{-1}. Table 1 lists these associations together with their heliocentric (r, l, b) and Galactocentric (R, θ) coordinates and the residual velocities V_R. Figure 1a shows the locations and residual velocities of these associations in the Galactic plane and the circular arcs that correspond to the minima in the distribution of the radial residual velocity. We excluded from our analysis the OB associations Sco OB4 ($l = 353°$, $r = 1.0$ kpc, $V_R = -15$ km s^{-1}) and HD 156154 ($l = 351°$, $r = 2.1$ kpc, $V_R = -16$ km s^{-1}); although their residual velocities are $V_R < -5$ km s^{-1}, they deviate greatly from the observed periodic pattern of the velocity field of young objects.

In model 2, the distribution of young objects is modeled in a ring. The points representing the OB associations are randomly scattered over the ring $R_0 - 2 < R < R_0 + 2$ kpc, except for the 3 kpc solar neighborhood where they concentrate toward the three arcs corresponding to three fragments of the spiral pattern (Fig. 1b). Table 2 lists the Galactocentric angles of the beginning and end marks of these arcs $\theta_{\min}$ and $\theta_{\max}$ and their Galactocentric distances $R_{\rm arm}$. The points in the arms are distributed uniformly, and their radial distribution is limited to the interval $R = R_{\rm arm} \pm 0.2$ kpc. The total number of points in the arms is equal to the number of points that would fell within the selected region of the ring (within 3 kpc of the Sun) if it were filled uniformly and randomly. Of the 2000 objects scattered over the ring, 250 objects, on average, fall within the selected region, and 40, 20, and 40% of these fall within the Carina, Cygnus, and Perseus arms, respectively.

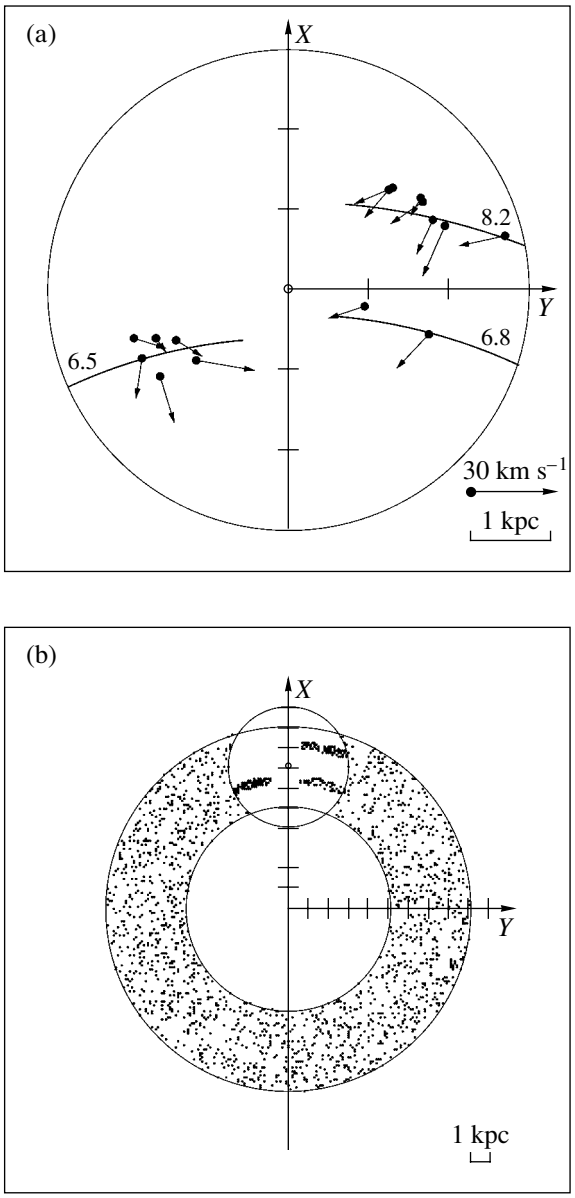

Fig. 1. Distribution of young objects in the Galaxy. (a) In model 1, the spiral pattern is represented by 15 real kinematically identified OB associations. The circular arcs correspond to the kinematic locations of the spiral arms. (b) In model 2, the young objects are randomly distributed in the ring $R_0 - 2 < R < R_0 + 2$ kpc, except for the 3 kpc solar neighborhood where they concentrate toward the identified fragments of the spiral pattern.

The modeled ring has a width of $\Delta R = \pm 2$ kpc, because we can ensure the completeness of our sample or, more specifically, the identification of all arm fragments in the solar neighborhood only in this interval. The tightly wound spiral pattern of the Galaxy forces us to be cautious, since the density of young objects changes much faster radially than azimuthally.

We assumed the distance to the Galactic center

Table 1. List of OB associations used in model 1

OB association	l	b	r, kpc	V_R, km s^{-1}	R, kpc	θ
Cyg OB3	72°.8	2°.0	1.8	−14.5	6.79	14°.93
Cyg OB9	77.8	1.8	1.0	−5.8	6.96	7.74
Cep OB1	104.2	−1.0	2.8	−8.7	8.23	19.08
Cas OB2	112.0	0.0	2.1	−19.0	8.13	13.89
Cas OB5	116.1	−0.5	2.0	−12.7	8.18	12.73
Cas OB7	123.0	1.2	2.0	−10.3	8.36	11.61
Cas OB1	124.7	−1.7	2.0	−6.8	8.41	11.31
Per OB1	134.7	−3.2	1.8	−7.8	8.49	8.81
Cas OB6	135.0	0.8	1.8	−11.2	8.43	8.44
Coll 228	287.6	−1.0	2.0	−6.6	6.77	−16.42
Car OB2	290.4	0.1	1.8	−5.6	6.69	−14.20
Cru OB1	294.9	−1.1	2.0	−13.5	6.51	−16.23
NGC 3766	294.1	−0.0	1.5	−7.3	6.62	−12.15
Cen OB1	304.2	1.4	1.9	−16.8	6.23	−14.77
Hogg 16	307.5	1.4	1.5	−7.4	6.32	−10.52

to be $R_0 = 7.1$ kpc (Dambis *et al.* 1995; Glushkova *et al.* 1998) and shorten the distance scale for OB associations given by Blaha and Humphreys (1989) by 20% to reduce it to the so-called short distance scale (Dambis *et al.* 2001; Sitnik and Mel'nik 1996).

RESULTS

The heavy line in Fig. 2 indicates the Fourier decomposition of the distribution of 15 OB associations over the Galactic plane into logarithmic spiral waves. The parameter p, which characterizes the interarm distance $\lambda = 2\pi R_0/|p|$ and the sense of arm winding, is along the horizontal axis; $p > 0$ and $p < 0$ correspond to the trailing and leading arms, respectively. The absolute values of the amplitudes of the one-armed spiral waves $|A(p, 1)|$ are along the vertical axis. Figure 2 clearly shows three maxima. The leftmost and rightmost outside maxima at $p = -28$ and $p = +24$ correspond to a tightly would spiral pattern with $\lambda = 1.8 \pm 0.4$ kpc. The Fourier spectrum of the tightly wound spiral arm consists of a superposition of the leading and trailing components, since we consider only a small region where the tightly wound spiral arms are indistinguishable from circular arcs. The circular arc is decomposed into a superposition of leading and trailing spiral waves with approximately equal amplitudes and pitch angles $|i|$. The central maximum in Fig. 2 stems from the fact that we are dealing with a sample with a highly asymmetric distribution about the Galactic center. Indeed, all of the associations in model 1 are located within 3 kpc of the Sun rather than distributed over the entire Galactic disk. Such a cluster of objects corresponds to a spiral wave with an infinite pitch angle ($p = 0$). The width

Table 2. Parameters of the spiral pattern used in model 2

Arm fragments	$\theta_{\min}$	$\theta_{\max}$	$R_{\rm arm}$, kpc
Carina	−25°	−5°	6.5
Cygnus	+5	+25	6.8
Perseus	+5	+21	8.2

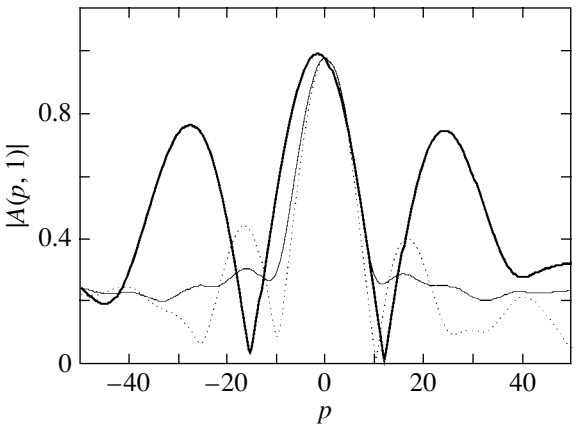

Fig. 2. Fourier decomposition of the distribution of 15 real OB associations into spiral harmonics (heavy line); the Fourier spectrum of one random distribution of 15 objects (dotted line), and the Fourier decomposition of the random distribution averaged over 100 samples (thin line).

of the central maximum depends on the size of the cluster: the smaller the clump, the wider the central maximum.

The dotted line in Fig. 2 indicates the Fourier decomposition for 15 objects randomly distributed in the 3 kpc solar neighborhood or, to be more precise, in the region where the circle $r = 3$ kpc and the ring $R_0 - 2 < R < R_0 + 2$ kpc intersect. We clearly see the maximum at $p = 0$ and the amplitude fluctuations on both sides of it. The thin line in Fig. 2 indicates the Fourier decomposition of a random distribution of 15 objects in the above solar neighborhood averaged over 100 samples. The Fourier spectrum of one random distribution agrees well with the mean spectrum in the central region ($p = 0$), where the amplitude fluctuations are small. The mean spectrum of the random distribution is a symmetric function relative to which we clearly see the central maximum of the Fourier decomposition of the real sample to be displaced toward the negative p, i.e., toward the leading waves. No random fluctuations can explain this displacement.

Let us assume the mean amplitude of the random distribution of 15 objects to be a background. We are interested in the difference $\Delta A(p, 1)$ between the Fourier amplitude for the real sample and the background. The heavy line in Fig. 3a indicates the absolute value of this difference $|\Delta A(p, 1)|$. We clearly see three maxima at $p = -28$, $p = +24$, and $p = -10$. The maximum at $p = -10$ points to the presence of a leading wave with a large interarm distance of $\lambda = 4.5 \pm 2.0$ kpc in the morphology of the Galactic spiral pattern.

The rms deviation of the Fourier amplitude of one random sample from the background is 0.12 and does

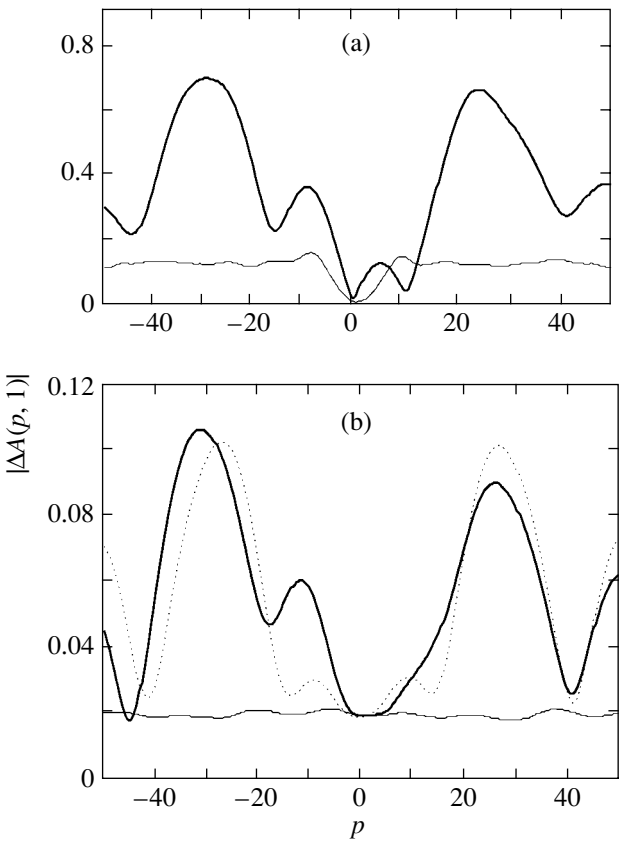

Fig. 3. (a) Absolute value of the difference between the Fourier amplitude calculated for the real distribution and the mean Fourier amplitude for a random distribution of 15 objects (heavy line); the rms deviation of the amplitude of a random sample from the background (thin line); we clearly see these three maxima at $p = -28$, $p = +24$, and $p = -10$. (b) The Fourier decomposition of the distribution of young objects in model 2 (heavy line); the Fourier decomposition for the fragments of an ideal spiral pattern (dotted line); the mean amplitude of the random distribution of young objects in the ring thin line; we clearly see three maxima at $p = -31$, $p = +26$, and $p = -12$.

not depend on p, except for the central region where it is close to zero (the thin line in Fig. 3a). The maxima at $p = -28$, $p = +24$, and $p = -10$ are not the result of random background fluctuations at the 99% confidence level.

Any Fourier decomposition contains high-order harmonics that, in our case, correspond to the increasingly tightly would spiral patterns at $p = 2p_0$, $3p_0$, $4p_0, \ldots$, where p_0 is the fundamental harmonic ($|p_0| = 26$). Our Fourier spectra also have high-order harmonics, but they are outside our figures.

It is interesting to note the causes of such deep and sharp minima in the Fourier decomposition of the real sample (Fig. 2). They correspond to a wave with an interarm distance ($|p| = 13$) that is twice the main tightly wound spiral pattern ($|p_0| = 26$). Since such a wave would inevitably arrive in opposite phases at the

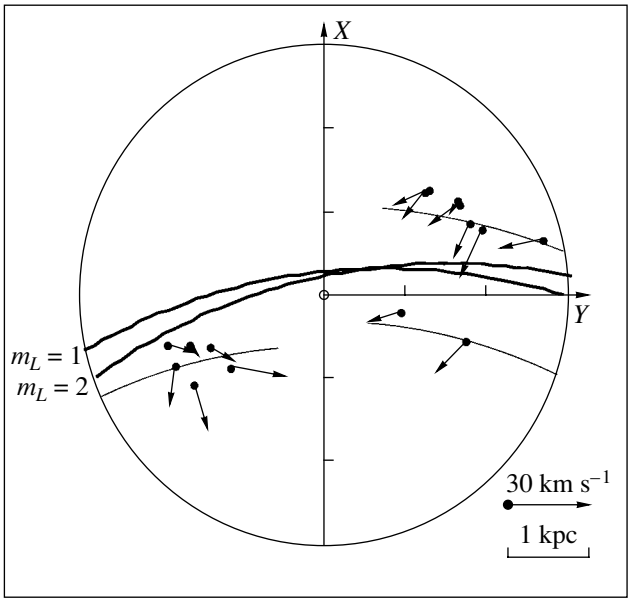

Fig. 4. Most probable locations of the leading wave with $\lambda = 4.5$ kpc and a pitch angle of $i = 6°$ and $i = 12°$ for the one-armed ($m_L = 1$) and two-armed ($m_L = 2$) models of the leading wave. In both cases, the leading wave in the solar neighborhood lies nearly halfway between the combined Carina–Cygnus and Perseus arm fragments.

Perseus arm and at the combined Carina–Cygnus arm fragment, it is absent in the spectrum.

The heavy line in Fig. 3b indicates the Fourier decomposition of the distribution of young objects in model 2. We clearly see three maxima at $p = -31$, $p = +26$, and $p = -12$ that correspond to a tightly wound spiral pattern with an interarm distance of $\lambda = 1.6 \pm 0.5$ kpc and a leading wave with $\lambda = 3.8 \pm 2.0$ kpc. No central maximum emerges in model 2, because any two halves of the Galaxy contain almost equal numbers of points. The scales of the vertical axes of models 1 and 2 differ by a factor of 10. However, we are interested not in the absolute values, but in the form of the Fourier decomposition. The Fourier decomposition of the random distribution of young objects throughout the ring consists of random amplitude fluctuations that do not exceed 0.06. The mean amplitude of these fluctuations is $|A(p, 1)| = 0.02$ (the thin line in Fig. 3b). None of the three maxima at $p = -31$, $p = +26$, and $p = -12$ is the result of random fluctuations in the distribution of young objects at the 99% confidence level.

To understand why the leading wave appears, let us consider the Fourier decomposition of an ideal spiral pattern in the solar neighborhood. The model of an ideal spiral pattern is a modification of model 2 (Fig. 1b). The difference is that objects within 3 kpc of the Sun concentrate toward two rather than three arm fragments that do not terminate anywhere within this region. The arms are in the shape of circular arcs and are located at the Galactocentric distances of the Carina ($R = 6.5$ kpc) and Perseus ($R = 8.2$ kpc) arms. The model is symmetric about the X-axis. Both arms contain equal numbers of objects.

The dotted line in Fig. 3b indicates the Fourier decomposition of an ideal spiral pattern. It exhibits two large maxima at $p = \pm 26$ and two barely visible, but unremovable maxima at $p = \pm 9$. The large maxima correspond to the main tightly wound spiral pattern, while the small maxima correspond to spiral waves with an interarm distance that is a factor of 3 larger than the distance between the Perseus and Carina arms. These waves emerge, since the circumference under consideration includes two arm fragments and the interarm space between them. Three halves of the main wave, $3\lambda_0/2$, can be covered by one half of the other wave, $\lambda_1/2$. This wave describes the behavior of all objects within 3 kpc of the Sun, without separating them between the arms, and its maximum must be located approximately halfway between the arms.

The detected leading wave with $\lambda = 4 \pm 2$ kpc is of the same nature. It describes the behavior of all objects within 3 kpc of the Sun. Figure 4 shows the most probable location of the leading arm. It has a pitch angle of $i = 6°$ and $i = 12°$ for the one-armed ($m_L = 1$) and two-armed ($m_L = 2$) models of the leading wave, respectively. In both cases, the leading arm intersects the X axis at a Galactocentric distance of $R = 7.4 \pm 0.5$ kpc (for the assumed Galactocentric distance of the Sun $R_0 = 7.1$ kpc); i.e., it lies exactly halfway between the combined Carina–Cygnus fragment and the Perseus arm.

Both defects of the spiral pattern—the displacement of the Carina and Cygnus arm fragments toward the leading spiral and the absence of the Perseus arm extension in the III quadrant—give rise to a leading wave. However, the termination of the Perseus arm makes a much larger contribution to the leading wave.

Both models yield similar results. However, the following trend clearly shows up in model 2. The leading wave tends to have an interarm distance that is twice λ of the tightly wound spiral pattern. This is because we actually have two fragments of the spiral pattern: the combined Carina–Cygnus fragment and the Perseus arm. In order to weaken the second fragment without weakening the first, the additional wave must have an interarm distance that is twice that of the main tightly wound spiral wave. To weaken the Perseus arm in the III quadrant without weakening it significantly in the II quadrant, the additional spiral wave must be a leading one.

Thus, the distribution of OB associations within 3 kpc of the Sun can be represented as a superposition

of two spiral components: a tightly wound spiral wave with an interarm distance of $\lambda = 1.8 \pm 0.4$ kpc and a leading arm with an interarm distance of $\lambda = 4 \pm 2$ kpc.

How can the detection of other more distant fragments of the tightly wound spiral pattern change the parameters of the leading wave? The leading wave proved to be most sensitive to the asymmetry of the new possible arm fragments about the X axis. The amplitude of the leading wave would increase only if, for example, the new distant fragment detected in the outer Galaxy were as asymmetric about the X axis as the Perseus arm (i.e., more objects would be located in the II quadrant than in the III quadrant; Fig. 1b). In contrast, in the inner Galaxy a distant fragment must contain more objects in the IV quadrant than in the I quadrant to amplify the leading wave. In general, the asymmetry in the distribution of young objects required to amplify the leading wave agrees with the asymmetry in the H I distribution in the Galaxy (Blitz and Spergel 1991).

HOW DOES EACH SPIRAL COMPONENT MANIFEST ITSELF IN THE KINEMATICS AND DISTRIBUTION OF YOUNG STARS?

While analyzing the locations of the spiral arm fragments identified by the kinematics of young stars, we implicitly assumed that the additional components of the spiral pattern would not disrupt the periodic pattern of the velocity field of young stars. The large interarm distance of the leading component agrees well with this assumption. Indeed, the velocity perturbation amplitudes f_R and f_θ for young stars must be proportional to λ^{-1} (Lin *et al.* 1969). Consequently, even if the other parameters of the spiral pattern (the perturbations of the potential and the locations with respect to the corotation radius) are equal, the velocity perturbation amplitudes for the leading wave must be a factor of 2 lower than those for the tightly wound wave. In general, the velocity perturbations for young stars can be explained without invoking the leading wave.

The tightly wound spiral wave was first found by analyzing the kinematics of young stars (Mel'nik *et al.* 1999, 2001). In the Fourier spectrum, it is represented by a superposition of leading and trailing spiral waves. However, the kinematics of young objects strongly suggests that the tightly wound spiral pattern is a trailing wave.

The sense of winding is determined by the following. The radial components of the mean residual velocities for the young stars that concentrate in the Cygnus and Perseus arms are directed toward the Galactic center, while their azimuthal components are opposite to the sense of Galactic rotation. Three conclusions can be drawn from this: First, the Cygnus and Perseus arm fragments represent a trailing spiral pattern. Second, the Cygnus and Perseus arm fragments are located within the corotation circle. Third, the coincidence of the minima in the distributions of radial and azimuthal residual velocities is indicative of the presence of a shock (see Mel'nik (2003) for more detail).

A problem arises with the Carina arm. We observe an enhanced concentration of young stars in all three arm fragments: the Perseus, Cygnus, and Carina arms. However, in the Carina arm, we find no significant variations in the azimuthal residual velocity across the arm, while the radial residual velocity exhibits a well-defined minimum (see Fig. 5 in Mel'nik *et al.* 2001). The absence of an azimuthal velocity gradient across the Carina arm may be attributable to the distance errors that can effectively blur the variations exactly in the azimuthal velocity (see Mel'nik (2003) for more detail). However, this defect can also have a different cause, one which is discussed in the next section.

The leading wave clearly shows up only in the relative location of the spiral arm fragments. Indeed, all three fragments of the Carina, Cygnus, and Perseus arms can be imagined as lying on a broad leading spiral arm. This distribution can stem from the fact that the star formation is more intense in the portions of the trailing spiral arms where they cross the crest of the leading wave. Shocks seem to be also present only in these arm portions. This behavior can be explained using the model of Roberts and Hausman (1984), in which the motion of particle clouds is considered in a perturbed potential. The enhanced surface density of the disk in these portions must cause additional crowding of the cloud orbits and increase the cloud–cloud collision frequency, which, in turn, can give rise to shocks.

Thus, the presence of a leading wave in the Galactic disk allows certain deviations from an ideal spiral pattern to be explained. The leading wave emerges mainly because the Perseus arm weakens in the III quadrant. The simplest explanation of the weakening of the Perseus arm consists in a decrease of the disk surface density in this region.

EVOLUTION OF THE GALACTIC SPIRAL PATTERN

Another peculiarity of the Galactic spiral pattern is the unusually small interarm distance of the trailing spiral wave ($\lambda = 1.8 \pm 0.4$ kpc), which is rarely observed in other galaxies. The tightly wound spiral pattern of our Galaxy may appear as a ring or part of it from a large distance.

The two peculiarities of the Galactic spiral pattern—the presence of shock and a tightly wound spiral pattern—force us to abandon the theory of modes, which is attractive in that it can ensure a quasi-steady state. The large energy losses in the shock require an efficient spiral wave amplification mechanism from the model to ensure a quasi-steady state. However, this mechanism (swing amplification) gives rise only to open spiral patterns (Toomre 1981; Athanossoula 1984). The observed tightly wound spiral pattern is probably not a mode and must evolve along the Galactic radius vector.

Toomre (1969) showed that over several galaxy rotations, the short trailing spiral wave displaces from the corotation region to the inner Lindblad resonance. During this displacement, the distance between the turns of the spiral wave decreases, while the density and velocity perturbations of the young stars remain high for a long period of time (Toomre 1969, 1977; Lin 1970). The trailing spiral wave observed in the Galaxy may be located near the inner Lindblad resonance. The unusually small interarm distance of the trailing wave can be explained by its evolution: the decrease in the interarm distance as the wave displaces toward the inner Lindblad resonance.

The Carina arm may be part of this resonance ring. First, we see no tightly wound spiral arms within the region bounded by the Carina arm. The kinematics of the Sagittarius arm differs markedly from that of the Perseus, Cygnus, and Carina arms (see Mel'nik *et al.* (2001) for more detail), and it cannot be considered to be a fragment of the same spiral wave. Second, the ring geometry of the Carina arm could in principle explain the absence of cross-arm variations in the azimuthal residual velocity.

The superposition of the trailing and leading spiral arms found in our Galaxy is not unique. The galaxy M 31 exhibits a similar pattern with the leading and trailing arms having interarm distances of 6 and 4 kpc, respectively (Considere and Athanossoula 1982). The main difference is that the interarm distance of the trailing wave in the Galaxy is a factor of about 2 smaller. In addition, the leading wave in the Andromeda galaxy is known to be one-armed. No such information is available for our Galaxy.

CONCLUSIONS

The spiral pattern of the Galaxy identified by the kinematics of young stars within 3 kpc of the Sun was Fourier decomposed into spiral harmonics. We showed that the spiral pattern could be represented as a superposition of trailing and leading waves with interarm distances of $\lambda = 1.8 \pm 0.4$ and 4 ± 2 kpc, respectively.

The presence of a leading wave in the Galactic disk makes it possible to explain certain deviations from an ideal spiral pattern. The leading wave clearly shows up only in the large-scale distribution of young objects and has virtually no effect on their kinematics. Shocks seem to exist only in the portions of the trailing spiral pattern where it intersects the crest of the leading wave. An enhanced surface density of the disk in these portions must cause additional crowding of the cloud orbits and increase the cloud–cloud collision frequency, which, in turn, can give rise to shocks (Roberts and Hausman 1984).

The small interarm distance of the trailing spiral wave ($\lambda = 1.8$ kpc) can be explained by its evolution: the decrease in the interarm distance as the wave displaces toward the inner Lindblad resonance. The Carina arm may be part of this resonance ring. It may well be that there is a spiral pattern in the region bounded by the Carina arm, but this is a different spiral pattern.

The leading wave in our Galaxy could be regenerating the trailing spiral pattern via the swing amplification mechanism (Goldreich and Lynden-Bell 1965; Julian and Toomre 1966; Toomre 1981). However, it remains unclear why it emerges.

ACKNOWLEDGMENTS

I am grateful to A.V. Zasov, I.I. Pasha, A.S. Rastorgouev, Yu.N. Efremov, and A.K. Dambis for interesting discussions and useful remarks. This work was supported by the Russian Foundation for Basic Research (project nos. 02-02-16677 and 03-02-16288), the Council for the Program of Support for Leading Scientific Schools (project no. NSh.389.2003.2), and the State Science and Technology Astronomy Program.

REFERENCES

1. E. Athanassoula, Phys. Rep. **114**, 319 (1984).
2. C. Blaha and R. M. Humphreys, Astron. J. **98**, 1598 (1989).
3. L. Blitz and D. N. Spergel, Astrophys. J. **370**, 205 (1991).
4. S. Considere and E. Athanassoula, Astron. Astrophys. **111**, 28 (1982).
5. A. K. Dambis, A. M. Mel'nik, and A. S. Rastorguev, Pis'ma Astron. Zh. **21**, 331 (1995) [Astron. Lett. **21**, 291 (1995)].
6. A. K. Dambis, A. M. Mel'nik, and A. S. Rastorguev, Pis'ma Astron. Zh. **27**, 68 (2001) [Astron. Lett. **27**, 58 (2001)].
7. E. V. Glushkova, A. K. Dambis, A. M. Mel'nik, and A. S. Rastorguev, Astron. Astrophys. **329**, 514 (1998).
8. P. Goldreich and D. Lynden-Bell, Mon. Not. R. Astron. Soc. **130**, 125 (1965).

9. W. H. Julian and A. Toomre, Astrophys. J. **146**, 810 (1966).
10. A. J. Kalnajs, *La Dynamique des Galaxies Spirales, Coll. Int. CNRS No. 241*, Ed. by L. Weliachew (Editions du Centre National de la Recherche Scientifique, Paris, 1975), p. 103.
11. C. C. Lin, *The Spiral Structure of Our Galaxy, IAU Symp. 38*, Ed. by W. Becker and G. Contopoulos (Reidel, Dordrecht, 1970), p. 377.
12. C. C. Lin, C. Yuan, and F. H. Shu, Astrophys. J. **155**, 721 (1969).
13. A. M. Mel'nik, Pis'ma Astron. Zh. **29**, 349 (2003) [Astron. Lett. **29**, 304 (2003)].
14. A. M. Mel'nik, A. K. Dambis, and A. S. Rastorguev, Pis'ma Astron. Zh. **25**, 602 (1999) [Astron. Lett. **25**, 518 (1999)].
15. A. M. Mel'nik, A. K. Dambis, and A. S. Rastorguev, Pis'ma Astron. Zh. **27**, 611 (2001) [Astron. Lett. **27**, 521 (2001)].
16. W. W. Roberts and M. A. Hausman, Astrophys. J. **277**, 744 (1984).
17. T. G. Sitnik and A. M. Mel'nik, Pis'ma Astron. Zh. **22**, 471 (1996) [Astron. Lett. **22**, 422 (1996)].
18. A. Toomre, Astrophys. **158**, 899 (1969).
19. A. Toomre, Annu. Rev. Astron. Astrophys. **15**, 437 (1977).
20. A. Toomre, *The Structure and Evolution of Normal Galaxies*, Ed. by S. M. Fall and D. Lynden-Bell (Cambridge Univ. Press, Cambridge, 1981), p. 111.

Translated by V. Astakhov

Astronomy Letters, Vol. 31, No. 2, 2005, pp. 88–97. Translated from Pis'ma v Astronomicheskiĭ Zhurnal, Vol. 31, No. 2, 2005, pp. 99–109.

Observations of the Transient X-ray Pulsar KS 1947+300 by the INTEGRAL and RXTE Observatories

S. S. Tsygankov* **and A. A. Lutovinov**

Space Research Institute, Russian Academy of Sciences, Profsoyuznaya ul. 84/32, Moscow, 117810 Russia

Received August 19, 2004

Abstract—We analyze the observations of the X-ray pulsar KS 1947+300 performed by the INTEGRAL and RXTE observatories over a wide (3–100 keV) X-ray energy range. The shape of the pulse profile was found to depend on the luminosity of the source. Based on the model of a magnetized neutron star, we study the characteristics of the pulsar using the change in its spin-up rate. We estimated the magnetic field strength of the pulsar and the distance to the binary. © *2005 Pleiades Publishing, Inc.*

Key words: *pulsars, neutron stars, X-ray sources.*

INTRODUCTION

The transient X-ray source KS 1947+300 was discovered in June 1989 during the observations of the Cyg X-1 region by the TTM telescope aboard the Kvant module of the Mir space station (Borozdin *et al.* 1990). The flux recorded from it was 70 ± 10 mCrab in the energy range 2–27 keV, and the spectrum was fitted by a power law with an index of $\gamma = -1.72 \pm 0.31$ and low-energy photoabsorption with an atomic hydrogen column density of $N_{\rm H} = (3.4 \pm 3.0) \times 10^{22}$ cm^{-2}. In April 1994, the BATSE monitor of the ComptonGRO observatory discovered the X-ray pulsar GRO J1948+32 with a period of 18.7 s in the same region of the sky. The spectrum of this source in the energy range 20–120 keV was described by a power law with a photon index of $\gamma = 2.65 \pm 0.15$ (Chakrabarty *et al.* 1995). Subsequently, KS 1947+300 and GRO J1948+32 were found to be the same object, a transient X-ray pulsar (Swank and Morgan 2000).

Until recently, no abrupt changes in pulsation period (so-called glitches) were known in accreting X-ray pulsars. However, having analyzed the RXTE data, Galloway *et al.* (2004) pointed out that the pulsation period of KS 1947+300 changes over a very short time. Thus, in January 2001, its pulsation frequency increased by about 1.8×10^{-6} Hz in less than 10 h (the rate of change is $\dot{f} \approx 5 \times 10^{-11}$ Hz s^{-1}), while the X-ray flux exhibited no significant increase. The fractional change in frequency in this case was $\Delta\nu/\nu = 3.7 \times 10^{-5}$, much greater than that observed during glitches in radio pulsars (Krawczyk *et al.* 2003) and anomalous X-ray pulsars (Kaspi and Gavriil 2003). At the same time, a comparison with the BATSE data reveals a spin-down of the pulsar at a mean rate of $\dot{f} \approx -8 \times 10^{-13}$ Hz s^{-1} on a time scale of several years. Based on the behavior of the pulsation period during the outburst of 2000–2001, Galloway *et al.* (2004) determined the parameters of the binary: the orbital period $P_{\rm orb} = 40\overset{\rm d}{.}415 \pm 0\overset{\rm d}{.}010$, the projected semimajor axis of the relativistic object $a_x \sin i = 137 \pm 3$ light seconds, and the eccentricity $e = 0.033 \pm 0.013$.

The optical counterpart in the binary is a B0 Ve star. If the true luminosity of the star is typical of stars of this spectral type, then the distance to it is estimated as ~10 kpc (Negueruela *et al.* 2003).

In this paper, we present the results of our spectral and timing analyses of the pulsar KS1947+300 based on INTEGRAL and RXTE data in a wide (3–100 keV) energy range.

OBSERVATIONS

The INTEGRAL International observatory (Winkler *et al.* 2003) placed in orbit by a Russian Proton launcher on October 17, 2002, carries four scientific instruments that allow the emission from astrophysical objects to be studied over a wide wavelength range (from optical to hard γ rays). We used mainly data from the ISGRI detector of the IBIS gamma-ray telescope (Ubertini *et al.* 2003), which includes two layers of position-sensitive detectors (ISGRI and PICsIT) and a coded mask. The ISGRI detector is effectively sensitive to photons in the energy range 20 to 200 keV (the energy resolution is ~7% at 100 keV) and can image a sky region within a $29^\circ \times 29^\circ$ field of

*E-mail: st@hea.iki.rssi.ru

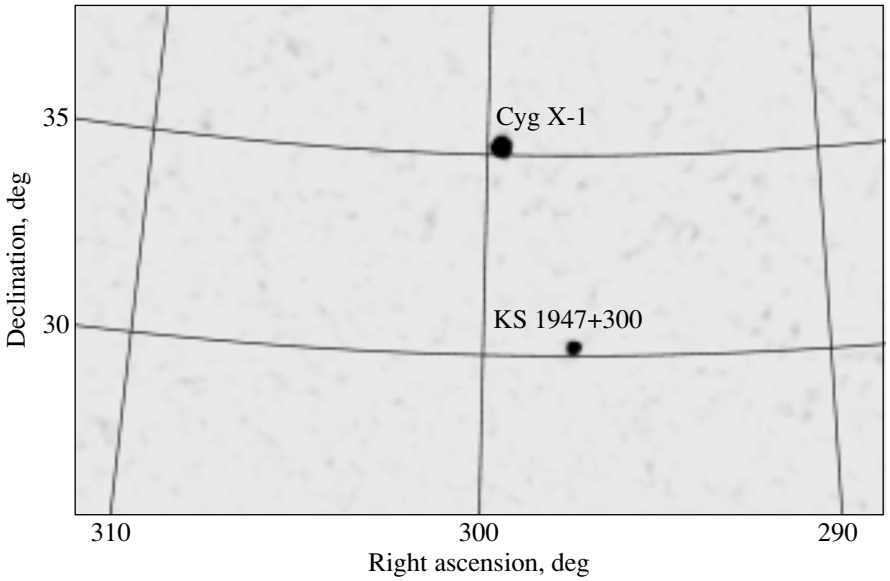

Fig. 1. Sky map with KS 1947+300 obtained by the IBIS telescope in the energy range 18–60 keV. The total exposure time was about 6 ks.

view (the full coding zone is $9° \times 9°$) with a nominal spatial resolution of ~12 arcmin (the angular size of the mask element). See Lebrun *et al.* (2003) for a more detailed description of the detector.

The X-ray pulsar KS 1947+300 occasionally falls within the field of view of the scientific instruments when the Galactic plane is scanned as part of the INTEGRAL Main Observing Program. In this paper, we analyze the INTEGRAL observations performed from December 2002 through April 2004. About 700 pointings were made over this period in which the object under study fell within the field of view of the INTEGRAL instruments; the total exposure time was $\sim 1.5 \times 10^6$ s.

We performed the image reconstruction and spectral analysis of the IBIS data using the methods described by Revnivtsev *et al.* (2004) and Lutovinov *et al.* (2003). An analysis of the large set of calibration observations for the Crab Nebula revealed a systematic error of ~10% in the measured absolute flux from the source over a wide energy range; the spectral shape was reconstructed with an accuracy as high as 3–5%. This was taken into account in the spectral analysis by adding a systematic error of 5%. All of the errors given in this paper are purely statistical and correspond to one standard deviation. The standard OSA software of version 3.0 was used for our timing analysis of the source on time scales of the pulsation period and for our spectral analysis of the JEM-X data.

Figure 1 shows the sky map with the X-ray pulsar KS 1947+300 obtained by the IBIS telescope in the energy range 18–60 keV. This map was constructed when the Galactic plane was scanned on May 11, 2003 (MJD 52770). The detection significance of the source was 29σ at a total exposure of ~6 ks.

Since the object under study was not within the field of view of the JEM-X X-ray monitor (Lund *et al.* 2003) aboard the INTEGRAL observatory in the overwhelming majority of the cases, we failed to analyze its behavior in the standard X-ray energy range. Therefore, we used simultaneous data from the ASM monitor of the RXTE observatory (http://xte.mit.edu/ASM_lc.html) to make up for the lack of information in this range (1.3–12.2 keV). In addition, based on publicly available RXTE data, we traced the evolution of the emission from the source over a wide energy range during one of its previous outbursts in 2000–2001 (Obs. ID 50068, 50425, and 60402). The main instruments of the RXTE observatory (Bradt *et al.* 1993) are the PCA and HEXTE spectrometers with the operating energy ranges 3–20 and 15–250 keV, respectively. The PCA spectrometer is a system of five xenon/propane proportional counters with an effective area of ~ 6400 cm^2 at 6–7 keV; its energy resolution at these energies is ~18%. The HEXTE spectrometer is a system of two independent packages of NaI(Tl)/CsI(Na) phoswich detectors swinging with an interval of 16 s for the observations of background areas at a distance of 1°.5 from the source. At each specific time, the source can be observed only by one of the two detector packages; thus, the effective area of the HEXTE detectors is ~700 cm^2.

The standard FTOOLS/LHEASOFT 5.3 software package was used to process the RXTE data.

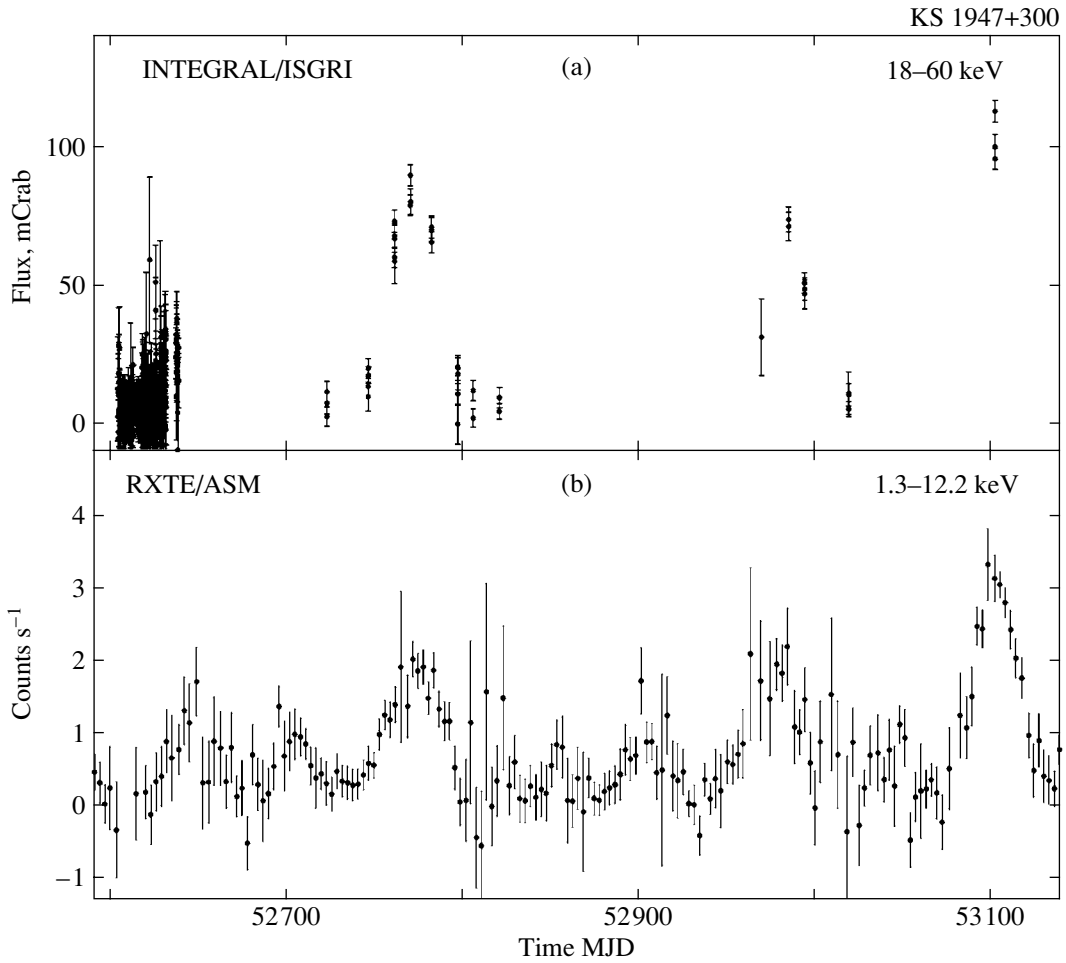

Fig. 2. Light curves for the pulsar KS 1947+300 in the energy ranges (a) 18–60 and (b) 1.3–12.2 keV. The errors correspond to one standard deviation.

TIMING ANALYSIS

As was mentioned above, the source KS 1947+300 exhibits strong outburst activity. Figure 2 shows its light curve in the energy range 18–60 keV constructed from the IBIS/INTEGRAL data in 2002–2004 (Fig. 2a) and the corresponding light curve in the energy range 1.3–12.2 keV constructed from the ASM/RXTE data (Fig. 2b).

As we see from the light curve, the source was in a low state during the first series of INTEGRAL observations in December 2002 (MJD 52600–52650); its intensity was ∼4.5 mCrab in the energy range 18–60 keV. At the end of this period, the flux from the source began to increase and reached ∼30 mCrab, but we failed to observe the outburst in full.

During the subsequent observations, the pulsar KS 1947+300 was within the IBIS field of view much more rarely, which, however, allowed several intense outbursts to be detected from it. The first began in mid-April 2003 (MJD 52750) and lasted about 50 days, and the peak flux from the source was about 80 mCrab in the energy range 18–60 keV. Subsequently, we detected two more outbursts from this object in December 2003 and April 2004 with peak fluxes of ∼70 (MJD 52985) and ∼100 (MJD 53102) mCrab in the energy range 18–60 keV, respectively. Figure 2 shows a clear correlation between the hard and soft X-ray fluxes from the source.

Table 1 gives the fluxes from the pulsar KS 1947+300 measured in the energy range 18–60 keV, the orbital phases during the observations under consideration calculated using $T_{\pi/2} =$ 51 985.31 MJD from Galloway *et al.* (2004), and its pulsation periods determined by an epoch-folding technique after the photon arrival times were corrected for the motion of the Earth, the spacecraft, and the neutron star in the binary. As we see from Table. 1, the pulsation frequency of the source near the peak of the April 2003 (MJD 52760–52780) outburst is proportional to the flux from it. Since the observational data and the statistics are scarce

Table 1. IBIS observations[a] of the pulsar KS 1947+300

Time of observations, MJD	Orbital phase	Flux, mCrab	Period, s
52605–52615	0.33–0.58	4.5 ± 0.3	18.669 ± 0.001
52723	0.25	6.9 ± 2.1	–[b]
52746	0.82	12.1 ± 2.3	–[b]
52761	0.19	64.0 ± 2.8	18.721 ± 0.005
52770	0.42	77.8 ± 2.7	18.718 ± 0.002
52782	0.71	67.8 ± 2.3	18.721 ± 0.002
52797	0.08	15.3 ± 2.0	–[b]
52806	0.31	6.3 ± 2.5	–[b]
52821	0.68	7.7 ± 2.3	–[b]
52970	0.36	31.0 ± 13.9	–[b]
52985	0.74	69.8 ± 3.4	18.727 ± 0.002
52994	0.96	47.5 ± 2.4	18.725 ± 0.002
53019	0.58	6.3 ± 2.1	–[b]
53102	0.65	96.1 ± 2.9	18.730 ± 0.002

[a] In the energy range 18–60 keV.
[b] Cannot be determined due to poor statistics.

(see, e.g., the measurements of the pulsation period during the December 2003 outburst), the significance of this result is low. However, it agrees with the ComptonGRO and RXTE measurements of the pulsation period during previous outbursts.

An analysis of the emission from X-ray pulsars indicates that their pulse profiles can depend strongly on the energy and intensity of the source (see, e.g., White *et al.* 1983; Nagase 1989; Lutovinov *et al.* 1994; and references therein). We studied the behavior of the pulse profile and the pulse fraction for KS 1947+300 as a function of its state. Figure 3 shows the phase light curves for the pulsar obtained from the IBIS/INTEGRAL data and averaged at different intensities: the flux from the source in the energy range 18–60 keV is (a) $F \approx 78$ mCrab (MJD 52770), (b) $F \approx 48$ mCrab (MJD 52994), and (c) $F \approx 5$ mCrab (MJD 52605–52615). In the first case, the pulse profile is a single broad peak whose intensity decreases insignificantly with increasing phase. A finer profile structure (separation into several individual peaks) begins to show up as the intensity of the source decreases. During the observations on April 7, 2004 (MJD 53102), when the peak flux from the source in the energy range 18–60 keV was about 96 mCrab, the pulse profile had a shape identical to that shown in Fig. 3a.

For the subsequent analysis of the results obtained and their comparison with theoretical models, we should pass from fluxes to luminosities over a wide energy range. However, in most cases, this is difficult to do, because we have only hard X-ray data at our disposal. Therefore, to roughly estimate the bolometric luminosity of the pulsar during the INTEGRAL observations of the April–May 2003 outburst, we used the following method: assuming the main energy release to be in the energy range 2–100 keV and the distance to the object to be $d = 10$ kpc, we determined its bolometric luminosity during the observations on April 7, 2004, when the source under study was also within the JEM-X field of view. The luminosity of the object can then be estimated from simple proportionality considerations by comparing the IBIS hard X-ray fluxes at this point and the point of interest. However, it should be understood that this estimate is valid only if the spectral shape is constant at the two points being compared. Thus, the pulse profiles shown in Fig. 3 correspond to the following approximate bolometric luminosities of the source: (a) 2.5×10^{37}, (b) 1.5×10^{37}, and (c) 0.2×10^{37} erg s^{-1}, respectively.

For comparison, Fig. 4 shows the HEXTE/RXTE pulse profiles for KS 1947+300 in the energy range 18–60 keV. The observations were performed during the outburst of the source under study that be-

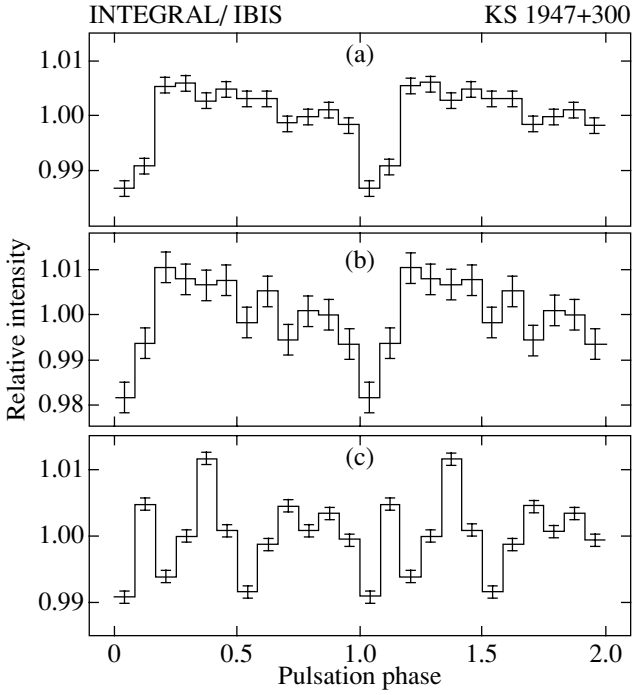

Fig. 3. IBIS pulse profiles for KS 1947+300 at different intensities; the mean bolometric luminosity of the source is (a) 2.5×10^{37} (MJD 52770), (b) 1.5×10^{37} (MJD 52994), and (c) 0.2×10^{37} erg s^{-1} (MJD 52605–52615).

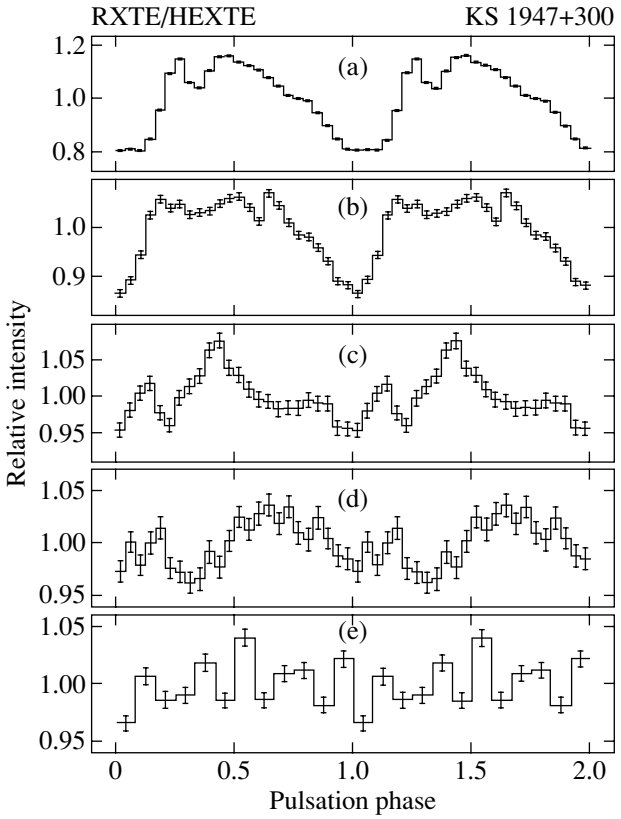

Fig. 4. HEXTE pulse profiles for KS 1947+300 at different intensities during the outburst of 2000–2001 (the background was not subtracted). The mean bolometric luminosity of the source is (a) 10.6×10^{37}, (b) 5.4×10^{37}, (c) 3.4×10^{37}, (d) 0.9×10^{37}, and (e) 0.3×10^{37} erg s^{-1}.

gan in December 2000. Each panel of this figure corresponds to the source's mean bolometric luminosities of (a) 10.6×10^{37}, (b) 5.4×10^{37}, (c) 3.4×10^{37}, (d) 0.9×10^{37}, and (e) 0.3×10^{37} erg s^{-1}. A significant difference between this outburst and the outbursts detected by the INTEGRAL observatory is a factor of ~3 longer duration and a factor of ~4 higher intensity. Nevertheless, the behavior of the pulse profiles in this case is similar to that observed by INTEGRAL (Fig. 3). In the brightest state, the pulse profile is a single broad peak with its separation into two subpeaks at the vertex, one of which is much narrower than the other; the intensity of the profile decreases with increasing phase. As the luminosity of the source decreases, the separation into several subpeaks becomes increasingly distinct. When the luminosity of the object reaches 0.9×10^{37} erg s^{-1}, the profile again becomes double peaked, with the mean peak shifting backward by approximately a quarter of the phase. This behavior of the profile may be attributable to different emission regimes, depending on the source's luminosity (Basko and Sunyaev 1976). The PCA/RXTE data in the softer energy range also reveal such a dependence of the pulse shape on the source's intensity, but it is not so distinct (see Fig. 3 from Galloway *et al.* 2004).

Figure 5 shows how the pulse profile for the object under study changes with energy range. Figures 5a and 5b present the phase light curves obtained from the PCA/RXTE observations on February 10, 2001 (MJD 51950); Fig. 5c shows the same light curves obtained from the HEXTE data averaged over the period during which the source was near maximum light (MJD 51941–51959). The relative intensity of the first peak increases with energy, but no significant changes in the shape were found.

Since the background cannot be properly determined at this time, we were unable to analyze the behavior of the pulse fraction using the IBIS/INTEGRAL data. Therefore, we used data from the HEXTE and PCA spectrometers of the RXTE observatory for such an analysis. In Fig. 6a, the pulse fraction, which is defined as $P = (I_{\max} - I_{\min})/(I_{\max} + I_{\min})$, where $I_{\max}$ and $I_{\min}$ are the background-corrected count rates at the maximum and minimum of the pulse profile, is plotted against orbital phase; this dependence was obtained from the

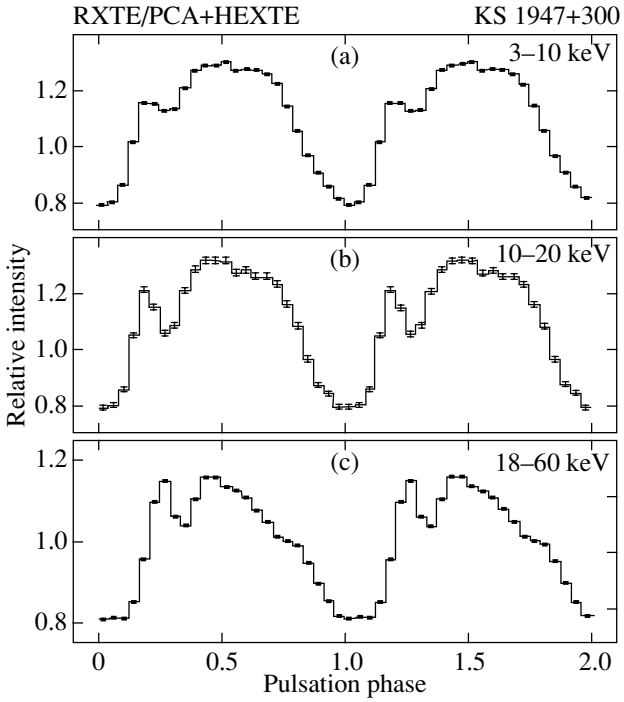

Fig. 5. RXTE pulse profiles for KS 1947+300 in different energy ranges. The errors correspond to one standard deviation.

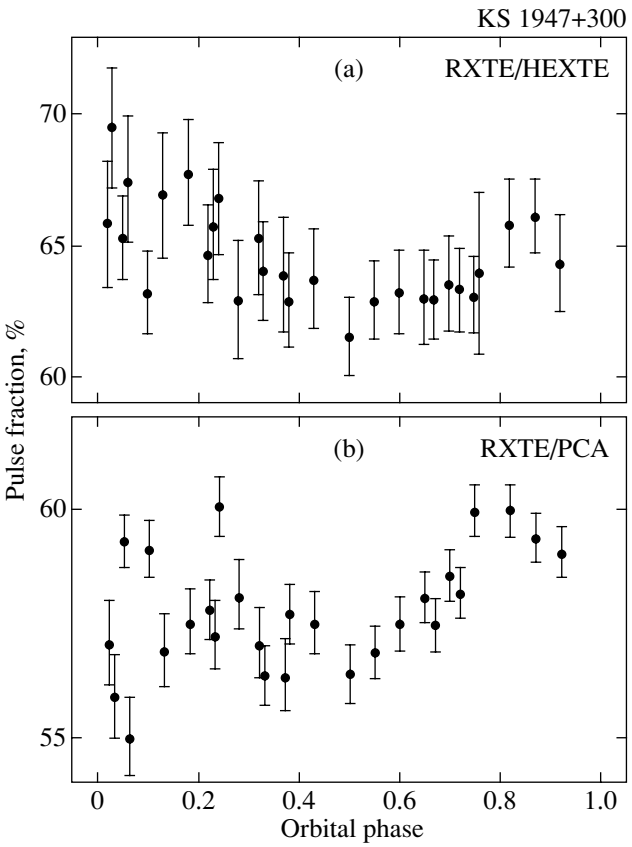

Fig. 6. Pulse fraction in the energy range 18–60 keV versus orbital phase of the pulsar KS 1947+300 during the 2000–2001 outburst, as derived from the HEXTE/RXTE data (a), and in the energy range 3–20 keV, as derived from the PCA/RXTE data (b).

HEXTE data in the energy range 18–60 keV near the peak of the 2000–2001 outburst. We see that there is a minimum near a phase of ∼0.5. A similar, but slightly less distinct dependence is also typical of the PCA data in the energy range 3–20 keV (Fig. 6b). The small scatter of data points in pulse fraction at close orbit phases is attributable to the dependence of this parameter on the source's intensity.

SPECTRAL ANALYSIS

As we showed in the previous section, the source KS 1947+300 exhibits a luminosity dependence of the pulse profile during X-ray outbursts. Therefore, it is of particular interest to study the spectral behavior of the object as a function of the outburst phase.

In the standard X-ray energy range, the pulsar KS 1947+300 was recorded at a statistically significant level by the JEM-X telescope of the INTEGRAL observatory only once, during the observations on April 7, 2004, when its bolometric luminosity was $L_x \simeq 3.1 \times 10^{37}$ erg s^{-1}. The spectrum of the source over a wide energy range is well described by a typical (for this class of objects) model that includes a simple power law with an exponential cutoff at high energies:

$$I(E) = AE^{-\alpha} \times \begin{cases} 1, & \text{if} \quad E < E_c \\ \exp\left[-(E - E_c)/E_f\right], & \text{if} \quad E \geq E_c, \end{cases} \qquad (1)$$

where E is the photon energy in keV, A is the normalization of the power-law component, α is the photon spectral index, E_c is the cutoff energy, and E_f is the e-folding energy in the source's spectrum. This model has long and widely been used to fit the spectra of X-ray pulsars (White *et al.* 1983). The energy spectrum of KS 1947+300 reconstructed from the JEM-X and IBIS data is shown in Fig. 7, and its best-fit parameters are given in Table 2.

During the remaining INTEGRAL observations, the pulsar was recorded at a statistically significant level only by the ISGRI detector of the IBIS telescope, and its spectrum could be reconstructed at energies above 18 keV. When the spectra of the source in these sessions were described by the bremsstrahlung model in all three cases (where the spectrum could be reconstructed), its temperature remained approximately the same, within the error limits, and equal to $kT \sim 33$ keV. Table 2 gives the best-fit parameters for the same spectra based on the model that was used above to describe the

Table 2. Best-fit parameters for the spectrum of KS 1947+300[a]

Date	α	$E_{\rm Fe}$,[b] keV	$E_{\rm c}$, keV	$E_{\rm f}$, keV	$\chi^2_N(N)$[c]
Based on INTEGRAL (IBIS) data					
MJD 52605–52630	1.07[d]	–	8.6[d]	26.4 ± 2.7	2.91(7)
MJD 52770	1.07[d]	–	8.6[d]	24.7 ± 1.9	2.30(7)
MJD 52985	1.07[d]	–	8.6[d]	26.5 ± 3.4	0.66(7)
Based on INTEGRAL (JEM-X + IBIS) data					
MJD 53102	$1.07^{+0.24}_{-0.13}$	–	$8.6^{+3.4}_{-1.2}$	$23.6^{+5.3}_{-2.3}$	1.18(104)
Based on RXTE (PCA + HEXTE) data					
February 2001	1.38 ± 0.01	6.47 ± 0.07	15.8 ± 0.5	34.2 ± 0.7	1.33(98)
March 2001	1.26 ± 0.01	6.55 ± 0.08	12.5 ± 0.5	28.5 ± 0.4	1.34(112)
April 2001	1.13 ± 0.02	6.34 ± 0.09	11.4 ± 0.4	25.4 ± 0.7	0.99(117)
May 2001	0.82 ± 0.08	6.65 ± 0.11	6.5 ± 0.5	18.5 ± 1.4	1.03(117)
June 2001[e]	0.84 ± 0.24	–	5.7 ± 1.2	11.6 ± 3.3	0.63(35)

[a] All errors are given at the 1σ level.
[b] The position of the line center.
[c] The χ^2 value normalized to the number of degrees of freedom N.
[d] The parameters are fixed.
[e] Based only on PCA (3–20 keV) data.

broad-band spectrum, but we fixed the parameters whose values were outside the ISGRI energy range at the values that we obtained when analyzing the spectrum measured on April 7, 2004. We see that the e-folding energy in the source's spectrum $E_{\rm f}$ (which is determined in this approach) remains almost constant. The relatively large χ^2 value for some of the spectra is attributable to the poor statistics in these observations.

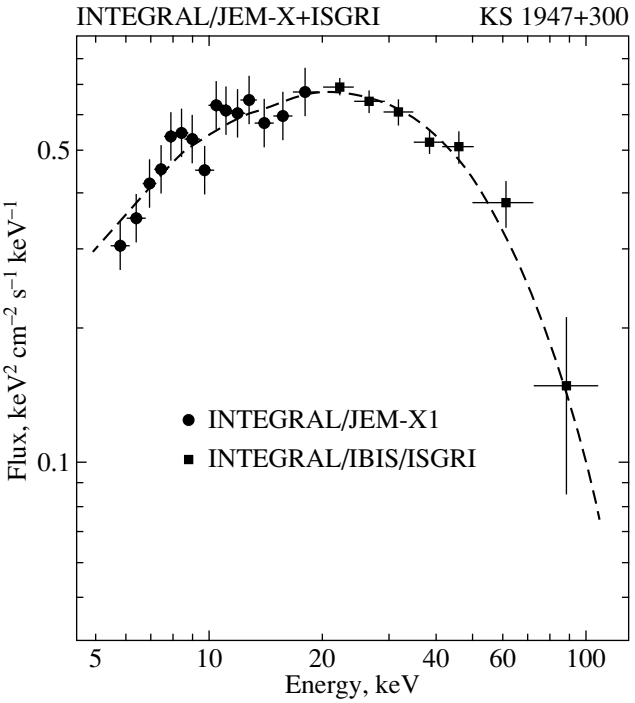

Fig. 7. Energy spectrum for KS 1947+300, as constructed from the observations by the JEM-X and IBIS telescopes aboard INTEGRAL on April 7, 2004. The dashed line indicates the best fit to the spectrum.

We used the RXTE data obtained during the 2000–2001 outburst to analyze the spectral behavior of the source over a wide energy range in mode detail. Figure 8 shows the energy spectra averaged over the same periods as those in which the pulse profiles were obtained (i.e., February, March, April, and May 2001, respectively); in June, the luminosity of the source was too low to reconstruct its spectrum from the HEXTE data, and only its soft part derived from the PCA data is shown in the figure. We used the PCA and HEXTE data for the energy ranges 4–20 and 20–100 keV, respectively. The RXTE data revealed a feature in the source's spectrum related to the emission line of neutral iron ($\sim$6.4 keV). The best-fit parameters for the pulsar's spectra in different states are given in Table 2. Interestingly, as the intensity of the source decreases, its spectrum becomes slightly harder, while the characteristic energies $E_{\rm c}$ and $E_{\rm f}$ decrease (for the observations in June 2001, the fit is based only on the PCA data). A comparison of the data from the two observatories shows that the best-fit parameters for the INTEGRAL data obtained in April 2004 also fall on this dependence.

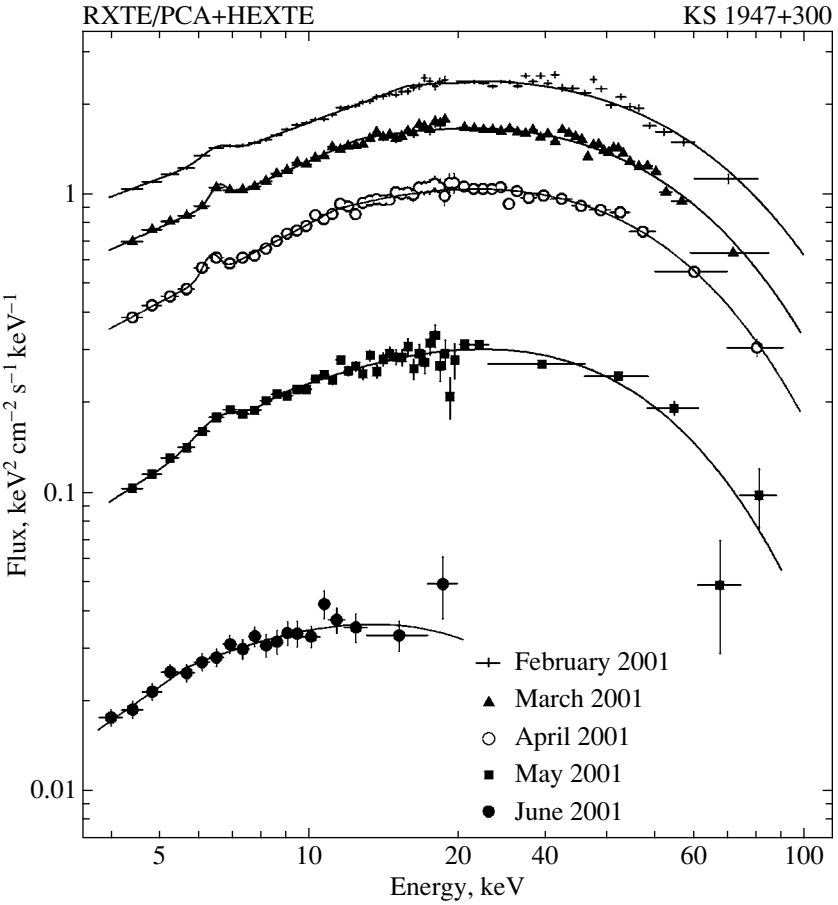

Fig. 8. Energy spectra for KS 1947+300 at different luminosities during the 2000–2001 outburst, as constructed from the RXTE data. The solid lines represent a power-law fit to the spectrum with a high-energy cutoff.

DISCUSSION

Evolution of the Pulse Profile

Basko and Sunyaev (1976) showed the existence of a critical luminosity L^* ($\sim 10^{37}$ erg s^{-1}) that separates two accretion regimes: the regime in which the effect of radiation on the falling matter may be disregarded and the regime in which this effect is significant. For $L < L^*$, the free-fall zone extends almost to the neutron-star surface, and the polar cap radiates mainly upward. In the opposite case ($L > L^*$), accretion columns that are elongated along the magnetic field lines and that radiate predominantly sideways are formed at the poles.

Based on this model, Parmar *et al.* (1989) first explained the luminosity dependence of the pulse profile for the transient X-ray pulsar EXO 2030+375. These authors modeled the pulse profile using a simple geometric model where the radiation is emitted from the magnetic poles of a rotating neutron star displaced from its spin axis. The study was carried out over a wide luminosity range: from 10^{36} to 10^{38} erg s^{-1}. It was pointed out that the upward-directed radiation becomes dominant as the source's luminosity decreases.

For the pulsar KS 1947+300, the behavior of its pulse shape is similar to that described above. For our analysis, we took the IBIS and HEXTE data for two different outbursts with luminosity ranges $(0.2–2.5) \times 10^{37}$ and $(0.3–10.6) \times 10^{37}$ erg s^{-1}, respectively. We consider the pulse profiles in the hard energy ranges due to their relative independence of external factors, in particular, the weaker dependence of the shape on the absorption far from the stellar surface. In both series of observations, the luminosity passes through its critical value of L^*, which is reflected in the change of the pulse profile shape (see Figs. 3 and 4). At high luminosities (i.e., during the formation of accretion columns), one might expect the spectrum to be softer than that in the low state, as confirmed by our spectral analysis.

The Cyclotron Lines and the Magnetic Field

In searching for features in the source's spectrum related to the resonance cyclotron absorption line, we

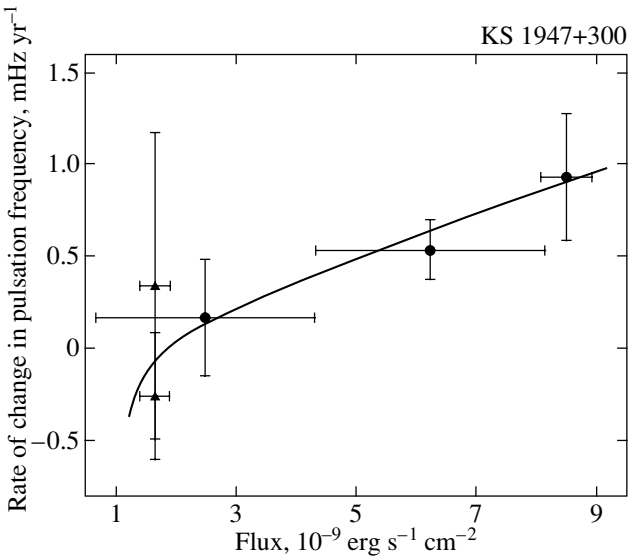

Fig. 9. Luminosity dependence of the rate of change in the pulsation frequency of KS 1947+300, as derived from the INTEGRAL (triangles) and RXTE (circles) data. The solid line indicates the model dependence for a distance to the binary of $d \sim 9.5$ kpc and a magnetic field of $B \sim 2.5 \times 10^{13}$ G.

added the corresponding component to the model fit in our spectral analysis. The energy of the line center $E_{\rm cyc}$ was varied over the range 5–90 keV at a 5-keV step, and its width was fixed at 5 keV. Using the $\Delta\chi^2$ test, we found the most probable position of the possible cyclotron line at an energy of about 70 keV, but the significance of this feature does not exceed $\sim 2\sigma$. Thus, we can at present conclude that either the sensitivity and effective exposure time of the modern INTEGRAL and RXTE instruments are not enough to detect the cyclotron line in the spectrum of KS 1947+300 or it lies outside the energy range 5–100 keV. If the latter is true, then the surface magnetic field of the neutron star must be either $<5.6 \times 10^{11}$ or $>10^{13}$ G.

Evolution of the Pulsation Period

During outbursts in X-ray pulsars, the rate of accretion onto the neutron star increases significantly. In this case, a spin-up of the pulsar attributable to the increase in the amount of angular momentum transferred by the accreted matter to the neutron star can be observed, with the magnetic field strength of the neutron star playing an important role.

A correlation between the rate of change in the pulse period and the X-ray luminosity during outbursts has now been found for seven transient sources (Galloway *et al.* 2004; Baykal *et al.* 2002, and references therein). As was noted above, during one of the outbursts observed by INTEGRAL (April 2003), there is a direct correlation between the flux from the source and its pulsation frequency similar to that observed by RXTE during the 2000–2001 outburst.

Based on the observed parameters of the pulsar KS 1947+300 during its outbursts, we can attempt to estimate its magnetic field strength and the distance to the binary using the model of a magnetized neutron star (Ghosh and Lamb 1979). The following relation must hold in the case of accretion from the disk:

$$\dot{\nu} \propto \mu^{2/7} n(\omega_s) L^{6/7} = \mu^{2/7} n(\omega_s) (4\pi d^2 F)^{6/7}, \quad (2)$$

where μ is the magnetic moment of the neutron star with a magnetic field B and radius R, $n(\omega_s)$ is a dimensionless function that depends on the fastness parameter ω_s, d is the distance to the binary, and F is the X-ray flux from it.

In Fig. 9, the rate of change in the pulsation frequency is plotted against the flux recorded from KS 1947+300. The circles in the figure correspond to the measured spin-up and spin-down rates of the pulsar near the peak of the April–May 2003 outburst, as inferred from INTEGRAL data, and the spin-up rate of the pulsar during the outburst of 2000–2001, as inferred from the RXTE data. When fitting these data by the function given by Eq. (2), we fixed the mass and radius of the neutron star at $1.4 M_\odot$ and 10^6 cm, respectively. As a result, we obtained the following values: the distance to the source $d = 9.5 \pm 1.1$ kpc and the magnetic field of the neutron star $B = 2.5^{+0.4}_{-1.1} \times 10^{13}$ G, which corresponds to the position of the cyclotron feature in the object's spectrum at an energy of about 220 keV. The derived values agree with the distance to the binary estimated from optical observations (Negueruela *et al.* 2003) and with the magnetic field strength estimated by analyzing the source's spectra (see above). It should be noted that we used the expression $n(\omega_s) = 1 + \dfrac{20(1 - 1.94\omega_s)}{31(1 - \omega_s)}$ for the dimensionless angular momentum $n(\omega_s)$ from the paper by Li and Wang (1996). When the function suggested by Ghosh and Lamb (1979) is used as a fit to $n(\omega_s)$, the magnetic field strength proves to be slightly smaller, $B \sim 1.6 \times 10^{13}$ G, but the distance to the binary increases significantly, $d \sim 14$ kpc. If the latter parameter is fixed at 10 kpc, then the surface magnetic field of the neutron star decreases to $B \sim 5 \times 10^{12}$ G, but the quality of the fit to the data points in Fig. 9 deteriorates significantly.

As was noted in the Introduction, the mean spin-down rate of the pulsar KS 1947+300 is low enough for its pulsation period to be considered close to the equilibrium value. In the case of disk accretion, this period is then related to the parameters of

the neutron star as follows: $P_{\rm eq} \simeq 1.0 L_{37}^{-3/7} \mu_{30}^{6/7}$ s (Lipunov 1987). Assuming that the the source's luminosity is $\sim 10^{37}$ erg s^{-1} and the pulsation period is $\sim$18.7 s, we obtain a magnetic field strength of $\sim 3 \times 10^{13}$ G, in good agreement with the above estimates.

ACKNOWLEDGMENTS

We wish to thank E.M. Churazov, who developed the methods and software for analyzing the data from the IBIS telescope of the INTEGRAL observatory. We also wish to thank M.G. Revnivtsev for help in processing the RXTE data and valuable remarks and discussions. This work was supported by the Ministry of Industry and Sciences (grant no. NSh-2083.2003.2 from the President of Russia and project no. 40.022.1.1.1102) and the Russian Foundation for Basic Research (project nos. 02-02-17347 and 04-02-17276). We used the data retrieved from the High-Energy Astrophysics Archive at the Goddard Space Flight Center of NASA and the data retrieved from the Archive of the INTEGRAL Science Data Center (Versoix, Switzerland) and the Russian INTEGRAL Science Data Center (Moscow, Russia).

REFERENCES

1. M. M. Basko and R. A. Sunyaev, Mon. Not. R. Astron. Soc. **175**, 395 (1976).
2. A. Baykal, M. J. Stark, and J. H. Swank, Astrophys. J. **569**, 903 (2002).
3. K. N. Borozdin, M. R. Gilfanov, R. A. Sunyaev, *et al.*, Pis'ma Astron. Zh. **16**, 804 (1990) [Sov. Astron. Lett. **16**, 345 (1990)].
4. H. V. Bradt, R. E. Rothschild, and J. H. Swank, Astron. Astrophys., Suppl. Ser. **97**, 355 (1993).
5. D. Chakrabarty, T. Koh, L. Bildsten, *et al.*, Astrophys. J. **446**, 826 (1995).
6. D. K. Galloway, E. H. Morgan, and A. M. Levine, Astrophys. J. (2004, in press); astro-ph/0401476.
7. P. Ghosh and F. Lamb, Astrophys. J. **234**, 296 (1979).
8. V. M. Kaspi and F. P. Gavriil, Astrophys. J. Lett. **596**, L71 (2003).
9. A. Krawczyk, A. G. Lyne, J. A. Gil, *et al.*, Mon. Not. R. Astron. Soc. **340**, 1087 (2003).
10. F. Lebrun, J. P. Leray, P. Lavocat, *et al.*, Astron. Astrophys. **411**, L141 (2003).
11. X.-D. Li and Z.-R. Wang, Astron. Astrophys. **307**, L5 (1996).
12. V. M. Lipunov, *Astrophysics of Neutron Stars* (Nauka, Moscow, 1987) [in Russian].
13. N. Lund, S. Brandt, C. Budtz-Joergesen, *et al.*, Astron. Astrophys. **411**, L231 (2003).
14. A. A. Lutovinov, S. A. Grebenev, R. A. Sunyaev, and M. N. Pavlinskiĭ, Pis'ma Astron. Zh. **20**, 631 (1994) [Astron. Lett. **20**, 538 (1994)].
15. A. A. Lutovinov, S. V. Molkov, and M. G. Revnivstev, Pis'ma Astron. Zh. **29**, 803 (2003) [Astron. Lett. **29**, 713 (2003)].
16. F. Nagase, Publ. Astron. Soc. Jpn. **41**, 1 (1989).
17. I. Negueruela, G. L. Israel, A. Marco, *et al.*, Astron. Astrophys. **397**, 739 (2003).
18. A. N. Parmar, N. E. White, and L. Stella, Astrophys. J. **338**, 373 (1989).
19. M. G. Revnivstev, R. A. Sunyaev, D. A. Varshalovich, *et al.*, Pis'ma Astron. Zh. **30**, 430 (2004) [Astron. Lett. **30**, 382 (2004)].
20. J. Swank and E. Morgan, IAU Circ. No. 7531 (2000).
21. P. Ubertini, F. Lebrun, G. Di Cocco, *et al.*, Astron. Astrophys. **411**, L131 (2003).
22. N. White, J. Swank, and S. Holt, Astrophys. J. **270**, 771 (1983).
23. C. Winkler, T. J.-L. Courvoisier, G. Di Cocco, *et al.*, Astron. Astrophys. **411**, L1 (2003).

Translated by V. Astakhov

Astronomy Letters, Vol. 31, No. 2, 2005, pp. 98–102. Translated from Pis'ma v Astronomicheskiĭ Zhurnal, Vol. 31, No. 2, 2005, pp. 110–115.

Relationship between the Nonstationary Radio-Luminosity Variations of the Crab Nebula and the Activity of Its Pulsar

K. S. Stankevich* **and V. P. Ivanov****

Research Institute of Radiophysics, Nizhni Novgorod State University, ul. Lyadova 25/14, Nizhni Novgorod, 603600 Russia

Received August 19, 2004

Abstract—Based on the half-century-long history of radio observations of the Crab Nebula, we investigate the evolution of its radio luminosity. We found a secular decrease in the radio luminosity; it has decreased by 9% since the discovery of the radio source in 1948. Apart from the secular decrease in the luminosity of the Crab Nebula, we identified two time intervals, 1981–1987 and 1992–1998, when radio bursts with energy release $\sim 10^{41}$ erg took place. In these years, the spectral indices of the instantaneous spectra decreased significantly due to the increase in the flux densities at short (centimeter and millimeter) wavelengths. These events were preceded by sudden increases in the pulsar's rotation rates, the largest of which, with an amplitude of $\Delta\Omega/\Omega = 3 \times 10^{-8}$, occurred in 1975 and 1989. We show that the magnetospheric instability mechanism that accompanies strong glitches can provide the energetics of the excess luminosity of the Nebula through the ejection of relativistic electrons with a total energy higher than 6×10^{42} erg from the pulsar's magnetosphere. © *2005 Pleiades Publishing, Inc.*

Key words: *supernovae and supernova remnants, radio luminosity, evolution, pulsar, glitches, magnetospheric instability, injection.*

INTRODUCTION

The Crab Nebula was discovered as a radio source by Bolton and Stanley in 1948 and is the prototype of the growing class of plerions—supernova remnants with a pulsar. Since then the Nebula has been observed at radio wavelengths, and sufficient data have now been accumulated to analyze the relationship between the pulsar's activity and the luminosity of the Nebula.

The pulsar PSR B0531+21, which injects relativistic particles and magnetic fields into the Nebula, is the source of energy required to maintain the intense nebular emission. Energy is released through the loss of rotational energy by the neutron star, causing its rotation period to increase. For PSR B0531+21, the rate of increase in the period is $\dot{P} = 4.2 \times 10^{-13}$ s s^{-1}, and the rotation rate of the pulsar decreased by 0.7% in 23 years of timing observations (1969–1993) (Lyne *et al.* 1993). The smooth secular decrease is occasionally interrupted by a sudden increase in the rotation rate known as a glitch. Twelve such glitches have been recorded over the period of regular observations of the pulsar (since 1969). They are accompanied by energy release, thereby differing from other nonstationary phenomena found in the emission and timing of the pulsar (such as a dispersion jump, a slowdown of the rotational phase, shadow pulses). The secular and sudden changes in the rotation rate of the neutron star must affect the injection of relativistic particles and magnetic fields into the Nebula and can be responsible for the nonstationary behavior of its luminosity. Below, we discuss the effect of these processes on the radio luminosity of the Nebula.

INSTANTANEOUS SPECTRA

Instantaneous spectra measured at different epochs are required to investigate the evolution of the radio emission from the source. No systematic spectral measurements of the Crab Nebula were made in the past. Nine yearly spectra between 1955 and 1983 were reconstructed from the set of published data (Ivanov *et al.* 1994). We have observed the radio emission from the Crab Nebula since 1985 every year at frequencies from 0.5 to 15 GHz. Over one or two months every year, we measured the energy distribution of the radio emission at the Kara-Dag Radio Astronomy Station at twenty frequencies of this range to obtain an instantaneous spectrum of the Nebula at the corresponding epoch. We determined the absolute flux densities by comparison with the

*E-mail: stnk@nirfi.sci-nnov.ru
**E-mail: ivnv@nirfi.sci-nnov.ru

emission of a blackbody disk located in the far zone of the radio telescope. The method of absolute measurements (artificial Moon) and the instrumentation were finalized by 1969 (Stankevich *et al.* 1973), and the measuring procedure remained identical over the ensuing years. We obtained 17 instantaneous spectra of the radio emission from the Crab Nebula from 1985 until 2000. Based on 26 instantaneous spectra, we determined the spectral indices and luminosities of the Crab Nebula that formed an evolutionary sequence spanning 45 years. Figure 1 shows the distribution of spectral indices constructed from instantaneous spectra. Two intervals, 1981–1987 and 1992–1998, in which the spectral indices of the instantaneous spectra decreased significantly can be identified in this figure. The decrease in the slope of the instantaneous spectra is the result of an increase in the flux densities at short (centimeter) wavelengths in these years, which also affected the frequency distribution of the secular decrease in the flux densities.

The table lists the mean rates of secular changes in the flux densities for the period 1974–2000 at several wavelengths. Significant variations in the mean rate of decrease in the flux densities are observed at 550 and 960 MHz; their differences can be explained by nonstationary perturbations in the instantaneous spectra (Ivanov *et al.* 1994). A secular flux decrease is well-defined in the portions of the frequency spectrum where no perturbations were observed. Thus, for example, the flux densities at 15.3 and 6 cm form a decreasing sequence, and the relative yearly decreases in the flux densities at these wavelengths are identical within the error limits. A more complex picture is observed at shorter wavelengths. There is virtually no secular flux decrease at $\lambda = 3.7$ cm (8108 MHz). Aller and Reynolds (1985) measured the secular flux decrease at 8 GHz at the earlier epochs from 1969 until 1985, $\frac{1}{S}\frac{dS}{dt} = -(0.167 \pm 0.015)\%\ \mathrm{yr}^{-1}$.

According to our data, the flux densities at this frequency from 1974 until 1984 also form a decreasing sequence, $\frac{1}{S}\frac{dS}{dt} = -(0.150 \pm 0.033)\%\ \mathrm{yr}^{-1}$ (Ivanov *et al.* 1994). However, the set of data for the subsequent epochs (1985–2000) change the slope; as a result, the intensity of the emission remained virtually constant. The flux at $\lambda = 2$ cm showed a similar behavior. There are the absolute flux-density measurements at $\lambda = 8.1$ mm (37 GHz) made in 1974; we performed the next series of measurements 20 years later, in 1994, and repeated them in 1995 and 2000. The fluxes in recent years have increased by 10% since 1974. We have no reason to believe that the flux densities increased monotonically between 1974 and 1994; the flux increase may be the result of sporadic activity of the pulsar. Table gives the yearly flux increase obtained by linear fitting.

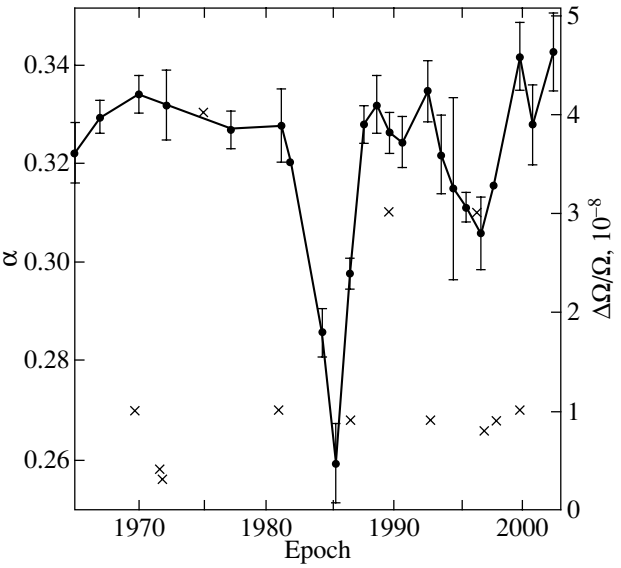

Fig. 1. Spectral-index distribution for the Crab Nebula, $\alpha = 0.3287$ is the mean unperturbed spectral index; the crosses mark glitches, the amplitude scale is on the right.

THE LUMINOSITY DISTRIBUTION FOR THE CRAB NEBULA FROM 1955 UNTIL 2000

Figure 2 shows the luminosity distribution for the Crab Nebula calculated using the instantaneous spectra in the frequency range 0.5–15 GHz. The straight line passes through the minimum luminosities within the error limits equal to the standard deviations and represents the secular change in the luminosity

$$L[\mathrm{erg\ s}^{-1}] = [3.9 - (t - 1960) \times 6.37 \times 10^{-3}] \times 10^{34}. \quad (1)$$

Yearly mean rates of secular changes in the flux densities in 1974–2000 at several wavelengths in the range 0.81–15.3 cm

Wavelength, cm	$\frac{1}{S}\frac{dS}{dt}$, % yr^{-1}
15.3	$-(0.159 \pm 0.024)$
6.14	$-(0.185 \pm 0.086)$
3.7	$-(0.06 \pm 0.03)$
2	$-(0.165 \pm 0.287)$
0.81	$+(0.45 \pm 0.057)$

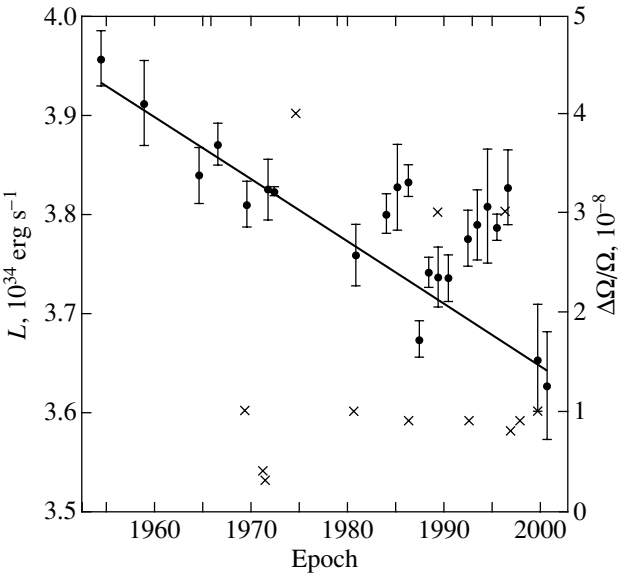

Fig. 2. Change in the luminosity of the Crab Nebula with time in the frequency range 0.5–15 GHz. The crosses mark glitches, the amplitude scale is on the right.

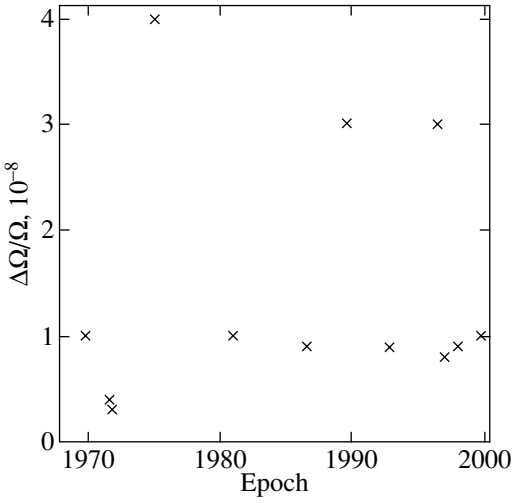

Fig. 3. Glitches in the pulsar PSR B0531+21; we used data from Boynton *et al.* (1972), Lohsen (1975), Lyne *et al.* (1993), Demianski and Proszynski (1983), Hobbs *et al.* (2002), and Wong *et al.* (2001).

The luminosity has decreased by 9% at a rate of

$$\frac{1}{L}\frac{dL}{dt} = -(0.167 \pm 0.012)\%\ \mathrm{yr}^{-1}$$

since the discovery of the radio source in the Crab Nebula in 1948 until now.

In the evolutionary model by Pacini and Salvati (1973), the energy injected by the pulsar into the nebula is

$$L_i(t) = L_{i0}(1 + t/\tau)^{-p}, \qquad (2)$$

where t is the age of the pulsar, τ is the spin-down time scale, and $p = n + 1/n - 1 = 2.325$, $n = 2.51 \pm 0.01$ is the braking index (Lyne *et al.* 1993). We derive the rate of decrease in the injected energy from Eq. (2):

$$\frac{1}{L_i}\frac{dL_i}{dt} = -\frac{p}{\tau + t}. \qquad (3)$$

For typical τ in the interval 300–700 yr, it is equal to $-(0.16 \pm 0.02)\%\ \mathrm{yr}^{-1}$ and corresponds to the rate of decrease in the luminosity of the Nebula. Thus, the luminosity of the Crab Nebula evolves as the energy injected by the pulsar decreases, and its value compensates for the energy losses inside the Nebula , in particular, through adiabatic expansion, only partially.

Two time intervals, 1981–1987 and 1992–1998, can be identified in Fig. 2 within which the luminosity rose and then rapidly decreased to the unperturbed level limited by the evolutionary component. The luminosity excess at maximum was 3.5 (1981–1987) and 5.2% (1992–1998). The luminosity bursts occurred when the slopes of the instantaneous spectra decreased and are the result of an increase in the flux densities at short (centimeter) wavelengths. The energy release was, on average, 10^{41} erg during each luminosity burst, which lasted five or six years. The additional injection of relativistic electrons into the Nebula by the pulsar must be the source of excess energy release. Let us consider the possible mechanism of such injection.

GLITCHES IN PSR B 0531+21

The slow spin-down of the Crab pulsar (due to magnetodipole radiation and current losses) between glitches is described by a power law:

$$\dot{\Omega} = -k\Omega^n, \qquad (4)$$

where the braking index $n = \Omega\ddot{\Omega}(\dot{\Omega})^{-2}$ was constant (within 0.5%) during all years of observations (Lyne *et al.* 1993). A sudden increase in the rotation rate (glitch) occurs exponentially with a time constant of ~0.8 days and then decays also exponentially with a time scale of 10–20 days. The glitch is characterized by the relative change in the rotation rate (or period) $\Delta\Omega/\Omega = -\Delta P/P$. Figure 3 shows all of the published (Lyne *et al.* 1993; Wong *et al.* 2001; Boynton *et al.* 1972; Lohsen 1975; Hobbs *et al.* 2002; Demianski and Proszynski 1983) glitches in the Crab pulsar; they all exceed $\Delta\Omega/\Omega = 10^{-9}$. Note that the amplitude of the fluctuations in the pulse arrival times called timing noise is $|\Delta\Omega/\Omega| \ll 10^{-10}$ (Wong *et al.* 2001). The greatest events occurred in 1975, 1989, and 1996, and they are of particular interest to us.

Glitches in the pulsar are also shown in the plots of the spectral-index (Fig. 1) and luminosity (Fig. 2) distributions for the Crab Nebula. Glitches with amplitudes 10^{-8} or lower occurred often, once in two or three years. They probably do not change appreciably the spectral-index and luminosity distributions. Glitches with higher amplitudes, 4×10^{-8} in 1975 and 3×10^{-8} in 1989, precede the periods of large changes in the spectrum and enhanced luminosity, which begin with a delay of four or five years. The changes in the spectral distributions last five or six years; spatial scales on the order of the region with a radius of 1 pc around the pulsar correspond to this period. Thus, luminosity perturbations are observed as the relativistic electrons injected by the pulsar fill the inner shell of the Crab Nebula.

A sudden increase in the rotation rate of a neutron star is known to result from a decrease in the moment of inertia: the oblateness ε of the star changes due to the deformation of its outer crust. If the moment of inertia of the star's equilibrium configuration is $I = I_0(1 + \varepsilon)$, the amplitude of the change in the rotation rate as the oblateness decreases by $\Delta\varepsilon$ is

$$\Delta\varepsilon = \Delta I/I = -\Delta\Omega/\Omega. \quad (5)$$

Gravitational energy is released as the oblateness of the star decreases; its total store in the crust of the Crab neutron star is estimated to be 2×10^{42} erg (Pines 1974). The excess luminosity of the Nebula after a strong glitch is, on average, 5% of this value. Since glitches with amplitudes of 3×10^{-8} occur relatively often (three glitches in 23 years of timing observations), the store of gravitational energy in the crust does not provide the energetics of the excess luminosity of the Nebula. Therefore, there must be another, nongravitational mechanism of the injection of additional energy that switches on during glitches in the pulsar.

THE MECHANISM OF MAGNETOSPHERIC INSTABILITY

Previously, the magnetospheric instability mechanism—sudden release of the particles of the plasma confined by closed magnetic field lines of the pulsar (Scargle and Pacini 1971; Roberts and Sturrock 1972)—was considered among other mechanisms to explain the observed glitches. Subsequently, the dynamical parameters of the glitches in the Crab pulsar were found to be faithfully described by the model of a starquake in the crust of the neutron star, and the magnetospheric instability mechanism found no application. However, it is appropriate to consider this mechanism in connection with the problem of energy release during a glitch in the pulsar. It should be borne in mind that the glitch in August 1989 was traced in detail and is now considered as typical of a starquake (Lyne *et al.* 1993), while the glitches in 1975 and 1989 were very similar in shape and amplitude. Therefore, the starquake and magnetospheric instability mechanisms must operate simultaneously at large glitch amplitudes. During a sudden increase in the rotation rate of the neutron star, the radius of the light cylinder decreases abruptly, which can act as a trigger mechanism stimulating the sudden ejection of the pulsar's relativistic magnetospheric plasma into the shell of the Crab Nebula. There is a maximum moment of inertia I_p of the plasma that can confine the magnetic field of the pulsar (Ruderman 1972):

$$I_p \cong \frac{B_0^2 R^3}{6\Omega^2}, \quad (6)$$

where R is the radius of the neutron star, and

$$B_0 = 3.2 \times 10^{19}(P\dot{P})^{1/2}\ \text{G} \quad (7)$$

is the magnetic field of the pulsar. In the Crab Nebula, $B_0 = 3.76 \times 10^{12}$ G, and we obtain $I_p = 6.5 \times 10^{37}$ g cm^2 at $R = 10^6$ cm. Let us estimate the mass M_p of the magnetospheric plasma around the pulsar using the moment of inertia:

$$I_p \cong M_p r_m^2, \quad (8)$$

where $r_m = c\Omega^{-1}$ is the radius of the light cylinder. We obtain $M_p = 2.6 \times 10^{21}$ g from Eqs. (6)–(8). Since the plasma is quasi-neutral, the number of pairs of relativistic protons and electrons ejected from the magnetosphere into the Nebula is $N_p = N_e = 1.6 \times 10^{45}$.

As was noted above, the decrease in the spectral index and the increase in the luminosity of the Nebula result from the increase in the intensity at short centimeter wavelengths, less than $\lambda = 3.5$ cm. At this wavelength, relativistic electrons with energy $E = 2.4 \times 10^9$ eV emit radiation in the magnetic field of the Nebula, $H = 3 \times 10^{-4}$ G. If the excess luminosity of the Nebula is produced by the relativistic electrons ejected from the pulsar's magnetosphere during a glitch (N_e), then the minimum energy of these electrons must also be $E_{\min} = 2.4 \times 10^9$ eV, and the total energy distribution must be a power law with an index $1 < \gamma \leq 1.2$. Thus, the total energy of the relativistic electrons injected into the Nebula during each strong glitch exceeds $N_e E = 6 \times 10^{42}$ erg. The mechanism of sudden release of the pulsar's magnetospheric plasma particles can provide the energetics of the excess luminosity of the Nebula and explain how relativistic particles are injected into the shell of the Crab Nebula. In this interpretation, the time between two glitches in the pulsar with amplitudes of

$\Delta\Omega/\Omega = (3–4) \times 10^{-8}$ is found to be enough to accumulate excess plasma mass in the magnetosphere to create conditions for magnetospheric instability and ejection of relativistic particles into the shell of the Nebula.

CONCLUSIONS

(1) Based on 26 instantaneous radio spectra of the Crab Nebula for the period from 1955 until 2000, we obtained data on the spectral indices and luminosities that formed an evolutionary sequence. The luminosity decreased secularly at a mean rate of $(0.167 \pm 0.012)\%$ yr^{-1}; the luminosity of the radio source has decreased by 9% since its discovery in 1948. The luminosity of the Crab Nebula evolves as the energy injected by the pulsar decreases; the rate of its decrease is also 0.16% yr^{-1} and compensates for the energy losses inside the Nebula (particularly through adiabatic expansion) only partially.

(2) Apart from the secular decrease in the luminosity of the Crab Nebula, we identified two time intervals, 1981–1987 and 1992–1998, when the radio brightness increased and reached its maximum in the middle of the interval and then decreased to the unperturbed level. The energy release during each burst was, on average, 10^{41} erg. In these years, the spectral indices of the instantaneous spectra decreased significantly due to the increase in the flux densities at short centimeter and millimeter wavelengths.

(3) Glitches in the pulsar with large amplitudes, 4×10^{-8} in 1975 and 3×10^{-8} in 1989, precede the periods of large changes in the spectrum and enhanced luminosity. The magnetospheric instability mechanism, in which the particles of the relativistic plasma confined by the pulsar's closed magnetic field lines are suddenly released, is enough to provide the energetics of the excess luminosity of the Nebula: the total energy of the relativistic electrons injected into the Nebula during a glitch exceeds 6×10^{42} erg. Starquakes in the neutron-star crust are known to be responsible for the glitches in the pulsar. Magnetospheric instability arises at large glitch amplitudes, $\sim 3 \times 10^{-8}$, and accompanies a starquake. Spectral perturbations are observed as the relativistic electrons injected by the pulsar fill the inner shell of the Crab Nebula.

(4) We analyzed the frequency distribution of the secular decrease in the flux density and showed that the amplitude the secular decrease is affected by nonstantionary perturbations in the instantaneous spectra. The flux densities at 1960 and 4880 MHz form a decreasing sequence, and the yearly decrease in the flux density is 0.16%, which is typical of the unperturbed spectrum. The increases in the flux densities at short centimeter and millimeter wavelengths in 1981–1987 and 1992–1998 changed the distribution of the secular decrease in the flux densities in this part of the spectrum.

ACKNOWLEDGMENTS

This work was supported by the Program for Support of Leading Scientific Schools (project no. NSh-1483.2003.2) and the Astronomy Program.

REFERENCES

1. H. D. Aller and S. P. Reynolds, Astrophys. J. Lett. **293**, L73 (1985).
2. F. E. Boynton, E. J. Groth, D. F. Hutchinson, *et al.*, Astrophys. J. **175**, 217 (1972).
3. M. Demianski and M. Proszynski, Mon. Not. R. Astron. Soc. **202**, 437 (1983).
4. G. Hobbs, A. G. Lyne, B. C. Joshi, *et al.*, Mon. Not. R. Astron. Soc. **333**, L7 (2002).
5. V. P. Ivanov, K. S. Stankevich, and S. P. Stolyrov, Astron. Zh. **71**, 737 (1994) [Astron. Rep. **38**, 654 (1994)].
6. E. Lohsen, Nature **258**, 688 (1975).
7. A. G. Lyne, R. S. Pritchard, and F. G. Smith, Mon. Not. R. Astron. Soc. **265**, 1003 (1993).
8. F. Pacini and M. Salvati, Astrophys. J. **186**, 249 (1973).
9. D. Pines, *Proc. 16th Solvay Conf. on Physics, Brussels, 1974*, p. 147.
10. D. H. Roberts and P. A. Sturrock, Astrophys. J. **173**, L33 (1972).
11. M. A. Ruderman, Annu. Rev. Astron. Astrophys. **10**, 427 (1972).
12. J. D. Scargle and F. Pacini, Nature Phys. Sci. Lett. **232**, 144 (1971).
13. K. S. Stankevich, V. P. Ivanov, S. A. Pelyushenko, *et al.*, Izv. Vyssh. Uchebn. Zaved., Radiofiz. **16**, 786 (1973).
14. T. Wong, D. C. Backer, and A. G. Lyne, Astrophys. J. **548**, 447 (2001).

Translated by A. Dambis